b139 729 23

U.O.V.S. BIBLIOTEEK

D' at T

University Free State
34300000737001
Universiteit Vrystaat

A Monte Carlo simulation of the effect of a ZnO layer on the cathodoluminescence generated in a ZnS phosphor powder

Abraham Petrus Greeff (M.Sc.)

A dissertation presented in fulfillment of the requirements for the degree

PHILOSOPHIAE DOCTOR

in the
Faculty of Natural and Agricultural Sciences
Department of Physics
at the
University of the Free State
Bloemfontein

Promoter: Prof H.C. Swart
August 2001

Universiteit van die
Oranje-Vrystaat
BLOEMFONTEIN
28 JAN 2002
UOVS SASOL BIBLIOTEEK

Bedankings

Hiermee wil ek graag my opregte dank en waardering betuig teenoor:

- Professor H.C. Swart vir sy vriendskap en bekwame leiding tydens hierdie studie.
- Professor G.L.P. Berning vir sy kommentaar en voorstelle tydens die afronding van die skripsie.
- My kollegas aan die UV Fisikadepartement vir hul vriendelikheid, behulpsaamheid en belangstelling tydens hierdie studie.
- My ouers vir al hul liefde, ondersteuning en belangstelling tydens my studiejare.
- Janine, die wonderlike "ander helfte" van 'n uitstekende span.

Maar bo alles, dankie aan my Hemelse Vader wat my die kennis, insig en krag gegee het om hierdie studie na die beste van my vermoeëns te kon voltooi.

A.P. Greeff
9 April 2001

Opsomming

Katodestraalbuise (*Cathode ray tubes, CRTs*) is tans 'n gewilde keuse wat vertooneenhede betref omrede die goeie beeldkwaliteit, asook die maklike en ekonomiese vervaardigingsproses. Ongelukkig is hierdie vertooneenhede groot en swaar en het dit 'n hoë energieverbruik wat dit ongeskik maak vir draagbare of handhoubare elektroniese toestelle. Indien die huidige uitbouing van die mark vir hierdie tipe toestelle in ag geneem word met die beloftes van toekomstige groei, sal 'n dun en ligte vertooneenheid 'n baie gesogte kommoditeit wees in die vertooneenheidmark.

Daar is verskillende tipes van hierdie plat vertooneenhede tans beskikbaar, met die Aktiewe matriks vloeikristal (*Active matrix liquid crystal display, AMLCD*) eenhede die gewildste keuse vir draagbare of handhoubare toestelle. Een moontlike alternatief vir vloeikristal -vertooneenhede is die Veldemmissievertooneenheid (*Field emission display, FED*). Dit werk op dieselfde basiese beginsels as CRTs, maar in plaas van drie elektrongewere, het die FED 'n matriks van klein metaalpunte wat optree as elektronbronne. Hierdie matriks is geleë digby die agterkant van die fosforskerm. Hierdie uiters kompakte opstelling wek lig op deur 'n proses van katodeluminessensie (*Cathodoluminescence, CL*).

Om die energieverbruik van FEDs te verminder, kan die versnelspanning van elektrone tussen die elektronbronne en die fosforskerm verminder word. Die laer versnelspanning skep egter probleme wat beeldkwaliteit en die leeftyd van die skerm betref. Huidiglik word konvensionele ZnS-tipe fosforpoeiers, dieselfde wat gebruik word in CRTs, gebruik om lig in FEDs op te wek. Tydens lang blootstelling aan elektronbombardering oksideer die fosforpoeier tot 'n nie-lumineserende ZnO lagie waar die oppervlak blootgestel word aan die elektronbundel. Die vorming van hierdie oksiedlagie is die gevolg van oppervlak chemiese reaksies tussen die ZnS fosforpoeier en waterdamp wat teenwoordig is in die ultra hoë vakuum omgewing. Die reaksie self word gestimuleer deur die elektronbundel. Die lae-energie elektrone in FEDs het 'n vlakker indringingsdiepte as dié wat gebruik word in CRTs. Aangesien die CL afhanklik is van die energieverlies van die elektrone in die fosforpoeier, neem die CL intensiteit af as gevolg van die groei van die ZnO lagie en die energieverlies binne-in die lagie. Dit lei dus tot 'n afname in beeldkwaliteit en die leeftyd van die fosforskerm.

In hierdie studie is die invloed van die ZnO lagie op die CL intensiteit bestudeer deur gebruik te maak van Monte Carlo simulasiemetodes. Die CL intensiteit kan gekwantifiseer word deur die proses van ligopwekking in drie afsonderlike stappe te beskou: die indringing van elektrone

in die fosforpoeier, die energieverlies van die elektrone en dan die opwekking en absorpsie van fotone deur die fosformateriaal.

Die fosforpoeier bestaan uit 'n distribusie van sferiese en plat korrels. As gevolg van die vorm van die sferiese korrels, asook die willekeurige oriëntasie van die plat korrels, varieër die dikte van die gevormde ZnO lagie met die invalshoek van die elektrone. In die eerste stap is 'n Monte Carlo metode gebruik om 'n invalshoekdistribusie te simuleer om sodoende die struktuur van die fosforpoeier in ag te neem. Die invalshoeke is gesimuleer deur die elektronpaaie te versprei oor 'n oppervlak wat gemodelleer is volgens die fosforpoeier se struktuur. Tweedens is die bane van die lae energie elektrone gesimuleer soos die elektrone die ZnO lagie indring en deurbeweeg na die ZnS fosformateriaal. Die simulasie is uitgevoer deur 'n gewone enkelverstrooiings Monte Carlo metode te gebruik, maar is verbeter deur 'n diffusie-intervlak te gebruik om die elektrone se energieverlies in die gebied tussen die ZnO en ZnS akkuraat te simuleer. Vanuit hierdie simulasies is energieverliesprofiele verkry vir spesifieke ZnO diktes, elektronbundelenergieë en diffusie-intervlakdiktes. Derdens is die elektronenergieverlies in ZnS bereken deur die energieverliesprofiele te gebruik en te aanvaar dat die diffusie-intervlak nie-lumineserend is nie. Die energieverlies in ZnS lei tot die vorming van elektron-holte pare wat weer kombineer en moontlik kan lei tot fotonopwekking. 'n Uitdrukking is afgelei om die CL intensiteit te kwantifiseer. Die uitdrukking kompenseer vir die absorpsie van fotone deur die fosformateriaal en elimineer kwantummeganiese en optiese aspekte soos totale interne weerkaatsing deur middel van normalisering. Deur hierdie uitdrukking toe te pas op die elektronenergieverlies in ZnS kan 'n kromme verkry word wat die CL intensiteit as funksie van ZnO dikte weergee vir 'n spesifieke bundelenergie.

In hierdie studie is die kwantifiseringsuitdrukking toegepas op die eksperimentele resultate van twee tipes fosforpoeiers. Die ZnS:Cu,Al,Au poeier word gebruik om groen lig op te wek, terwyl die ZnS:Ag,Cl poeier gebruik word om blou lig op te wek. Vir ZnS:Cu,Al,Au vergelyk die gesimuleerde ZnO dikte baie goed met eksperimentele gemete waardes vir die oksieddikte. Indien dieselfde simulasieparameters gebruik word vir ZnS:Ag,Cl is die eksperimentele gemete oksieddikte baie dunner as die voorspelde waarde. Hierdie verskil kan toegeskryf word aan die versameling van lading oor die gebied van die primêre elektrone tydens elektronbombardering. Dit verlaag die tempo van oksiedgroei asook die waarskynlikheid van elektron-holte pare herkombinasie.

Summary

Today Cathode ray tubes (CRTs) are the standard in display technology due to their good image quality, ease of manufacturing and economy. Unfortunately, these displays are bulky and have a high power consumption making it unsuitable for portable or hand held electronic devices. With the current market expansion of these devices and the prospects claimed by future projections, a thin lightweight display with low power consumption and excellent image quality will be a very sought after commodity in the display market.

There are various types of flat panel displays on offer, with the Active matrix liquid crystal display (AMLCD) the most popular choice for portable or hand held devices. One possible alternative to liquid crystal displays are Field emission displays (FEDs). It works on a similar principle as an ordinary CRT, but instead of three electrons guns it has an array of tiny metallic tips acting as electron emitters. They are situated in close proximity at the back of the phosphor screen. This extremely compact setup produces light by a process of cathodoluminescence (CL).

To lower the power consumption of FEDs, the accelerating voltage of electrons between the emitters and phosphor screen can be reduced. The lower acceleration voltage results in some difficulties concerning image quality and the lifetime of the phosphor screen. Currently conventional ZnS-based phosphor powders, the same used in CRTs, are used to generate light in FEDs. During prolonged exposure to the electron beam the phosphor powder oxidizes to a non-luminescent ZnO layer where the surface is irradiated by the electron beam. The formation of this oxide layer is due to surface chemical reactions between the ZnS phosphor and water vapor which is present in the ultra high vacuum environment. The reaction itself is stimulated by the electron beam. The low energy electrons in FEDs have a shallower penetration depth than those used in CRTs. Since the CL is dependent upon the energy loss in the phosphor powder, the CL decreases due to the growth of the ZnO layer and the energy loss inside the layer. This leads to a decrease in the image quality and lifetime of the screen.

In this study the influence of the ZnO layer on the CL intensity was investigated using Monte Carlo simulation methods. The CL intensity can be quantified by separating the light generation process into three steps: the penetration of the electrons into the powder, the energy loss of the electrons and the generation and absorption of photons by the phosphor material.

The phosphor powder consists of a distribution of spherical and flat grains. Due to the shape of the spherical grains as well as the random orientation of the flat grains, the thickness of

the oxide layer varies with the incident angle of the electron beam. In the first step a Monte Carlo method was used to simulate a distribution for the incident angles to take into account the structure of the phosphor powder. The incident angles were simulated by spreading the electron paths over a surface modeled according to the structure of the phosphor powder. Secondly, the trajectories of the low energy electrons were simulated as it penetrated the ZnO layer and moved into the ZnS phosphor material. The simulation was performed using an ordinary single scattering Monte Carlo method, but was improved by using a diffusion interface to accurately simulate the energy loss of electron in the interface region between ZnO and ZnS. From these simulations energy loss profiles were obtained for specific ZnO thicknesses, electron beam energies and diffusion interface thicknesses. Thirdly, the electron energy loss in the ZnS was calculated by using the energy loss profiles and assuming that the diffusion interface was non-luminescent. The energy loss in ZnS leads to creation of electron-hole pairs that may recombine radiatively and generate photons. An expression was derived to quantify the generated CL. The expression compensates for the absorption of photons by the phosphor material and eliminates quantum mechanical and other optical aspects like total internal reflection by normalization. Applying the quantification expression to the electron energy loss in ZnS a curve relating the CL intensity to the ZnO thickness for a specific beam energy was determined.

In this study the quantification expression was applied to the experimental results of two types of phosphor powders. The ZnS:Cu,Al,Au powder is used to generate green light, while the ZnS:Ag,Cl powder is used for blue light. For ZnS:Cu,Al,Au the predicted ZnO thickness compare extremely well with experimental measurements. However, using the same simulation parameters, the experimentally measured oxide thickness on ZnS:Ag,Cl is much thinner than the predicted value. This difference can be attributed to the trapping of charge over the range of the primary electrons during electron irradiation. This lowers the rate of oxide formation as well as the probability of electron-hole pair recombination.

Keywords: Field emission displays, ZnS phosphor powder, Electron beam irradiation, Cathodoluminescence degradation, Monte Carlo simulation, CL quantification

Contents

Chapter 1

A background to current display technologies

1.1 Introduction

Cathode ray tubes (CRTs) continue to serve as the standard for image quality, manufacturability and economy in the display market. Unfortunately, conventional CRTs are bulky and have a high power consumption. This is acceptable for TV sets and desktop computer monitors but totally unsuitable for compact and portable display devices.

For these types of applications flat panel displays (FPDs) are superior. According to a document published in 1998 by the US Defense Department[1] the FPD market was worth about US$14 billion in 1997 and is projected to reach about US$20 billion by the year 2000. Notebook computers constitute 60% of this market while other hand-held devices, like personal digital assistants and digital cameras, make up the rest. Furthermore, it is expected that these markets will double in size around 2001 or 2002. With this projected growth, companies are currently undertaking very large research and development programs to position their products in the FPD market. A number of different technologies are used in making FPDs, each having it's own characteristics, with differing strengths and weaknesses. The most important display types are Liquid Crystal Displays (LCDs), Electroluminescent displays (ELDs) and Field Emission Displays (FEDs).

1.2 The different display technologies

1.2.1 Liquid Crystal Displays (LCDs)

LCDs contain a transparent organic polymer that respond to an applied voltage by changing it's orientation. This alters the polarization of light passing through the crystals and makes the display either transparent or dark for light passing through it. The displays are manufactured by depositing a polarizing film onto the outer surfaces of two quartz substrates with a matrix of transparent indium tin oxide (ITO) electrodes on the inner surfaces of the substrates. With micron-sized spacers holding the two substrates apart, it is joined together and the outer edges are sealed with a gasket. The interior is then evacuated and injected with a polymer.

The polarizers on the front and back of the display are orientated 90^o with respect to one another. With this orientation no light can pass through the display unless the polarization of the light is altered. When no voltage is applied, liquid crystals can be aligned in twisted (90^o) or super twisted (270^o) configurations. With these configurations the polarity of light is rotated allowing the light to pass through the front polarizer, illuminating the viewing surface. When a voltage is applied, the liquid crystals align to the created electric field, the polarity of the incoming light does not change and the viewing surface appears dark.

All LCDs must have a source of reflected or back lightning. This source is usually a metal halide, cold cathode, fluorescent or halogen bulb placed behind the back plate. Since the light must pass through the polarizers, glass, liquid crystals, filters and electrodes only about 5% of the original light exists on the viewers side. Therefore the generation of unseen light is a major drain on the battery-operated LCDs power source.

The most common LCD is the passive matrix type and has been used in watches and calculators since the early 1970's. Another type of LCD is the active matrix display which uses diodes or thin film transistors (TFTs) at each pixel to control the pixel's on-off state. In Figure 1.2.1 a diagram is shown of the construction of an active matrix LCD. TFTs are fabricated in a manner similar to integrated circuits and much of the manufacturing equipment, materials and accumulated knowledge about silicon is applicable to the fabrication process. The front transparent electrode is deposited over the entire glass surface and serves as a ground connection. The rear glass is deposited with a matrix of transistors and metal interconnect lines. For monochrome displays there is at least one transistor for each pixel and for full colour displays there are at least three per pixel. Even with redundant transistors at each pixel, some pixels fail to operate, resulting in a loss in image quality. Furthermore, the response time of the liquid

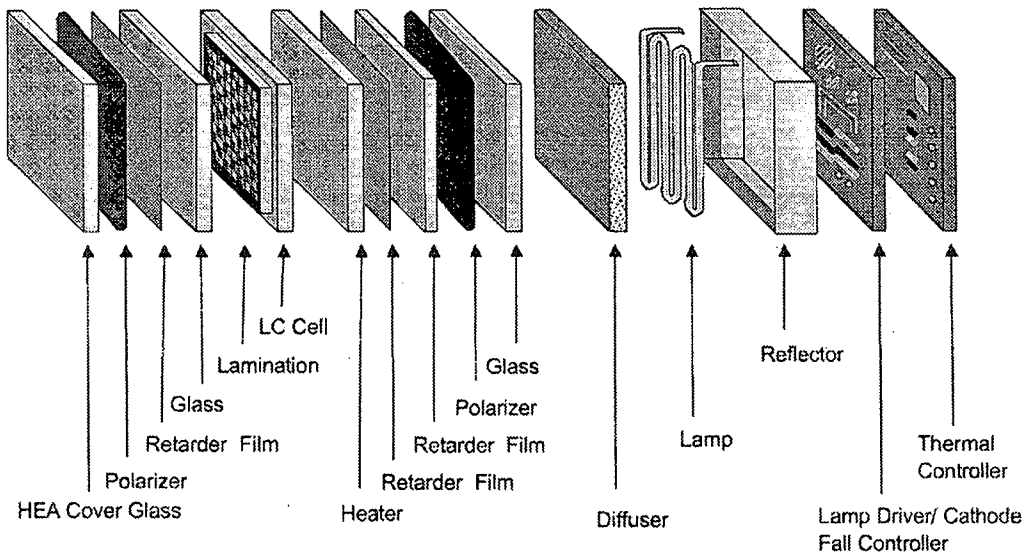

Figure 1.1: A diagram showing the construction of an active matrix LCD display. Illustration courtesy of [1].

crystals are relatively slow. This results in a display that is relatively slow and unsuitable for displaying images at video speeds. The slowness increases as the display becomes larger and combined with the intensive fabrication process has inhibited LCDs becoming larger. Despite these drawbacks, LCDs are still the current leader in the FPD market [1].

1.2.2 Electroluminescent Displays (ELDs)

ELDs are classified as emissive displays because they generate their own light, unlike LCDs. The light generating material is a phosphor which is sandwiched between two glass or quartz substrates acting as front and back electrodes. The passive and active matrix addressing schemes are similar to those described for liquid crystal displays. In Figure 1.2.2 a diagram is shown of the construction of an ELD.

The process of electroluminescence can be described as the non-thermal conversion of electrical energy into light. In the ELD light is emitted from the phosphor when a high electric field is applied between the front and back electrodes and electrons accelerated in the phosphor impact with an activator center to produce light [3].

Currently there is very little ELD usage in computer and consumer electronic products due

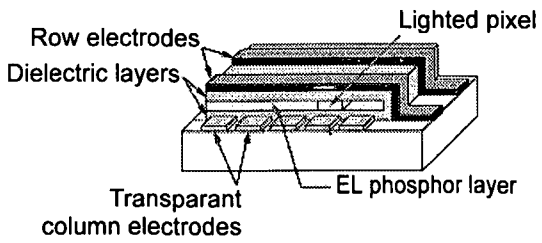

Figure 1.2: A diagram showing the construction of a ELD. Illustration courtesy of [2].

to inefficient colour capabilities of the phosphor and also, to a lesser extent, the high cost of electronic driving circuits. The phosphor powders used in these displays are the same as those used in ordinary CRTs which require a high accelerating voltage for activation. Active matrix addressed ELDs also require high-voltage transistors at each pixel to activate the phosphors. Improvements have been made concerning the luminous efficiency, particularly for the blue colours and is therefore likely to gain popularity as improvements in phosphor technology are made.

1.2.3 Field Emission Displays (FEDs)

FEDs are solid state vacuum displays that operate on a similar principle to CRTs. Both display types generate light by a process called cathodoluminescence. Electrons from the electron gun or cathode are accelerated across a vacuum gap to irradiate the phosphor powders in the screen which act as the anode and produce light. The most important difference between these two displays is the source of electrons. In the CRT three electron guns are used to scan a beam of electrons across the screen, while the FED employs an array of miniature cathodes to accelerate the electrons. Using this setup the distance between the cathodes and the phosphor screen shrinks by many orders of magnitude. This is illustrated in Figure 1.2.3 where a FED is compared with a CRT of similar screen dimensions.

The FED itself consists of two flat sheets of glass separated by a gap of about 1 mm. The faceplate is coated with phosphor and an array of microscopic cathodes is formed on a base-plate using thin film processing technology similar to that used in LCD panel fabrication. In Figure 1.2.3 a diagram is shown of the basic FED construction and in Figure 1.2.3 a scanning electron microscope (SEM) image is shown of the cathode array and gate surface. Each cathode array is separately addressed to generate an electron source by a process called cold cathode emission. The electron emission is obtained by applying a voltage between the cath-

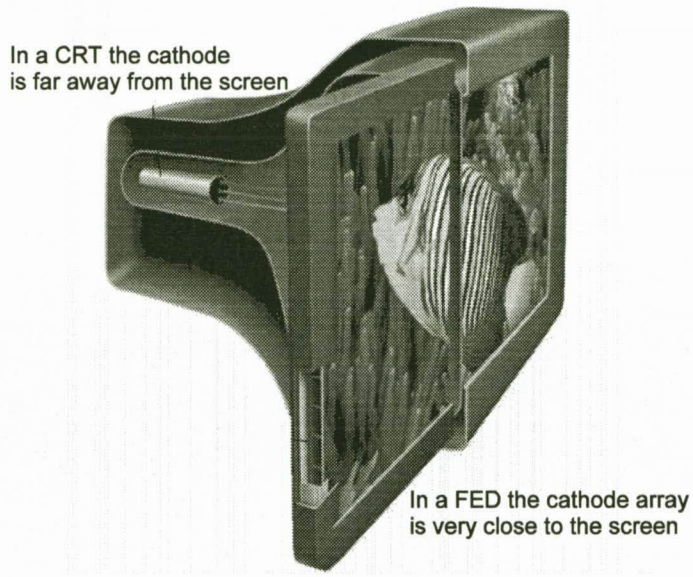

Figure 1.3: A comparison between a FED and a CRT of similar screen dimensions. The drastic reduction in size for the FED is due to the use of an array of miniature cathodes instead of the usual three electron guns. Illustration courtesy of [4].

odes and the gate situated above the cathodes. This results in a very power efficient display because there is no cathode heating involved as the case is with CRTs. These generated electrons are then accelerated towards the screen. Further power efficiency is gained because a FED does not require the shadow mask used in conventional CRTs which can waste up to 80% of the power. The pixel shown in Figure 1.2.3 consists of three different colour light emitting phosphor powders. By varying the electron emission to each addressable cathode, light of varying intensity and colour can be generated.

There are two basic types of phosphors used in FEDs to generate light. These are aluminum coated high voltage phosphors, referred to as the P22 group and the uncoated low voltage phosphors. The high voltage type is used in CRTs for it's superior colour quality and efficiency at high accelerating voltages. However, using the same phosphor in FEDs introduces a number of challenges. One problem is the fact that a high voltage is required to accelerate the electrons, requiring a larger vacuum gap between the faceplate and the cathode. The internal structural supports must bridge this vacuum gap and not impact the electron beam, which would cause visible variations in phosphor luminance. The increased gap also requires an active focusing structure. Low-voltage phosphors simplify the support problem because the supports can be

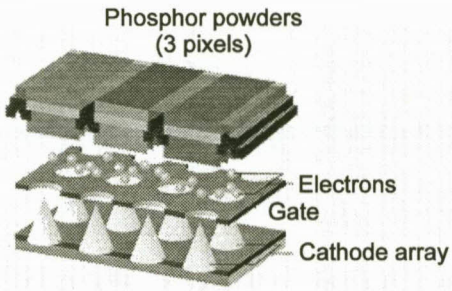

Figure 1.4: A diagram showing the basic operation of a FED. Electrons generated at the miniature cathodes are accelerated towards the phosphor screen where light is generated upon impact. Illustration courtesy of [4].

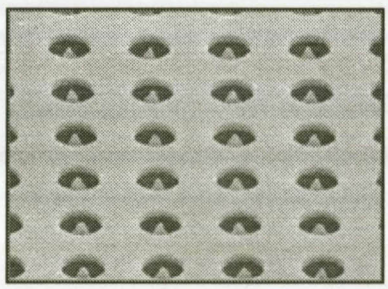

Figure 1.5: A SEM image of the miniature cathode array. The electron emitters can be seen through the holes in the gate's surface. Each gate measures about 1 mm in diameter. Image courtesy of [5].

	CRT	*LCD*	*ELD*	*FED*
Low cost	•			•
Ease of manufacturing	•			•
Wide viewing angle	•		•	•
Rugged			•	•
Sharpness	•			•
Low power		•		•
High resolution	•	•		•
Thin		•	•	•
Lightweight		•	•	•

Table 1.1: A comparison between the different display technologies currently available.

roughly as high as they are wide e.g., 0.1 mm $\times$ 0.1 mm, but deliver inadequate colour visual performance, life, and power efficiency. Low-voltage colour phosphors typically require over 10 times more beam current than high-voltage phosphors to generate the same level of luminance. Since the phosphor life is proportional to the beam current, low-voltage phosphors consequently age faster, resulting in an unacceptable short product life. Low-voltage phosphors also have less than 25% of the power efficiency of high-voltage phosphors due to heating, the lack of a aluminum reflective film and an increased need for a clean phosphor surface.

1.3 The advantages and disadvantages of FEDs

Considering the share of portable electronic devices like notebook computers in the FPD market and the market's projected growth in the next couple of years, FEDs are the perfect successor to the current LCD generation offering many advantages. In Table 1.3 FEDs are compared to other display technologies on the grounds of economic, fabrication and image quality differences. Compared to it's current rival in the display technology market, active matrix LCDs, FEDs offer many more advantages.

FEDs are simpler and less expensive to fabricate than active matrix LCDs. The construction is less complex and there is a higher tolerance for defects, fewer layers of assembly and fewer alignment problems. The cathode array permits a number of cathodes to be redundant without any loss in image quality. Compared to LCDs a few defective TFTs can ruin the screen. According to estimates [4] a full scale FED manufacturing facility will be about 33% cheaper than a LCD manufacturing plant of similar capacity, lowering the production costs. Account-

	FED product
Candescent (www.candescent.com)	13.2" 800×600 SVGA*
PixTech (www.pixtech.com)	12.1" 800×600 Mono
Futaba (www.futaba-eu.com)	5.8" 640×480 Mono

Table 1.2: A table listing the various companies involved in FED development and the products currently offered. Prototypes that are not for commercial use are indicated by *.

ing for a third of the total cost of a notebook computer, the screen is the most expensive component. Savings in this area will therefore likely result in a price decrease of these devices, making it more affordable for consumers.

Due to the simple construction of the FED with the light emitting phosphors in the faceplate, wide viewing angles are possible. According to a PixTech product data sheet [6] the total viewing angle is as large as 160^o without any loss in brightness. Furthermore, the FED is well suited for harsh environments being able to operate in the temperature range -20 to 70^oC. Other types of FPDs have a much narrower operating temperature range, making them impractical for very cold or very hot environments.

The full colour FEDs are able to deliver 24 bit colour quality at a screen resolution that ranges from 320×240 pixels currently on offer by PixTech to 800× 600 pixels prototype currently under development by Candescent. In some LCDs an increase in the screen's resolution or colour pallette decreases the back light transmission. Increasing the back light's intensity, raises power consumption and shortens battery life. Another advantage of FEDs is that their response time is about 5 times faster than the fastest active matrix LCD. This enables the FED to display images at video speeds making it very suitable for multimedia applications.

While it is a very promising technology, all FED efforts are still in the research and development stage with companies only now starting to show full colour prototypes with mono colour displays already available for purchase. In Table 1.3 a list is given of the current market leaders and the products currently on offer.

The main issue preventing FEDs to enter full scale production is the trade-off between the lifetime of the phosphor powder and power consumption. If high voltage phosphors (P22-group) are used, the quality of the display is comparable to that of CRTs with a long phosphor lifetime. But the display's power consumption increases, making it unsuitable for portable devices relying on battery power. If low voltage phosphors are used, not only does the power consumption decrease but also the phosphor lifetimes, again making it unsuitable for displays

[7].

In terms of performance, power, efficiency and lifetime characteristics high voltage phosphor are the obvious choice for FEDs and will probably be the only commercially viable phosphor choice for many years to come. In the next chapter the technical difficulties surrounding the use of these phosphors in FEDs are discussed.

Chapter 2

Using conventional phosphors in FEDs

2.1 Introduction

In the previous chapter the superiority of FEDs compared to the current dominant LCD technology was highlighted. The question was also raised about which type of phosphor to use in the displays and it was concluded that the conventional high voltage phosphor is currently the only viable option due to it's longer lifetime and higher luminosity.

These high voltage phosphors, which are also used in CRTs, are of the standard ZnS type. The phosphor powder is generally produced in a series of calcining, grinding and annealing steps. Activators and dopants, responsible for light emission during electron irradiation, are introduced and dispersed in the phosphor during high temperature reactions. The ZnS-based phosphors that produce light in the blue region (450 nm) of the visible light spectrum are doped with trace amounts of Ag and Cl (P22B group), while those that produce light in the green region (501 nm) are doped with Cu, Al and Au (P22G group). The phosphor powders used in this study were standard ZnS:Ag,Cl and ZnS:Cu,Al,Au powders obtained from Osram Sylvania.

The phosphor screen is a very important component of the FED. There is a degradation in the cathodoluminescence (CL) generated in the ZnS phosphor as the electron exposure time increases. This is the result of a non-luminescent ZnO layer that forms on the surface according to the electron stimulated surface chemical reaction (ESSCR) model [8, 9, 10, 11,

12]. According to this model the electron beam that is used to irradiate the powder dissociates surface absorbed molecular species (e.g. H_2O, H_2 or O_2) converting them into reactive atomic species which rapidly combine with S to form products with high vapour pressures, such as SO_x or H_2S which desorbs from the surface. XPS measurements [8, 15] indicated that this oxide was ZnO.

Although this CL degradation is also present in CRTs, the effect is much more pronounced in FEDs due to the weak vacuum conditions and the low energy of the excitation electrons. Both these factors are intrinsic to FEDs. The weak vacuum is a result of the large area to volume ratio inside the display and the subsequent extensive degassing from the surface, while the use of low energy electrons is a prerequisite to expand FEDs into the market for portable devices having a low power consumption. The weak vacuum conditions increase the concentration of ambient gases and therefore the reactants to facilitate ZnO growth. The energy loss of the low energy electrons, with their shallower penetration depth, is much more affected by the ZnO layer on the surface of the ZnS phosphor powder. Since there is a direct relationship between the amount of energy loss in the ZnS phosphor and the generated photons, a decreased energy loss in the ZnS results in a decrease in the CL intensity.

In the following chapters the effect the growth of a ZnO layer on the surface of the ZnS phosphor has on the CL intensity is studied using the Monte Carlo simulation technique and then compared to experimentally measured data. Using this simulation method the trajectories of the low energy electrons in the ZnO layer and ZnS bulk can be simulated. An energy loss is associated with each electron trajectory which depends on the electron's energy and the type of atom it is scattered from. From these energy losses a quantitative value for the CL intensity can be obtained. Repeating the simulation for different ZnO thicknesses, a curve is obtained describing the CL intensity as a function of the oxide thickness. From this curve, comparisons can be made with experimentally measured oxide thicknesses after the phosphor powder was degraded to certain values.

2.2 CL degradation of sulfides

Itoh et al. [13] studied the mechanism of degradation of ZnS and ZnCdS phosphors at low voltages and showed the desorption of sulfur containing species. This desorption was found to be related to the power density of the electron beam and also to the increased decomposition of water on the surface of the phosphors at increased partial pressures of water vapor. One drawback of these experiments was that the power densities used were those of the vacuum

fluorescent displays, which are generally higher than those found in FEDs [14].

Similar conclusions about the effects of the partial pressures of the reactive gas were drawn by Swart et al. [8] for ZnS:Cu and ZnS:Ag powder phosphors in simulated FED operating conditions. Degradation of these standard CRT phosphors was studied by using Auger electron spectroscopy (AES) and CL spectroscopy. The Auger results showed that both C and S were depleted from the near surface region of the phosphor while the O and Zn surface concentrations increased. It was suggested that the near surface region of the ZnS phosphor was converted into a sulfur-depleted, oxygen-rich compound, such as ZnO or $ZnSO_4$.

Using XPS analysis, Itoh reported that $ZnSO_4$ was formed on the surface of ZnS and ZnCdS when it was degraded by an electron beam, while Swart et al. reported the formation of ZnO on the surface [8, 15]. Comparing the AES data with the CL data, Swart et al. suggested that a direct correlation existed between the decrease in CL intensity and the extent of surface reactions. The formation of a non-luminescent ZnO surface layer was demonstrated by sputter depth profiles taken after total coulomb exposures of 28 C/cm^2 and 38 C/cm^2 and found to be 1.8 nm and 3 nm respectively.

Kingsley and Prener [16] examined the CL efficiency of ZnS:Cu phosphor particles onto which non-luminescent ZnS of known thickness was deposited. They found that for non-luminescent coatings up to 400 nm thick, the CL efficiency was dominated by the power loss of the electron beam in the non-luminescent layer. Furthermore, the results suggested that the dependence of efficiency on accelerating voltage is dominated by the power loss of the electron beam in the non-luminescent layer and not by changes in the internal efficiency of the phosphor itself.

On the theoretical side, Toth and Phillips [17] approximated CL generation in GaAs using total electron energy loss profiles. These profiles were determined with CASINO, a publicly available Monte Carlo code simulating electron trajectories [18, 19, 20, 21]. The CL intensity was obtained by integrating the energy loss profile along the entire depth of the electron interaction volume. No accommodation was made for the optical losses suffered by the generated photons. However, the experimental results agreed closely with the simulated CL intensity values. A more descriptive model for GaAs was proposed by Phang et al. [22] calculating the excess carrier distribution using the Monte Carlo method and accounting for optical losses of photons both within the semiconductor and at the semiconductor-air interface. The energy loss profiles were similar to that presented by Toth et al.

2.3 Aim: Quantifying the CL intensity

As a first approximation the quantitative simulation of the CL intensity of CL generated inside the ZnS phosphor powder can be addressed as three separate aspects: the incident angle of electrons into the powder particles, the energy loss of electrons in the phosphor and finally the photon generation. In the following paragraphs, each of these aspects will be discussed in detail. Two of these three problems are addressed using the Monte Carlo method. A brief description of this powerful statistical method is given in *Appendix A*. In Paragraph 2.3.1 the Monte Carlo method is used to randomly distribute electron paths over a model surface of the powder according to a Gaussian probability density function. In Paragraph 2.3.2 the method is used to simulate the trajectories and energy loss of electrons in the ZnS phosphor powder.

2.3.1 The incident angle of the electron beam

Firstly, the powder does not have a uniform flat surface, but consists of a random distribution of spherical and flat grains or particles. Therefore the effective thickness of the growing ZnO layer on the ZnS particle will vary according to the exact position of the electron beam on the particle's surface. The difference between the effective thickness z_{eff} of an overlayer on a spherical particle and the overlayer's radial thickness z as experienced by an electron beam is illustrated in Figure 2.3.1. Only the top half of each phosphor powder particle is simulated, due to the limited penetration depth of low energy electrons. An increase in the incident angle θ will lead to an increase in z_{eff} and the subsequent energy loss in this layer. In Figure 2.3.1 the effective thickness as function of the radial thickness and incident angle of an electron beam is shown. For thin overlayers the effect of increasing the incident angle is less dramatic but as the thickness of the layer and the incident angle increases, the effective thickness becomes quite large.

To take into account the effect that the phosphor powder's morphology has on the energy loss process, a Monte Carlo simulation on the interaction between the electron beam and the ZnO/ZnS powder particles was performed to determine the angular distribution of the incident electrons. These results are presented in *Chapter 3*. Using these results a comparison was made between the energy loss in the ZnS as a function of the ZnO thickness with and without the angular distribution. The effect the ZnO layer has on the energy loss in the ZnS phosphor powder is therefore effectively simulated.

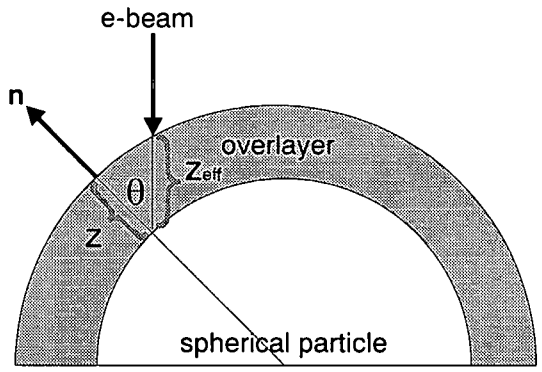

Figure 2.1: The difference between the effective overlayer thickness z_{eff} as encountered by an electron beam and the radial thickness z of an overlayer covering a spherical particle. The angle between the direction of the electron beam and a vector normal to the surface is θ.

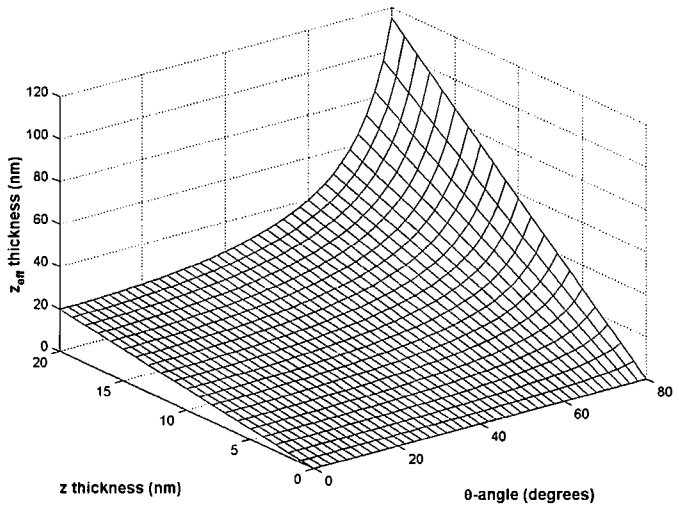

Figure 2.2: The effective thickness of a overlayer z_{eff} on a spherical particle as function of the radial overlayer thickness z and the angle θ between the incident electron beam and the surface normal. Results are only plotted up to 80^o because the effective thickness increases to infinity as the angle increases to 90^o.

2.3.2 The electron's energy loss inside the phosphor

Secondly, as the electron travel through the powder, it loses energy to the solid. The trajectories as well as the energy loss along these trajectories can be accurately simulated using the Monte Carlo technique. Such a code was developed using very recent models to describe the scattering angles and step length of electrons between scattering events. The electron beam's incident angle distribution was used in the simulation to accommodate the phosphor's morphology. The concept of a diffusion interface between the ZnO layer and ZnS bulk was also introduced. In *Chapter 4* energy loss profiles for different ZnO thicknesses were determined when the powder is irradiated by 2 keV electrons. This beam energy was used in the simulation since the experimental degradation measurements were performed at an electron beam energy of 2 keV.

2.3.3 The generation of photons

Thirdly, the energy that the electrons lost in the phosphor powder generates electron-hole (e-h) pairs that can recombine either radiatively or non-radiatively. In the case of radiative recombination in the ZnS phosphor photons are generated and propagate in all directions. Only a small fraction of these photons emerge from the surface, resulting in the measured CL intensity. In *Chapter 5* an expression is derived to calculate a normalized value for the CL intensity using the energy loss profiles determined in Chapter 4.

Chapter 3

The electron beam's incident angle

3.1 Introduction

As was mentioned in the previous chapter the phosphor powder does not have a uniform flat surface, but consists of a random distribution of flat and spherical shaped grains. The effect oxide growth around these powders has on the energy loss process of electrons was also explained. In this chapter a Monte Carlo simulation was performed to simulate the interaction between the electron beam and the powder particles to obtain a distribution of incident angles. Using this angular distribution a comparison was made between the energy loss in the ZnS as a function of the ZnO thickness with and without the angular distribution using the CASINO code. It is a single scattering Monte Carlo simulation for low energy beam interaction, employing tabulated elastic Mott cross sections calculated from relativistic Hartree-Fock-Slater atomic potentials and the modified Bethe energy loss equation. Zhang et al. [23] used a different approach to simulate the CL excitation process in phosphor particles by extending the one dimensional electron generation function, determined by Everhart and Holf [24], to three dimensions in nanocrystalline structures.

A JEOL 6400 WINSEM Scanning electron microscope was used to image the powder at an acceleration energy of 5 keV. The sample holder consisted of a copper platelet with a 1mm hole drilled 0.5 mm into the metal. The phosphor powder was compacted into this hole. The phosphor consists of particles with a bimodal size distribution between 1.4±0.3 μm and 4.5±0.5 μm. The bigger particles are flat and elongated up to 10 μm in one direction. SEM images of the phosphor powder at different magnifications are shown in Section 3.3.

The simulations performed in this chapter are based on experimental results from previous

phosphor studies [8, 9, 25]. In these studies a PHI model 549 Auger system was used to determine the influence of various parameters on the degradation process. Both CL and Auger electrons were excited by the same electron beam and different sets of data were collected simultaneously. The electron beam size and shape would play an important role in the simulations. The electron beam profile was determined by measuring the electron beam current while moving the edge of the Faraday cup perpendicular to the electron beam. The experimental data of the beam current as function of the distance moved by the edge of the Faraday cup, Figure 3.1(a), is then differentiated and plotted, Figure 3.1(b). The diameter of the electron beam was determined as 67 μm taken as the full width at half maximum (FWHM) at a primary electron energy of 4 keV. Although the simulations and degradation experiments were performed at a beam energy of 2 keV, the 4 keV beam profile was only used to fit a mathematical function to after which the function's parameters were changed to accommodate different beam profiles. A Gaussian function was fitted to the experimentally measured electron beam profile and used to distribute electron incident positions over the phosphor surface during the simulation. The incident angle between the electron beam and a vector normal to the surface of the phosphor particle was then calculated for a large number of electron trajectories to obtain an angular distribution.

Both flat and spherical particles were modeled and from a combination of the incident angle distributions for these two types, a probability density function was obtained. This function was then used to calculate the energy loss in ZnS as function of the ZnO thickness and the particle's morphology using the Monte Carlo code.

3.2 Distributing electrons over a surface

Electrons from a static electron beam irradiating any surface are not uniformly spread over the beam area, but are concentrated in the center of the beam as seen by the profile of the measured beam in Figure 3.1(b). A Gaussian function describes this distribution well. To model the electron beam irradiating the phosphor powder, a large number of electron paths are spread over a plane according to a one dimensional Gaussian function applied in both lateral directions. To distribute the electrons across the beam diameter according to this distribution, a Gaussian function, for example:

$$f(x) = \frac{2}{\sqrt{\pi}} e^{-x^2} \tag{3.1}$$

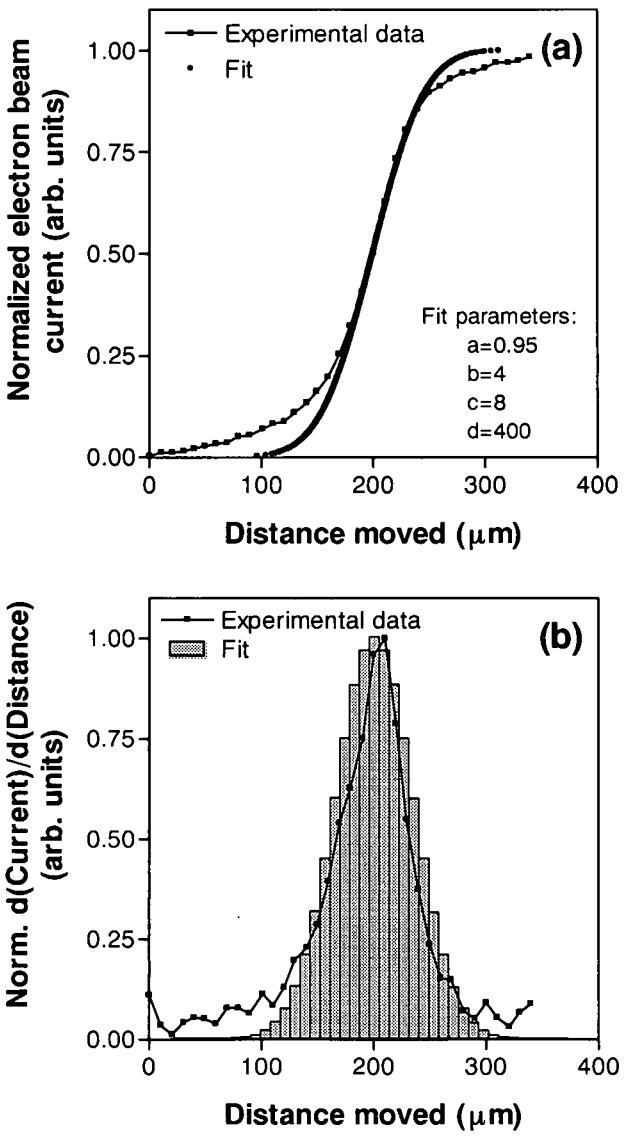

Figure 3.1: The normalized electron beam current (a) and the differentiated current (b) as function of the moving distance of the Faraday cup edge at a primary electron energy of 4 keV. In (a) Equation 3.7 is fitted to the experimental data. In (b) a comparison between the experimental data and a histogram of these generated values is shown.

may be used as a probability density function to sample using random numbers between 0 and 1. The following expression returns the probability $P \in [0,1]$ of finding the value x in the interval $[-\infty, t]$:

$$P = \frac{\int_{-\infty}^{t} f(x)dx}{\int_{-\infty}^{\infty} f(x)dx} \tag{3.2}$$

where $f(x)$ is a probability density function. To apply the Monte Carlo technique to Equation 3.1, Equation 3.2 can be expressed as:

$$P = \frac{\int_{-\infty}^{0} f(x)dx + \int_{0}^{t} f(x)dx}{\int_{-\infty}^{0} f(x)dx + \int_{0}^{\infty} f(x)dx} \tag{3.3}$$

and according to the definition of the error function:

$$erf(t) = \int_{0}^{t} \frac{2}{\sqrt{\pi}} e^{-x^2} dx \tag{3.4}$$

using the mathematical identity $\int_a^b g(x)dx = -\int_b^a g(x)dx$, Equation 3.3 then simplifies to:

$$P = \frac{1 + erf(t)}{2} \tag{3.5}$$

To generate the values of t, Equation 3.5 can be rearranged so that:

$$t = erf^{-1}(2P - 1) \tag{3.6}$$

which returns a value for $t \in [-4, 4]$ for any given random number P between 0 and 1.

To apply this technique to simulate the measured electron beam profile, Equation 3.6 must be fitted with the necessary parameters to the experimental data in Figure 3.1(a):

$$t = [\frac{\frac{erf^{-1}(2P-1)}{a} + b}{c}]d \tag{3.7}$$

where a, b, c and d are fit parameters. To obtain the fit in Figure 3.1(a), Equation 3.7 was sampled 10^3 times with random numbers. Increasing the value of a increases the slope of Equation 3.7 which in turn decreases the spread of the beam. This parameter will be referred to as the *Beam shape* parameter. Parameter d determines the maximum lateral area over which

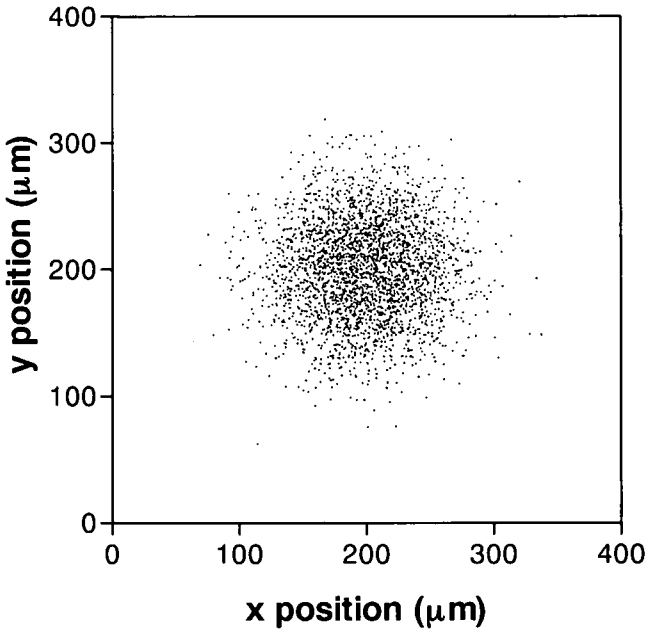

Figure 3.2: A two dimensional spread of (x, y) points generated using Equation 3.7 and the fit parameters given in Figure 3.1(a) applied to both the x- and y-directions.

the beam is spread and is referred to as the *Total beam diameter*. This parameter should not be confused with the FWHM beam diameter. Parameters b and c are only introduced to normalize the distribution. The values of these 4 parameters are also given in Figure 3.1(a). Although the fit is not perfect, the slopes of the fitted equation and the experimental data coincide well. The misfit at the edge can be attributed to the effects introduced by the physical form of the Faraday cup, especially the shape of the cup's opening and it's relative small size compared to the diameter of the electron beam. In Figure 3.1(b) a normalized histogram of the generated t values are shown plotted over the normalized differentiated electron beam current. A total number of 10^5 t values were generated for this histogram. The maxima of the profile and the histogram do not coincide, but can be attributed to an asymmetric experimentally measured beam profile. The rest of the histogram fits the profile well, except at the edges were the electron current does not decrease to zero. This may be attributed to the misfit seen in the slope edges in Figure 3.1(a). To extend this distribution into two dimensions, Equation 3.7 has to be applied to both the x and y directions. From this a spread of (x, y) points can be generated over a 400 μm $\times$ 400 μm area following a Gaussian distribution as seen in Figure 3.2.

3.3 Modeling the surface morphology

In Figure 3.3 a SEM image of the P22G phosphor powder at low magnification is shown. The streaking across the image is due to charging effects of the semiconducting phosphor when the electron beam scans across the surface. At this low magnification, the morphology of the individual powder particles is not clearly visible.

In Figure 3.3 and 3.3 more SEM images of other areas at higher magnifications are shown . These locations were chosen to the side of the sample holder where the powder layer is more thinly spread around the edges. The streaking in the images are less visible due to the improved conducting properties between the powder and the copper sample holder. In these two images both flat and spherical powder particles are visible. Both types of particles are randomly distributed over the surface.

Certain basic assumptions were made to model the surface morphology. The spherical phosphor particles are assumed to be perfect spheres with an average diameter of 2 μm. The other group of particles is assumed to be perfectly flat and orientated randomly in any direction between 0 and 90^o with respect to the incident direction of the electron beam. The assumption is made that each shape's area, flat or spherical, contributes 50% to the total area irradiated by the electron beam. In the experimental setup, the sample is orientated at a 30^o angle to the incident electron beam while the simulations are performed at a 0^o angle. Since half of the particles are assumed to be perfect spheres, the radius of curvature and the distribution of electron beam incident angles are the same for any sample orientation direction. Furthermore, the spheres are packed into an ordered structure only for the simulation and any shadowing effects that may occur should be ignored. In the experimental setup the spherical grains are randomly distributed and any area that is shadowed from the electron beam will not contribute to the generated CL. The same argument also holds for the flat particles which are randomly orientated with respect to the electron beam.

A simple calculation can be made to determine the angle between the direction of the electron beam and a vector normal to the surface of the spherical particle. In Figure 3.3 such a possible incident angle is shown when an electron penetrates the surface of the particle. If the electron path is represented as an unit vector $\mathbf{e}$ in the z-direction and the vector normal to the surface as $\mathbf{a}$ then the direction cosine between these two vectors can be expressed as:

$$cos(\theta) = \frac{\mathbf{a} \cdot \mathbf{e}}{\mid \mathbf{a} \mid\mid \mathbf{e} \mid} \tag{3.8}$$

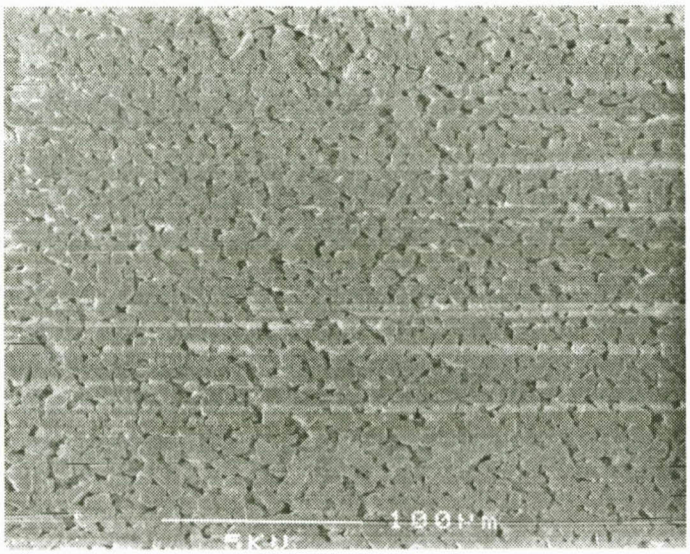

Figure 3.3: A 372 μm $\times$ 278 μm SEM image of the compacted P22G phosphor powder at low magnification revealing the surface morphology. The streaks across the image are due to a surface charging effect.

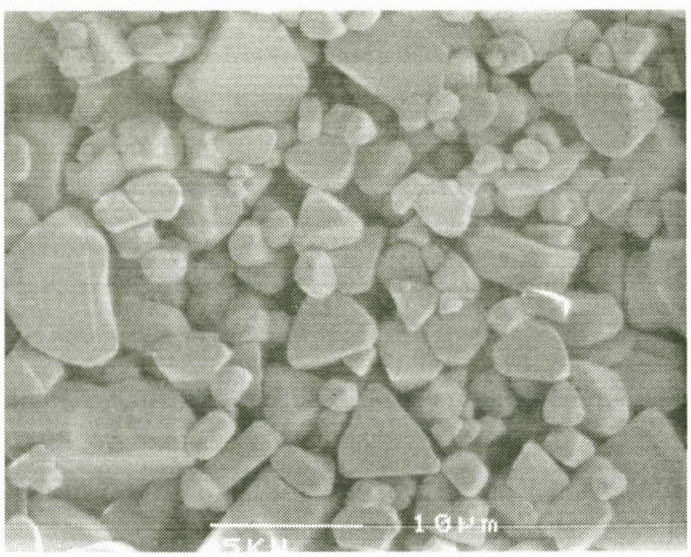

Figure 3.4: A 49 μm $\times$ 36 μm SEM image showing the P22G phosphor powder at a high magnification. Two groups of particles can be identified in the image: flat and spherical particles with both being randomly distributed over the surface.

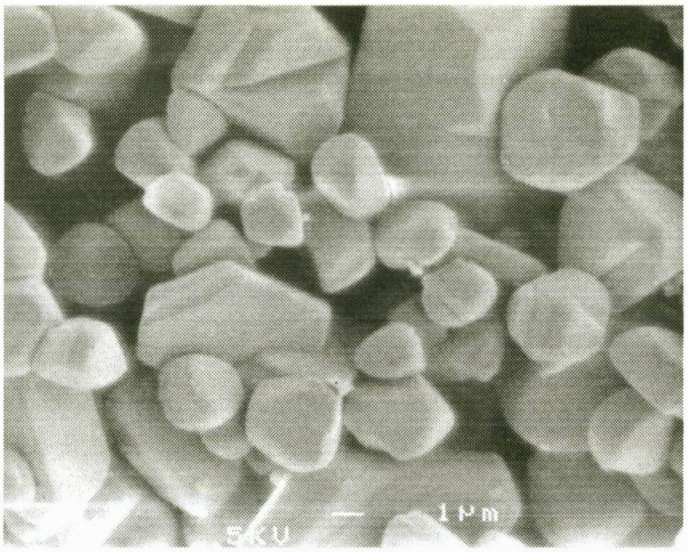

Figure 3.5: A 24 μm $\times$ 18 μm SEM image showing another area of the P22G phosphor powder at a high magnification.

But vector **a** is in the same direction as the position vector **b** and since **e** is a unit vector:

$$cos(\theta) = \frac{b_z}{\sqrt{b_x^2 + b_y^2 + b_z^2}} \tag{3.9}$$

with b_x, b_y and b_z the components of vector **b** between the origin of the sphere $(x_1, y_1, 0)$ and the incident position (x_r, y_r, z_r) so that:

$$cos(\theta) = \frac{z_r}{\sqrt{(x_r - x_1)^2 + (y_r - y_1)^2 + z_r^2}} \tag{3.10}$$

But the denominator in Equation 3.10 is equal to the radius of the sphere r so that:

$$cos(\theta) = \frac{z_r}{r} \tag{3.11}$$

To determine the incident angle for a sphere with a known radius only z_r must be known, with x_r and y_r determined with the technique described in Section 3.2. This can be readily calculated from these values using the equation for the sphere.

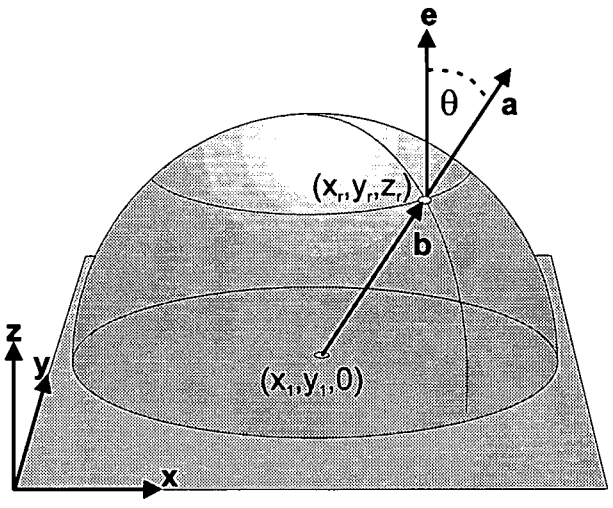

Figure 3.6: To determine the angle θ between the electron beam's direction and a vector normal to the surface on a spherical particle, the direction of the electron beam can be represented by a unit vector e and the surface normal vector as a.

3.4 Determining the angular distribution

Although the SEM images in Figure 3.3 and 3.3 clearly show that the spherical particles are randomly distributed over the surface, the exact position of a single sphere under the electron beam is irrelevant as long as enough spheres are simultaneously irradiated by the electron beam, resulting in as many different θ-angles as possible. This implies that the spheres can be arranged in any ordered fashion during the simulation to determine the angular distribution.

In Figure 3.4 the interaction between 10^4 electron paths and 100 spheres arranged in an ordered fashion is shown. Each sphere has a 2 μm diameter and covers a total area of 20 μm $\times$ 20 μm. A perspective and top view of the spheres, shows the distribution of incident positions over the different spheres' surfaces. The *Beam center offset* refers to the center displacement of the beam. In this case the value is (1,1) which indicates that the beam was displaced 1 μm in the x-direction and 1 μm in the y-direction, from the midpoint position (10 μm,10 μm). At this position the beam is centered on a sphere rather than on the gap between the spheres. For this simulation, the *Total beam diameter* was set to 2 μm, spreading the electron beam over the entire effective area of a single sphere and the *Beam shape* parameter was set to 0.95, the same value as for the fit shown in Figure 3.1(a). The percentage of electrons that did not interact with the surface of the sphere, in other words the electrons that fell in the

gaps between the spheres, is given by the *No interaction* value. In this case the value is zero which visually corresponds to the distribution of electron interactions in the 2D view.

The angle between each incident electron path and the surface normal of a sphere was determined with the technique described previously in Section 3.3. A histogram was determined from the results, using 18 bins, each 5^o wide and spread between 0 and 90^o. These results, the *Interaction fraction* as function of the incident angle, are displayed in Figure 3.4. The *Interaction fraction* is obtained by dividing the histogram's frequency by the total number of simulated paths. The density of electron interactions increases from 0^o and reaches a maximum in the region of 10^o. The density then rapidly decreases to zero as the incident angle increases further. This is because the greatest part of the distributed incident positions fall on the top region of the sphere, where the incident angle is small.

In Figure 3.4 the simulation was repeated with the same focus parameter, but the beam's range was increased to 10 μm, covering the effective area of 25 spheres. Note that in the figure it appears as though only a total of 9 spheres are irradiated, but this is due to the Gaussian spread and the limited number of simulated electron paths. Due to the gaps between the spheres, the *No interaction* value increased to 20.01%. In the histogram the density of electron interactions reaches a maximum at incident angles between 40 and 50^o and then decreases to 0 as the angle increases to 90^o. The change in distribution compared to the previous histogram is due to the larger number of spheres irradiated and the subsequent improved statistical results.

In Figure 3.4 the simulation was repeated again with the same *Beam shape* parameter, but increasing the *Total beam diameter* to 20 μm. The No interaction value increased to 21.43%. Although the ratio between the sphere's effective surface and the area of the gaps between the spheres is linearly dependant, the non-uniform distribution of incident positions lead to the non-linear increase of this value. The histogram is similar to the one in Figure 3.4, with the maximum around 45^o.

The histogram's shape and the position of the maximum can be attributed to the density of the electron interactions spread over the sphere and is directly related to the sphere's effective surface exposed to the electron beam. A surface area element dA on the sphere, Figure 3.4, has the expression:

$$dA = 2\pi r^2 sin(\theta) d\theta \tag{3.12}$$

However, the effective area presented to the incident electron beam dA_{eff} is a horizontal projection of the area dA and can be expressed in terms of the area element dA and the

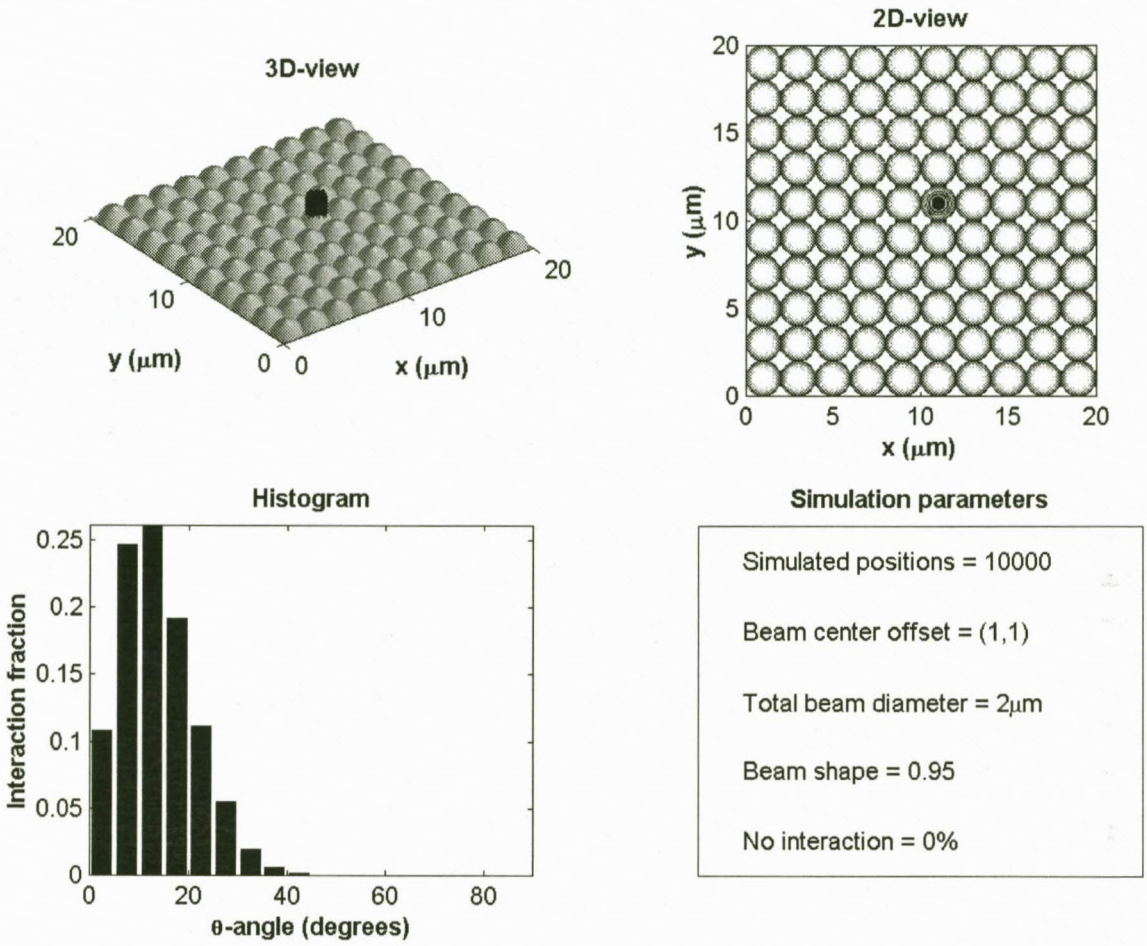

Figure 3.7: **A simulation visually showing the interaction between 10^4 electron paths and 100 spherical particles each with a 2 μm diameter. The Total beam diameter and Beam shape was set to 2 μm and 0.95, spreading the electron beam over the effective area of a single sphere. The shape value was kept as the fit to experimentally measured beam profile in figure 3.1(a). The distribution of incident angles over the surface of the single sphere is displayed in the histogram.**

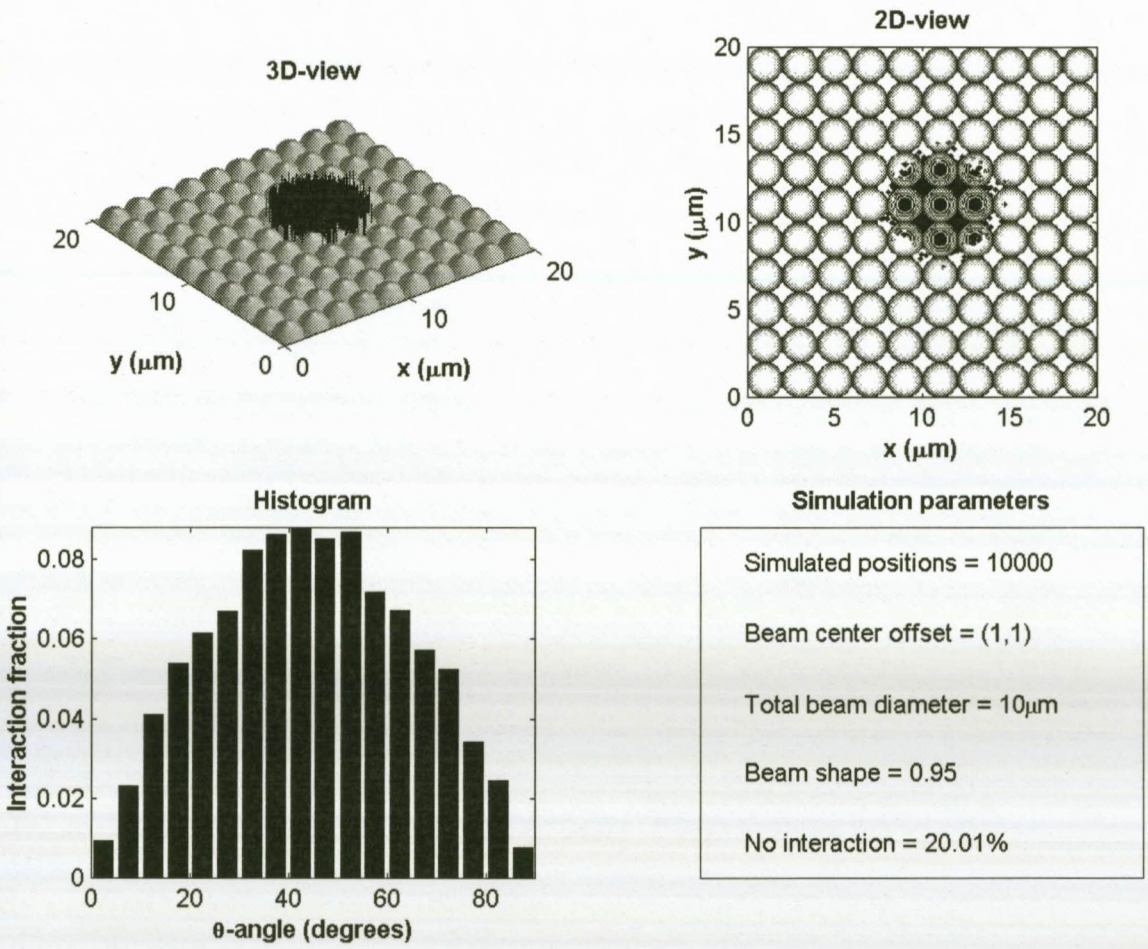

Figure 3.8: The simulation showed in figure 3.4 was repeated with the same Beam shape parameter, but the Total beam diameter was increased to 10 μm, covering the effective area of 25 spheres. The distribution of incident angles over the surface is displayed in the histogram.

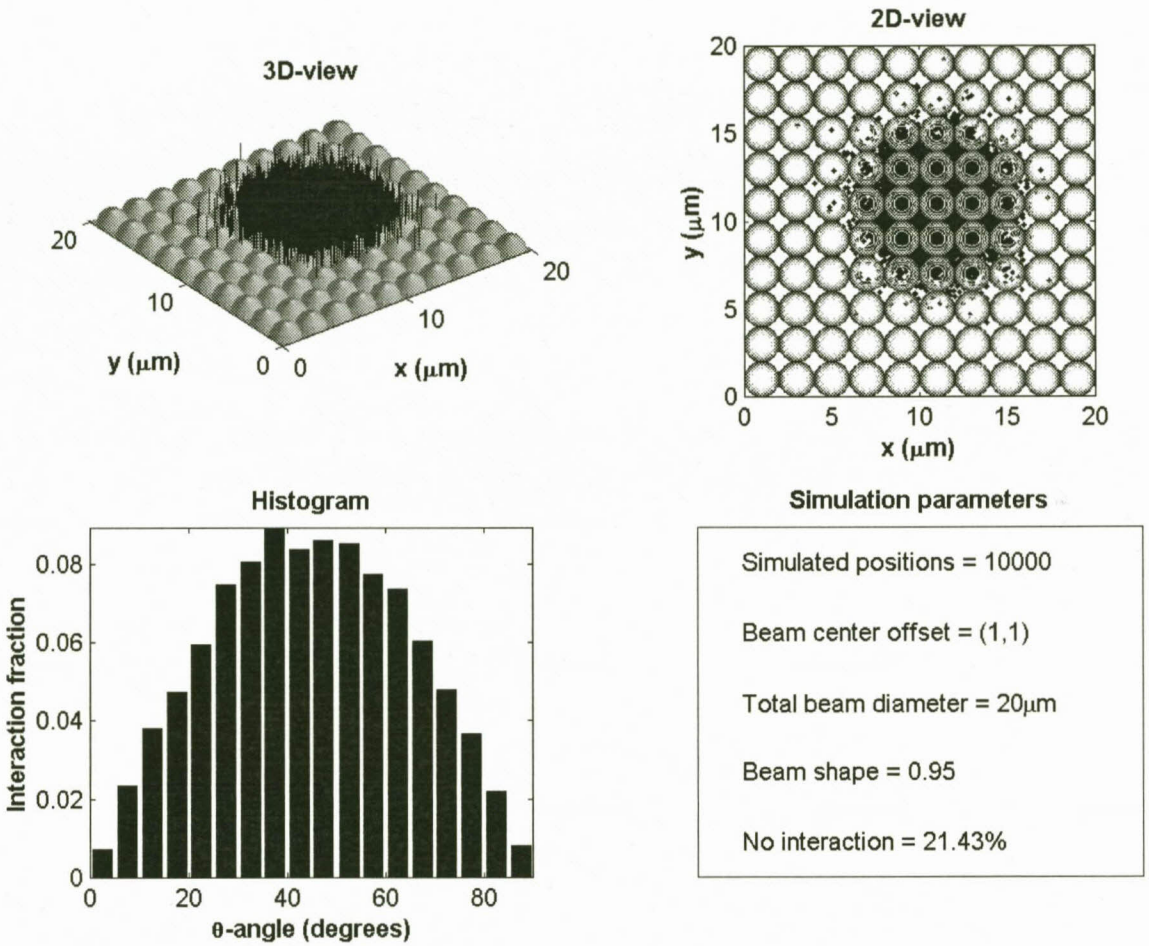

Figure 3.9: The simulation shown in figures 3.4 and 3.4 was repeated, again with the same Beam shape parameter, but the Total beam diameter was increased to 20 μm, covering the whole effective area of the 100 spheres. The distribution of incident angles over the surface is displayed in the histogram.

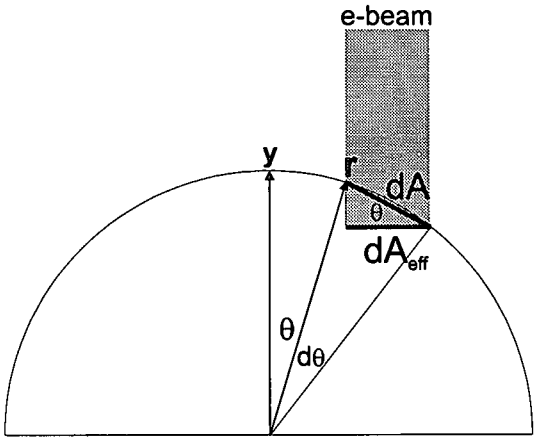

Figure 3.10: A side view of a sphere with radius r illustrating the relationship between the surface area element dA and dA_{eff}, the effective surface area element exposed to the electron beam.

incident angle θ:

$$dA_{eff} = dA \times cos(\theta) \tag{3.13}$$

Using this expression, Equation 3.12 becomes:

$$dA_{eff} = \pi r^2 sin(2\theta) d\theta \tag{3.14}$$

using the trigonometric identity $sin(2\theta) = 2sin(\theta)cos(\theta)$. If the assumption is made that the fraction of electron paths interacting with the sphere's surface is proportional to the effective surface area element dA_{eff}, the *Interaction fraction* df can be expressed as:

$$df = k \times dA_{eff} \tag{3.15}$$

where k is a proportionality constant. Substituting Equation 3.14 into Equation 3.15 reveals that the *Interaction fraction* should be a sine function of the incident angle with a half period of 90°. This corresponds to the shape of the histogram seen in Figure 3.4. This expression also reveals that the *Interaction fraction* has a maximum value when θ is 45° and correlates with the results obtained in the simulation.

3.5 The non-uniform growth of the oxide layer

As previously mentioned the growth of the oxide layer is stimulated by the impingement of electrons onto the surface of the ZnS phosphor powder. Thus the rate of oxide growth should be proportional to the current density of the electron beam. Considering the spherical shaped grains and the effective area exposed to the electron beam, the current density varies across the surface of the powder. Referring back to Figure 3.4, the ratio of the exposed area dA, Equation 3.12, to the effective area dA_{eff}, Equation 3.14, a measure of the normalized exposed area, is given by:

$$\frac{dA}{dA_{eff}} = \frac{1}{cos(\theta)} \tag{3.16}$$

The current density is defined as the current per unit area or I/A with I the current and A the area. Since the beam current remains constant over the surface area of the sphere, the rate of oxide growth is inversely proportional to the normalized exposed area. In Figure 3.5 a graph is shown indicating the normalized rate of oxide growth for a spherical particle with a unit radius. At the top of the sphere, the normalized exposed area is the smallest and therefore the beam current density is the highest. This may result in the fastest oxide growth. To the sides of the sphere, the normalized exposed area increases and the current density decreases. Lower current densities may however lead to a higher surface reaction rate [26] due to a lower local temperature on the surface of the phosphor powder. This may lead to an increase in the surface reaction rate due to the longer time spent by absorbed molecules on the surface, resulting in a direct increase of the ESSCR probability.

As the thickness of the oxide layer around the particle increases, the rate of oxide formation should decrease since the reaction is localized to the ZnS phosphor surface itself. It is further unknown whether the oxide formation is a reaction or diffusion controlled process. Although the angular distribution can be modified to accommodate this non-uniform oxide growth, in the absence of sufficient experimental measurements for the purposes of this study, it's effect was ignored and it was assumed that the oxide layer around the particle has a uniform thickness.

3.6 Factors influencing the angular distribution

The influence of the electron beam's profile on the angular distribution should also be determined. By adjusting the a and d parameters in Equation 3.7 the beam's profile can be

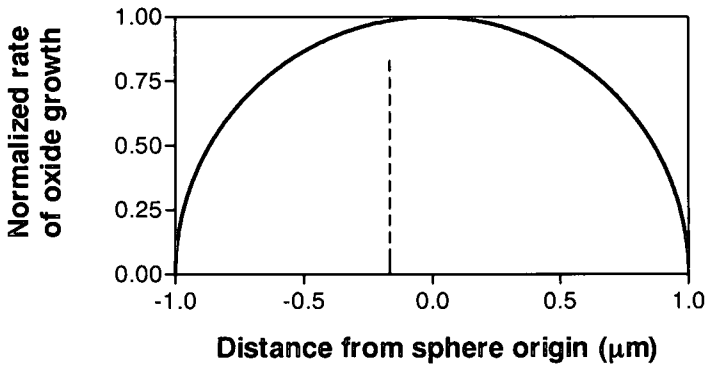

Figure 3.11: The normalized rate of oxide growth for a spherical particle with a unit radius as function of the sphere's diameter. At the top position of the sphere the current density is the highest and therefore the rate of oxide growth the fastest. To the side of the sphere, the current density is lower and the rate slower.

changed. In Figure 3.6(a) and 3.6(b) the effect of changing these parameters on the electron beam profile is shown with the FWHM beam diameter as function of the (a) *Total beam diameter* at a constant *Beam shape* parameter of 0.95 and (b) *Beam shape* at a constant *Total beam diameter* of 10 μm. In Figure 3.6(a) the FWHM beam diameter increases linearly with an increase in the *Total beam diameter* while in Figure 3.6(b) it decreases exponentially with an increase in the *Beam shape* parameter. The Monte Carlo simulations performed in Section 3.4 were then repeated to investigate the influence these two parameters have on the angular distribution.

In Figure 3.6 the *Interaction fraction* as function of the incident angle is given for various *Beam shapes*. Beam profiles associated with the shape parameter are also shown in the inset. As this parameter is decreased from 2 to 0.4 the distribution of incident angles converge towards that seen in the histogram in Figure 3.4 and predicted by Equation 3.15.

In Figure 3.6 the *Interaction fraction* as function of the incident angle is given for various *Total beam diameters*. A selection of beam profiles at various *Total beam diameters* are shown in the inset. When the *Total beam diameter* is set to 2 μm, the distribution corresponds to the histogram seen in Figure 3.4 because only one sphere is irradiated. As this value is increased, the distribution again converges towards to that seen in Figure 3.4's histogram and predicted by Equation 3.15.

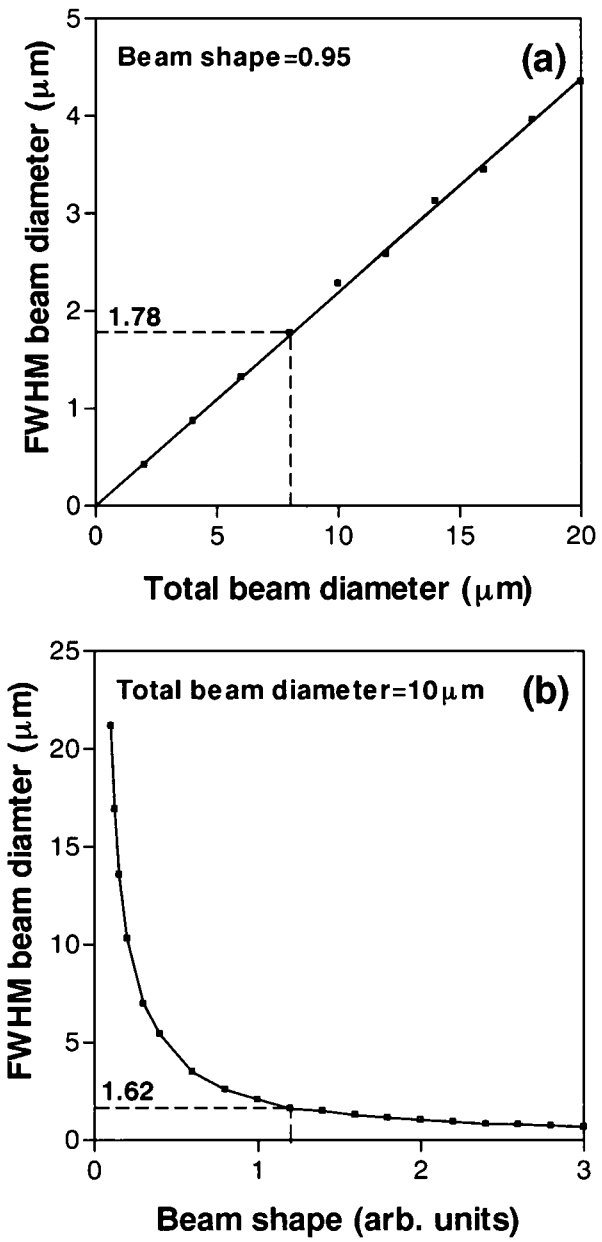

Figure 3.12: The FWHM beam diameter as function of (a) the Total beam diameter and (b) the Beam shape.

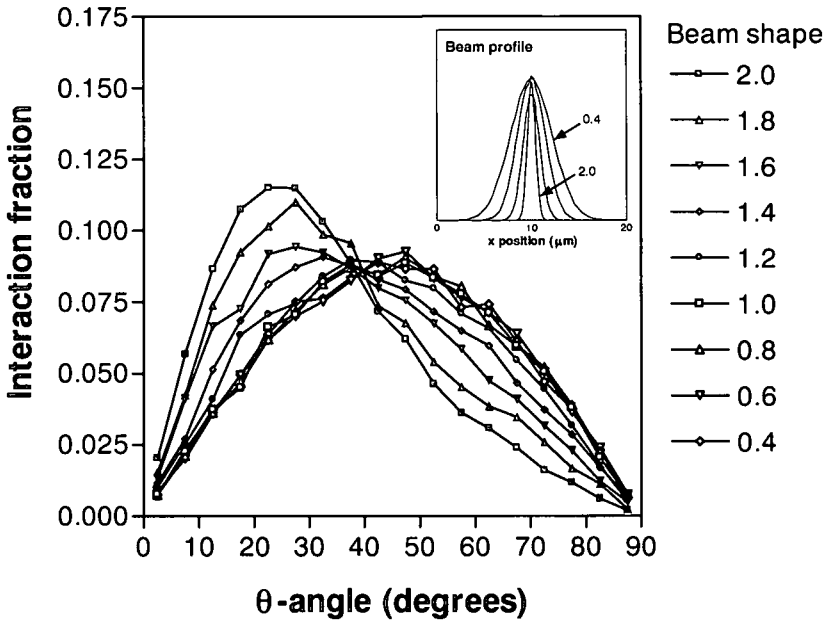

Figure 3.13: The interaction fraction as function of the incident angle θ for different Beam shape parameters. The Total beam diameter was kept constant at 10 μm and the simulation was performed using 10^4 electron paths. A selection of beam profiles at different shape-parameters are shown in the inset.

A very distinct feature in Figures 3.6 and 3.6 is that the angular distribution converges when the *Beam shape* parameter is decreased and the *Total beam diameter* is increased above certain values. In Figure 3.6 this takes place when the parameter is set to values smaller than 1.2 and in Figure 3.6 when set to values greater than 8 μm.

Comparing these values with the FWHM beam diameter shown in Figure 3.6(a) and (b), reveals that the minimum FWHM beam diameter to obtain this convergence is 1.78 and 1.62 μm respectively, which is in the same order as the sphere's diameter of 2 μm used in these simulations. Changing the beam's profile thus only influences the distribution of the incident angles if the FWHM beam diameter is smaller than the size of the irradiated particle. The larger the beam diameter, the more spheres are irradiated and the better the statistical results obtained from the simulation. Although the maximum value for the *Total beam diameter* used in these simulations were limited to 20 μm, the beam already interacts with enough spheres at a shape parameter of 0.95 to deliver a good statistical result. In the experimental setup the FWHM beam diameter of the electron gun used to irradiate the phosphor powder was in the

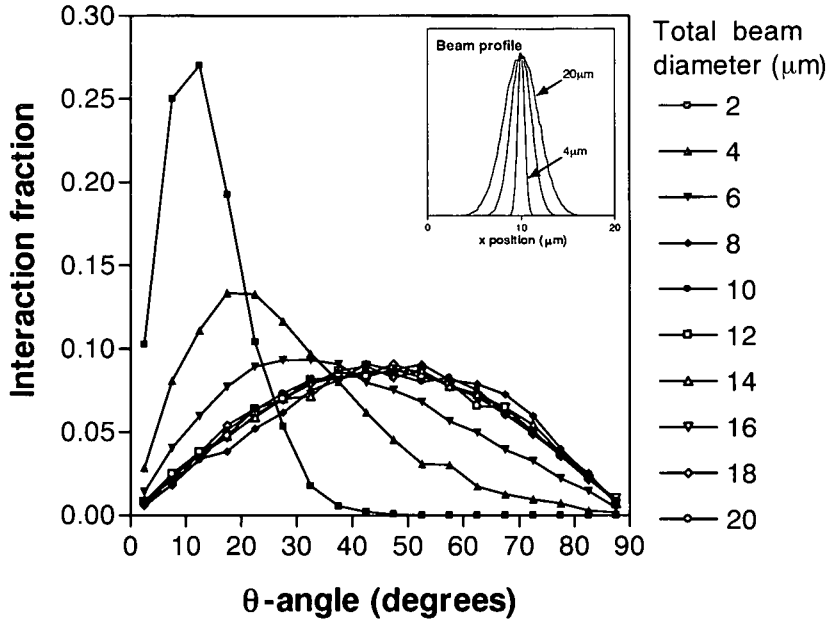

Figure 3.14: The interaction fraction as function of the incident angle θ for different Total beam diameter parameters. The Beam shape was kept constant at 0.95 and simulation was performed with 10^4 electron paths. A selection of beam profiles for different total diameters are shown in the inset.

order of 67 μm (Figure 3.1). According to these results, the angular distribution for this beam should be similar to the convergent angular distribution seen in Figures 3.6 and 3.6.

3.7 Extending the angular distribution to flat particles

Up to now these simulations only dealt with the angular distribution associated with spherical particles. For flat particles, the distribution is much simpler. Since it is assumed that the flat particles are randomly orientated in any direction between 0 and 90^o, the *Interaction fraction* as function of the θ-angle will be constant. Using the same histogram bin width as was used for the simulations involving the spherical particles, the value for the *Interaction fraction* is constant at 0.0556 compared to that seen in the histograms of Figures 3.4 to 3.4. It was further assumed that each group of particles contribute 50% to the total effective area irradiated by the electron beam. In Figure 3.7 the combined angular distribution of the spherical and flat particles was determined by adding half of each particles group's *Interaction fraction* profile.

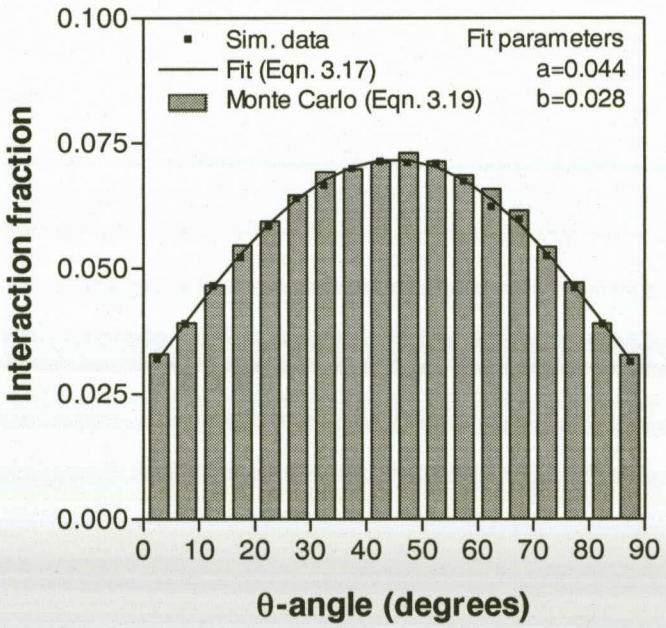

Figure 3.15: **The interaction fraction as function of the incident angle θ for the simulation data (A fitted equation and a histogram). The simulation data originates from the combined results of the spherical and flat particle simulations and the fit on this simulation is from Equation 3.17. The fit parameters are also shown. Using this equation and the Monte Carlo method, a number of θ-angles were generated. The histogram shows the distribution of these angles.**

If a probability density function is obtained that describes this distribution of incident angles, sampling from that function will yield values for the incident angle distributed according to the profile seen in Figure 3.7. To determine a probability density function describing this distribution, the following expression can be used:

$$f(x) = a \cdot sin(2x) + b \tag{3.17}$$

where the first term refers to the contribution of the spherical and the second term to the flat particles' angular distribution. Using the expression in Equation 3.2 and adjusting the lower and upper limits to 0 and 90°, the probability P of locating x in the interval between 0 and t is given by:

$$P = \frac{\frac{a}{2}[1 - cos(2t)] + bt}{a + \frac{b\pi}{2}} \tag{3.18}$$

with $P \in [0, 1]$. To sample values t from this equation using random numbers between 0 and 1, the equation can be rewritten as:

$$cos(2t) - \frac{2bt}{a} = 1 - (2 + \frac{b\pi}{a})P \tag{3.19}$$

This expression has no analytical solution and is solved using the Newton-Rhapson numerical iteration method [27]. In Figure 3.7 a comparison between the simulation data, a fitted equation and a histogram is shown. The simulation data originates from the combined results of the spherical and flat particle simulations and the fit on this simulation is from Equation 3.17 with the necessary parameters for a and b. Using this equation and the Monte Carlo method, a large number of angles were generated. The histogram shows the distribution of these angles which is a good approximation of the previous simulation results.

3.8 The effect of the angular distribution on the energy loss

In Figure 3.7 Monte Carlo simulations of the energy loss in the ZnS phosphor as function of the ZnO thickness *with* and *without* the angular distribution is shown at a beam energy of 2keV using the CASINO code. This corresponds to the two cases where the ZnO layer grows on a flat surface and where it grows on and around a distribution of flat and spherical particles. The profile that does not consider the distribution was determined from the simulated energy

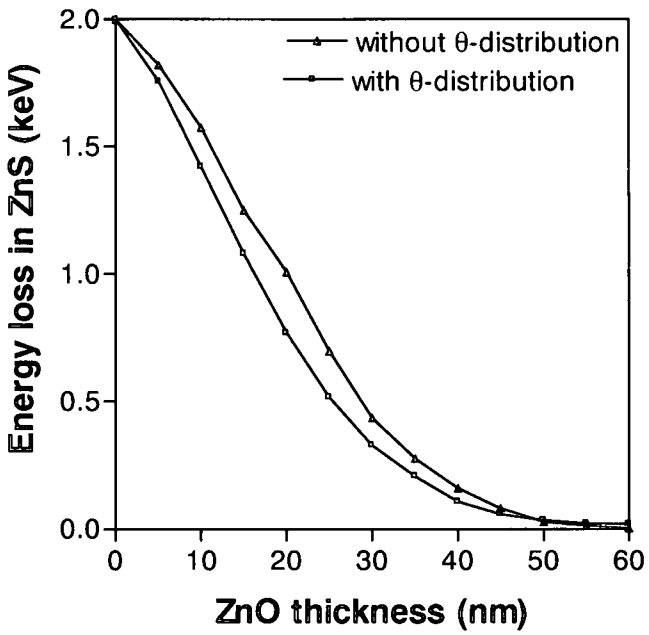

Figure 3.16: Monte Carlo simulations of the energy loss in ZnS phosphor powder as function of the ZnO layer thickness at a beam energy of 2keV. The one profile was determined with and the other one without taking the distribution of electron incident angles into account.

loss values in ZnS at certain ZnO thicknesses and a 0^o electron beam incident angle. The other profile was constructed from the same energy loss values but weighted according to the *Interaction fraction* given by Equation 3.17 at different incident angles spread between 0 and 90^o. In both profiles the energy loss in ZnS decreases exponentially as the ZnO thickness increases. But when the angular distribution is also considered, there is a decreased energy loss in the ZnS, indicating that though the energy loss is primarily due to the growth of the non-luminescent ZnO layer, the morphology of the phosphor powder also effects the degradation.

Chapter 4

The electron trajectories and energy loss

4.1 Introduction

In this chapter a Monte Carlo electron trajectory simulation is used to determine an electron interaction volume and an energy loss profile through the ZnO layer and the ZnS bulk with a diffusion interface between the oxide layer and the bulk. By varying the thickness of the ZnO layer and the diffusion interface, the effect of these parameters on the energy loss profile can be studied in detail at different beam energies.

The Monte Carlo technique used to simulate the electron trajectories in solids is well known and already reported elsewhere by various authors [19, 28, 29, 30]. Therefore only a brief outline of the method, based on the set of questions in the flowchart in Figure 4.1 will be given here. An energetic electron penetrates a solid at an incident angle α and travels a certain distance S before it is scattered by an atom for the first time. In this step length the electron loses a certain amount of energy ΔE. Changing it's trajectory, as shown in Figure 4.1, the electron then travels another distance before it is scattered again. This process is repeated until the electron has lost all it's energy to the solid. The simulation is then repeated until a statistically significant result is obtained. Dividing the electron interaction volume into layers and calculating the energy loss in each of these layers, an energy loss profile can be constructed. The scattering of the electron by an atom is viewed as an elastic scattering event with no energy loss, but changing the direction of the electron trajectory. The distance the electron moves between scattering events is viewed as an inelastic scattering event with a negligible direction

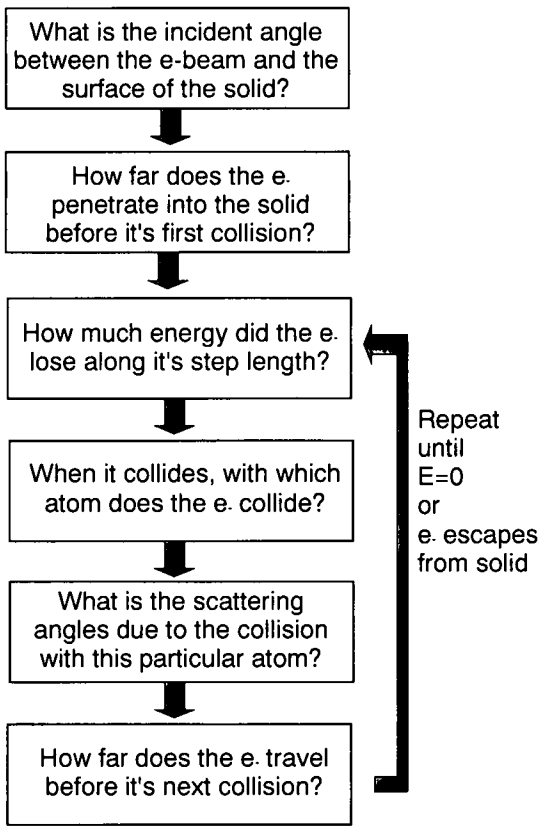

Figure 4.1: A set of questions summarizing the Monte Carlo method used to simulate the trajectory of the single electron in a compound.

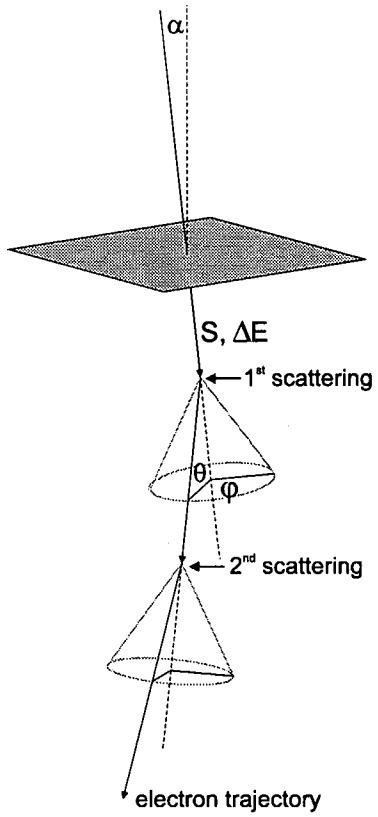

Figure 4.2: A graphical illustration of the change in an electron's trajectory when it penetrates a solid at an incident angle and is scattered by the atoms of the solid.

change.

4.2 Determining the electron's incident angle

The electron's incident angle is determined by the orientation of the electron beam with respect to the surface of the solid. As already discussed in the previous chapter, the ZnS surface is not flat, but consists of a distribution of flat and spherically shaped particles. Greeff and Swart [31] determined the distribution of electron beam incident angles using a Monte Carlo method. During the simulation of the electron trajectories, the incident angle of each new electron is sampled from this angular distribution.

4.3 Electron's step length

The electron's mean free path is the average distance the electron must travel through the solid to undergo an average of one event of a particular type. Mean free path's can be separately calculated for elastic scattering, inner shell ionization, plasmon scattering and so on. If several different scattering processes can occur, the total mean free path, λ_T, which considers all of the processes, can be calculated as:

$$\frac{1}{\lambda_T} = \sum_i \frac{1}{\lambda_i} \tag{4.1}$$

where λ_i is the mean free path of each scatter process. Scattering events fall in two categories: either elastic in which the trajectory direction is altered but the electron's energy remains the same or inelastic in which both the electron's trajectory and energy changes. Inelastic scattering is responsible for the energy transfer to the solid which subsequently results in the emission of secondary radiation, including secondary electrons, characteristic x-rays and Auger electrons, bremsstrahlung, x-rays and so on. Since only elastic scattering events are presumed to contribute to significant angular deviations, the step length between scattering events is determined from the mean free path for elastic scattering [28]:

$$S = -\lambda ln(R) \tag{4.2}$$

where λ is the electron's elastic mean free path and $R \in [0, 1]$. Equation 4.2 originates from the survival equation [32]:

$$N/N_0 = e^{-S/\lambda} \tag{4.3}$$

expressing the fraction of electrons N/N_0 left after it penetrated a distance S into the solid. This fraction can be represented by a random number $R \in [0, 1]$. The elastic mean free path for a compound is given by [19, 30]:

$$\lambda = \frac{1 \times 10^{-6}}{N_A} \frac{\frac{\mathbf{CA}}{\mathbf{F}\rho'}}{\mathbf{F}\sigma'} \ (m) \tag{4.4}$$

with $\mathbf{C}$ a row vector containing the atomic weight fraction of Zn, S and O. The column vector $\mathbf{A}$ contains the atomic weights (g/mol) of the three elements. The atomic fraction $\mathbf{F}$ is again

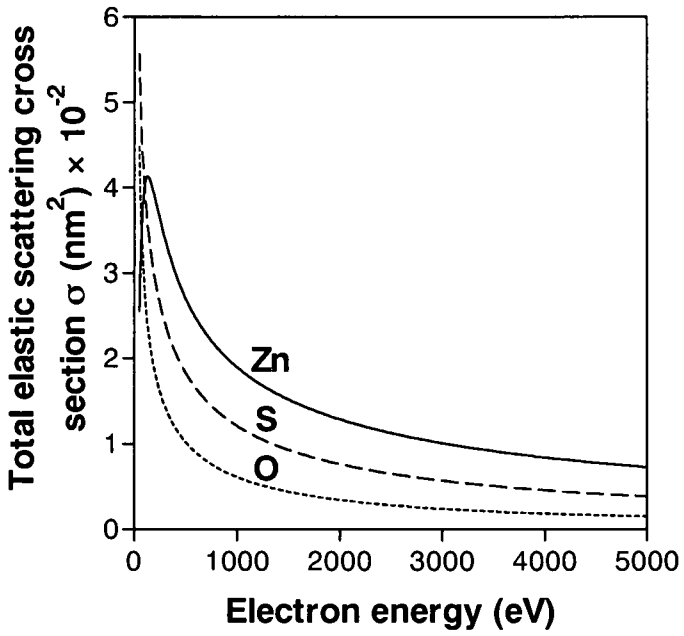

Figure 4.3: The total elastic scattering cross section σ as function of electron energy for Zn, S and O. The value for σ is obtained from a database using the Mott theory to describe the elastic scattering.

a row vector, while the density ρ' (g/cm^3) and the total elastic scattering cross section σ' (m^2) are column vectors and N_A Avogadro's number. The denominator $\mathbf{F}\sigma'$ refers to the total elastic scattering cross section for the compound [30]. In the expression by Hovington et al. [19], a mean density is used for the compound, but in Equation 4.4 this is modified to $\mathbf{F}\rho'$ to accommodate any changes in the stoichiometry of the solid. For a solid consisting of a single element, Equation 4.4 simplifies to that given by Newbury et al. [33] and Ding et al. [34].

In Figure 4.3 the value of σ for Zn, S and O as a function of electron energy is shown. The value for σ is taken from a database supplied by the National Institute of Standards and Technology (NIST) [35] which forms part of their standard reference data program. The database supplies the differential and total scattering cross section for elements with atomic numbers between 1 and 96 and for electron energies ranging from 50 eV to 10 keV. Refer to *Appendix B* for a complete description of the NIST database. For all the elements the total scattering cross section decreases with an increase in electron energy with Zn, physically the largest atom and therefore having the largest cross section. It is only at very low energies that the cross section

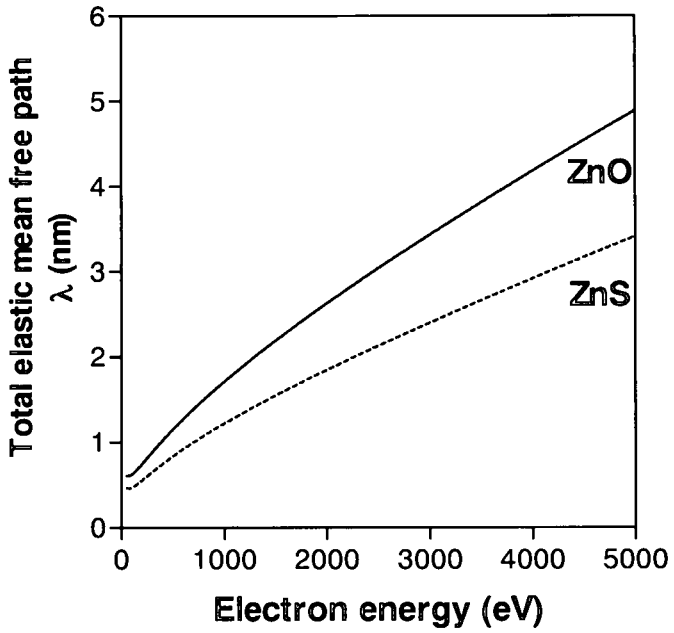

Figure 4.4: The total elastic mean free path as a function of the electron energy for ZnO and ZnS. In the diffusion interface, the total elastic mean free path is a linear combination of the individual mean free paths for the elements Zn, S and O based on the atomic concentration of each element and not shown here.

of O is larger than that of Zn. Using Equation 4.4 the elastic mean free path of an electron in a compound can be calculated. In Figure 4.3 the elastic mean free path for ZnO and ZnS is shown. In the diffusion interface the mean free path for a compound consisting of Zn, S and O can also be calculated using Equation 4.4. The varying concentration of these three elements will vary the elastic mean free path as function of depth in the diffusion interface.

4.4 The electron's energy loss

Although inelastic scattering is neglected as far as angular deviations and path length are concerned, energy loss due to inelastic scattering events is considered by means of the Bethe continuous energy loss approximation. The energy loss ΔE of the electron along it's step length is determined by:

$$\Delta E = \frac{dE}{dS} \times S \tag{4.5}$$

where S is the step length and dE/dS is the energy loss rate. The most widely used analytical expression for the energy loss factor has been that of Bethe (1930) and gives good results over a wide energy range. However at low electron energies (below 10 keV) certain events, like inner shell ionizations, are no longer possible and the Bethe expression does not compensate for this [36]. Writing the Bethe expression in a more generalized version, the total stopping power can be expressed as the sum of core ionizations, plasmon and conduction electron excitations [37] with the number of terms reducing with a decrease in electron energy. Joy and Luo [38] suggested a modification to the mean ionization potential which represents the average energy loss per interaction considering all possible energy loss processes [39]. The mean ionization potential, which represent the summation of these terms, should be modified to be energy dependant. They showed that the modified expression is in good agreement with other theoretical models of Tung [40] and Rao-Sahib Wittry [41]. The modified Bethe expression is given by:

$$\frac{dE}{dS} = -\frac{7.85 \times 10^{12}}{E}\frac{\rho Z}{A} ln(\frac{1.166E}{J^*}) \ \ (eV/m) \tag{4.6}$$

where E is the electron energy (eV), ρ the density (g/cm^3), Z the atomic number and A the atomic weight of a specific element with J^* the modification suggested by Joy and Luo [42]:

$$J^* = \frac{J}{1 + 0.85\frac{J}{E}} \tag{4.7}$$

where J is the mean ionization potential of the material:

$$J = 9.76Z + 58.8Z^{-0.19} \ \ (eV) \quad Z \geq 13 \tag{4.8}$$

or

$$J = 11.5Z \ \ (eV) \quad Z \leq 12 \tag{4.9}$$

In a compound, the modified Bethe expression becomes [19]:

$$\frac{dE}{dS} = \sum_{i=1}^{n} C_i(\frac{dE}{dS}_i) \ \ (eV/m) \tag{4.10}$$

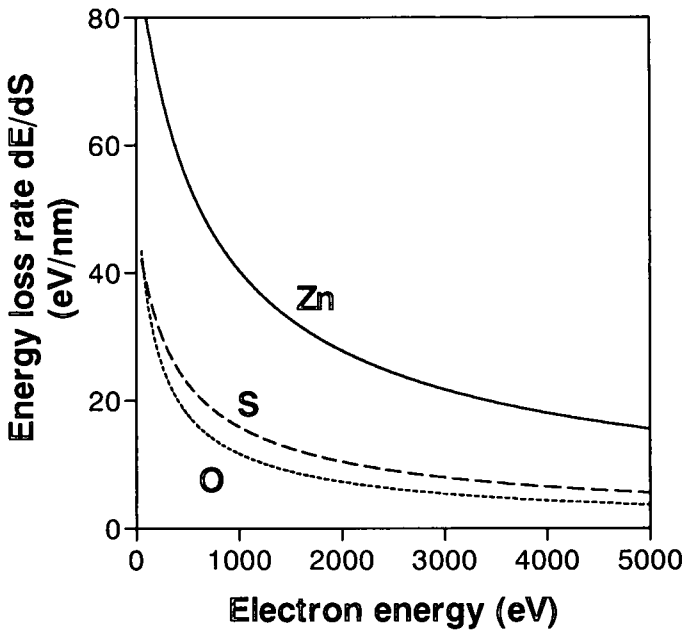

Figure 4.5: The rate of electron energy loss due to screening from Zn, S and O atoms according to Equation 4.6.

where n is the number of elements in the compound and C_i is the weight fraction of each element. To change the atomic fraction into weight fraction the following expression is used [43]:

$$C_i = \frac{F_i A_i}{\mathbf{FA}} \tag{4.11}$$

where C_i is the weight fraction and F_i is the atomic fraction of each element i. $\mathbf{F}$ and $\mathbf{A}$ is a row and column vector respectively containing the atomic fraction and weight fraction of Zn, S and O.

In Figure 4.4 the energy loss rate of electrons due to screening from Zn, S and O atoms are shown as function of the electron's energy. Since Zn is the larger atom, the screening effect is expected to be the most dramatic and be responsible for the greatest electron energy loss over the whole range of electron energy values. The energy loss associated with S and O atoms is again based upon the size of the atoms.

4.5 Atoms responsible for scattering

In a compound, the decision on which element's atom is responsible for scattering the electron is based upon the elemental contribution to the total elastic scattering cross section of the solid [30]. In the particular case of ZnO/ZnS, for any given number $R \in [0, 1]$, Zn atoms are responsible for the scattering when:

$$0 \leq R \leq \frac{F_{Zn}\sigma_{Zn}}{\mathbf{F}\sigma'} \tag{4.12}$$

or S atoms when:

$$\frac{F_{Zn}\sigma_{Zn}}{\mathbf{F}\sigma'} \leq R \leq \frac{F_{Zn}\sigma_{Zn} + F_S\sigma_S}{\mathbf{F}\sigma'} \tag{4.13}$$

or O atoms when:

$$\frac{F_{Zn}\sigma_{Zn} + F_S\sigma_S}{\mathbf{F}\sigma'} \leq R \leq 1 \tag{4.14}$$

where F_{Zn} and F_S are the atomic concentrations of Zn and S, while σ_{Zn} and σ_S are the total elastic scattering cross section of these two elements.

Depending upon the desired wavelength of light emitted during CL, ZnS powders are doped with specific trace elements. For example, to obtain blue light the phosphor powder is doped with Ag and Cl atoms and to obtain green light, the dopant atoms are Cu, Al and Au. Although these dopants are responsible for the light emission by forming recombination centers, their concentrations are minute and can be neglected for all practical reasons when simulating the electron trajectories.

By varying the concentration of the elements in the vector $\mathbf{F}$ according to an error function, it is possible to simulate the ZnO layer on top of the ZnS bulk with a diffusion layer between them as shown in the simulated depth profile in Figure 4.5. One solution of Fick's second law [44] which is a differential equation describing the dynamic diffusion of atoms is:

$$\frac{c_s - c_x}{c_s - c_0} = erf(\frac{x}{2\sqrt{Dt}}) \tag{4.15}$$

where c_s is a constant concentration of the diffusing atoms at the surface of the solid, c_0 is the initial uniform concentration of the diffusing atoms in the solid and c_x is the concentration

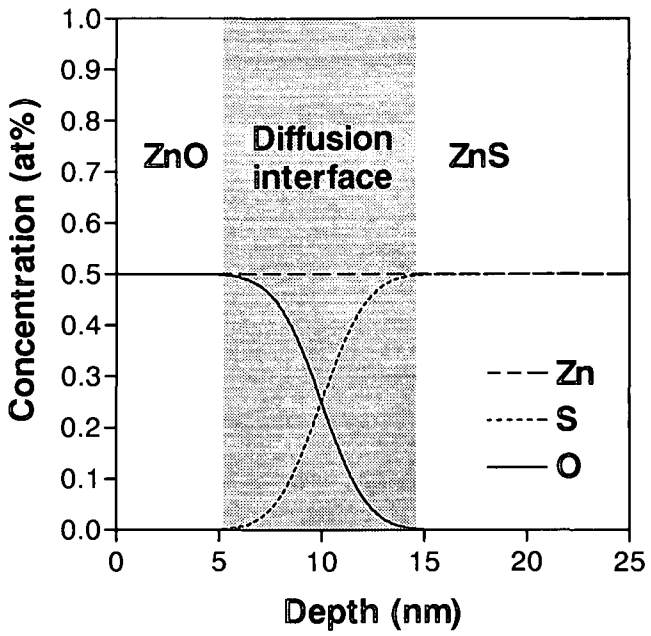

Figure 4.6: A simulated depth profile showing the atomic concentration as function of depth for a 10 nm thick ZnO layer on top of ZnS. The diffusion interface has a total width of 10 nm.

of the diffusing atom at position x below the surface after time t. This solution permits the calculation of the concentration of the diffusing atoms near the surface as a function of time and position beneath the surface. From this function a simulated depth profile can be obtained at a time t and is used to supply concentration values for $\mathbf{F}$. It is therefore possible to select the atom responsible for scattering based on it's concentration at a particular depth. For example, at a depth of 10 nm (See Figure 4.5) the concentration of Zn is 50% and that of S and O both 25%. Using these values, the scattering cross section as function of electron energy as well as Relations 4.12 to 4.14, a graphical representation of the scattering frequency of Zn, S and O atoms as function of electron energy is shown in Figure 4.5. In the Monte Carlo code the element responsible for the scattering event at a certain electron energy is chosen based on the value of a randomly distributed number $R \in [0, 1]$. For example, if an electron has an energy of 2000 eV and the random number has a value of 0.5 then the Zn atom is responsible for the scattering event. At the same energies, the S atom acts as a scattering center if R has a value of 0.75 and the O atom if R has a value of 0.9. Considering that the distribution of values for R is uniformly spread, Zn atoms will have the highest scattering frequency, with S atoms second and O atoms third. This is due not only to a higher concentration of Zn but

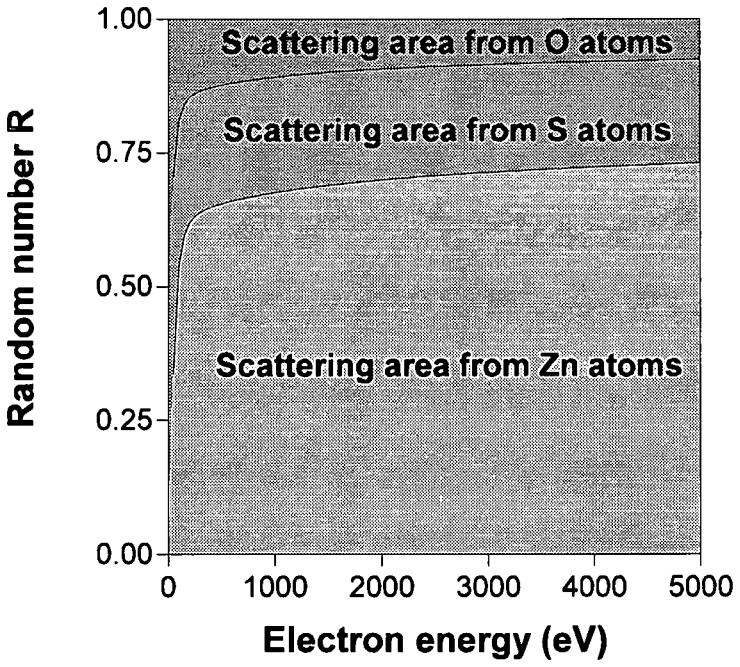

Figure 4.7: A graphical representation indicating the relationship between the random number R in Equations 4.12 to 4.14 and the scattering frequency from the different types of atoms as a function of the electron's energy. The concentration values for the atoms were obtained from the simulated concentration profile shown in Figure 4.5. The shaded areas correspond to the scattering frequency: the larger the area, the higher the frequency.

also due to a larger cross section, as seen in Figure 4.3. At very low electron energies (below about 300 eV) the participation of Zn atoms decrease, while that of S and O atoms increases in scattering frequency.

4.6 The scattering angles

Referring back to Figure 4.1, the two scattering angles that are responsible for changing the electron's trajectory are the azimuthal and polar angles, ϕ and θ respectively. The ϕ-angle is simply any angle between 0 and 360^o, while the θ-angle is a function of the differential elastic cross section of the atom responsible for the scattering event. Refer to *Appendix C* for a discussion on describing the electron trajectories in terms of these two angles and the electron's step length in Cartesian coordinates.

In the Monte Carlo simulation, the elastic cross section is used in two ways. As already seen, the *total* elastic cross section is used to describe the mean free path between scattering events, while the *differential* elastic cross section determines the polar scattering angle. A commonly used elastic scattering cross section is the screened Rutherford cross section which has a convenient analytical form and is straightforward to implement in a Monte Carlo calculation. However, the screened Rutherford cross section can only be applied to high energy electrons and solids with a low atomic number. An alternative to the screened Rutherford cross section is the partial wave expansion method of the Mott scattering cross section [45]. These values are also available from the NIST database [35].

In Figures 4.6 the polar scattering angles are shown for S and O as function of the electron energy and a number between 0 and 1 according to values obtained from the NIST database. For all three elements, Zn, S and O, the scattering angle is quite small for the largest part of the energy range, but increase considerably at very low electron energies.

4.7 Performing the trajectory simulation

In Figure 4.7 the Monte Carlo results are shown simulating the trajectories of 100 electrons each with an initial energy of 2 keV through a 10 nm thick ZnO layer into the ZnS bulk. The shaded region represents the diffusion interface with a total thickness of 10 nm. The concentration of S and O on top, in and below the diffusion interface varies according to the depth profile showed in Figure 4.5 with the thickness of the ZnO layer taken at the depth where O decreased to 50% of it's original concentration. The effect of using a distribution for the electron's incident angle is evident in the general direction of the initial electron trajectories in the solid. The final trajectory of several backscattered electrons that left the sample is also visible on the surface. However, to obtain a reliable backscattering coefficient, the number of electrons should be increased by at least three orders of magnitude.

Contrary to the method employed by Hovington et al. [19] no correction is made for the effect the change in region from ZnO to ZnS has on the electron's elastic mean free path and energy loss between scattering events. This is done for two reasons. Firstly, the transition between the two regions is not abrupt, but gradual due to the diffusion interface and, secondly, the electron's step length between scattering events is short and the diffusion interface thick enough to accommodate this change in concentration when computing the step length and energy loss.

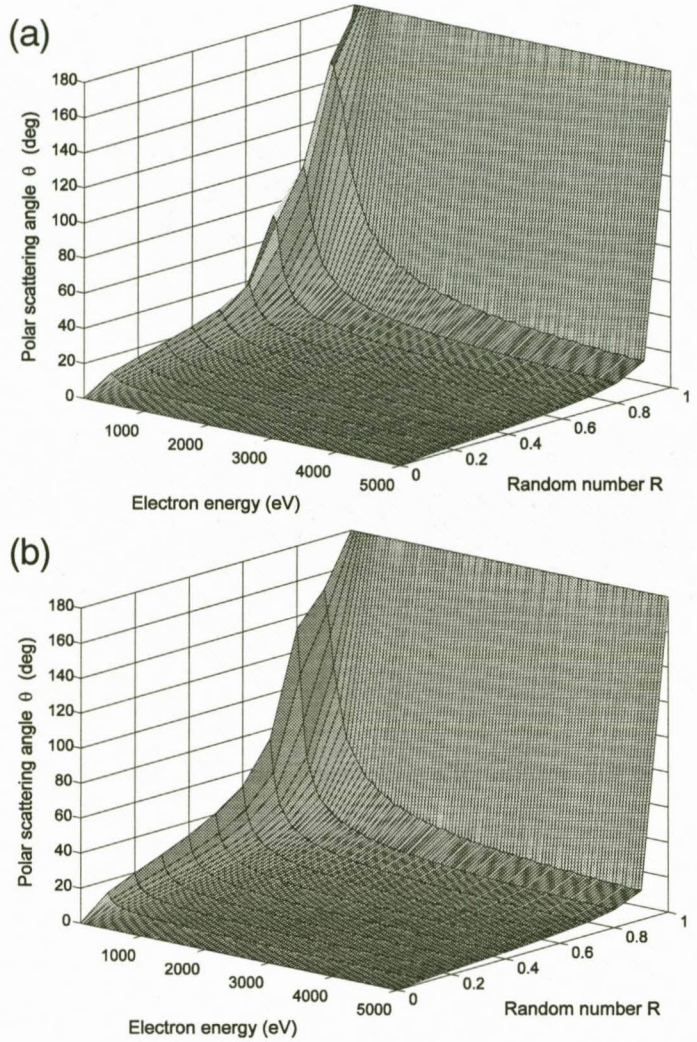

Figure 4.8: The polar scattering angles for (a) S atoms and (b) O atoms as function of the electron energy and a random number as provided by the NIST database [35].

U.O.V.S. BIBLIOTEEK

j 1553 95 44

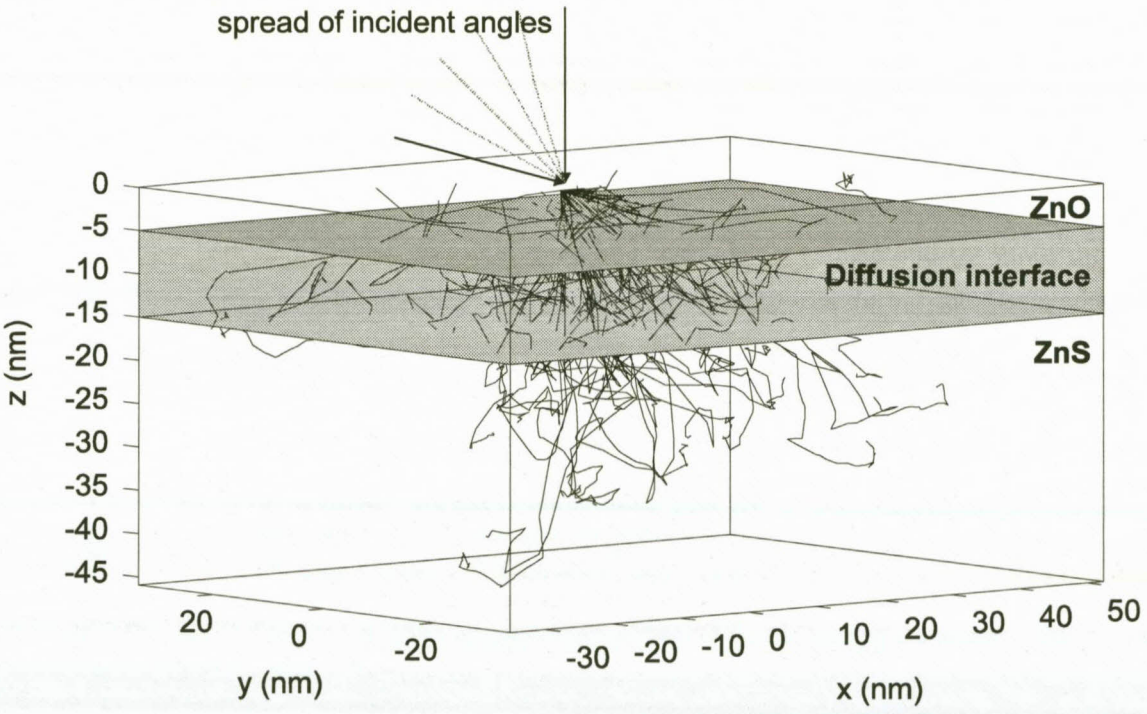

Figure 4.9: A Monte Carlo simulation of 100 electron trajectories with an initial 2 keV energy. The shaded region represent the diffusion interface between the ZnO layer and the ZnS bulk. The concentration of Zn, S and O follows that of the simulated depth profile shown in Figure 4.5 with the 50% mark of O at a depth of 10 nm.

4.8 Obtaining an energy loss profile

To determine an energy loss profile through the interaction volume [46], the volume is divided up into a number of thin horizontal layers and the energy loss in each layer calculated, giving the total energy loss as function of the depth of each layer [17]. In Figure 4.8 the simulated electron trajectories shown in Figure 4.7 were used to determine a very low resolution energy loss profile. Since the exact position of each scattering event and the electron's associated energy at that position is known, the energy loss rate $\Delta E_z/\Delta z$ between two subsequent scattering events at depths z_i and z_{i+1} can be determined:

$$\frac{\Delta E_z}{\Delta z} = \frac{E_i - E_{i+1}}{z_i - z_{i+1}} \tag{4.16}$$

Dividing the interaction volume into 0.1 nm thick layers, this energy loss is then spread through

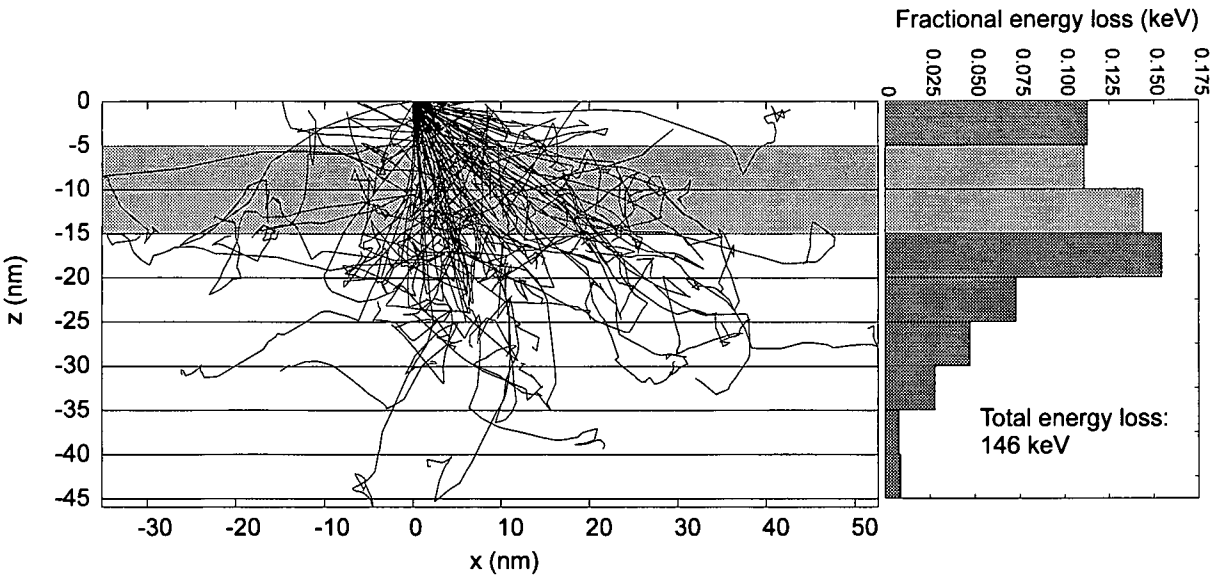

Figure 4.10: The energy loss profile on the right side of the electron trajectories shown in Figure 4.7 generated by dividing the interaction volume into horizontal layers and calculating the total energy loss in each layer. The shaded regions in the trajectory plot and corresponding energy loss profile indicates the diffusion interface region.

these layers between depths z_i and z_{i+1}. In Figure 4.8 each of these layers were 10 nm thick, leading to very rough approximation of the energy loss profile. The y-axis of the energy loss graph is expressed in the unitless *Fractional energy loss*. This term expresses the energy loss of electrons $\Delta E/\Delta z$ (Refer to Equation 4.16) in the solid as a fraction of the total input energy, which in this case was 200 keV (2 keV/electron $\times$ 100 electrons). The sum total of all the fractional energy losses in the layers is 0.73 (146 keV / 200 keV) which is less than unity, indicating that some still-energetic electrons were backscattered. This is confirmed by a backscattering coefficient of 0.3 indicating that about 30% of electrons left the sample. This value is obtained by counting the number of electrons that are scattered to such an extent during the simulation that they exit the sample again.

In Figure 4.8 the energy loss profile is shown for a diffused 10 nm thick ZnO layer on top of the ZnS bulk. The thickness value was chosen according to previous measurements by XPS depth profiles on degraded ZnS phosphor powders [15]. This profile was obtained by simulating 10^5 trajectories of 2 keV electrons and using Equation 4.16 to determine the energy loss. Figure 4.8

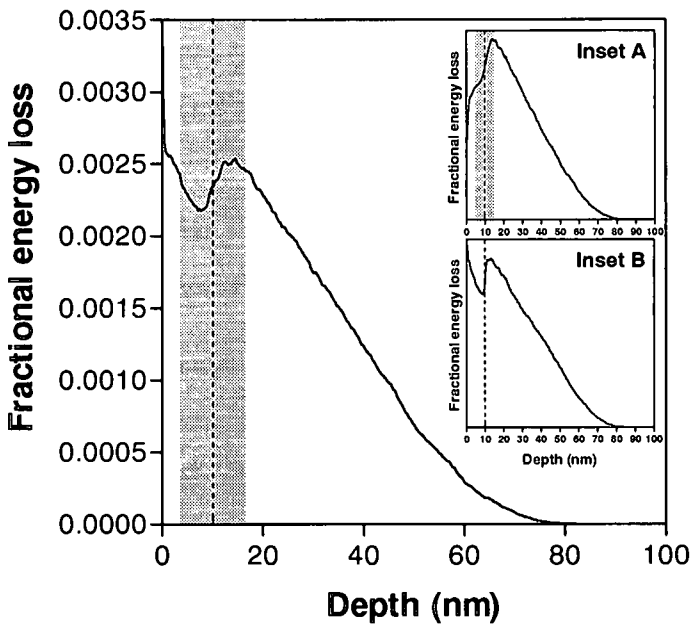

Figure 4.11: The fractional energy loss of 2 keV electrons as function of depth for a 10 nm thick ZnO layer on top of ZnS. The diffusion interface between ZnO and ZnS is 10 nm thick and indicated by the shaded area. In Inset A a similar energy loss profile is shown, but instead of using a distribution of incident angles (see text), an incident angle of 0 degrees was used. In Inset B an energy loss profile is shown without the diffusion interface, but with the angular distribution.

differs from the energy loss profiles shown by Toth and Phillips [17] for 4 to 20 keV electron beams in GaAs. In the profiles of Toth and Phillips the energy loss increases from zero at the surface to a maximum value at some depth below the surface before it then decreases to zero again. The energy loss profiles were calculated by dividing the solid into a number of horizontal layers, the same way as described in the previous paragraph. The simulation by Toth and Phillips was performed at a zero incident angle and therefore the initial electron trajectory is perpendicular to the layers. The energy loss during the first step length is spread over a large number of layers, reducing the energy loss in each layer.

The direction of the electron changes only after the first scattering event. The electron trajectory is not perpendicular to the surface after the first scattering event and the energy loss in the following step length is therefore spread over a smaller number of layers, increasing the energy loss in each layer. In the following scattering events, the change in direction is more dramatic, increasing the energy loss in each layer.

The observed maximum energy loss at a depth of around 13 nm should not be confused with abovementioned maximum energy loss seen in Figure 4.8. This maximum is due to the ZnO/ZnS interface and is attributed to the difference in electron energy loss associated with O and S atoms. In this profile the energy loss immediately starts to decrease from 0.0025 as a result of the distribution of incident angles used in the simulation. The initial electron trajectory is not perpendicular and therefore the energy loss during the first few step lengths is spread over a smaller number of layers, increasing the energy loss in these shallower layers. This masks the observed maximum seen in the energy loss profiles of Toth and Phillips. A simulation that was performed with the same parameters as above, expect that the incident angle was set to 0^o, is shown in Inset A in Figure 4.8. These results are in agreement with that of Toth and Phillips.

The diffusion interface, indicated by the shaded area in the graph, has a total width of 10 nm with the concentration of Zn, S and O in this area corresponding to the profile shown in Figure 4.5. The effect the absence of such a diffusion interface has on the energy loss profile is shown in inset B in Figure 4.8 with the profile changing much more abruptly in the ZnO/ZnS region. Since the concentration of the Zn atoms remains constant in both regions, the increase should be due to the transition from O atoms in the ZnO layer to S atoms in the ZnS bulk. Referring back to Figure 4.4, O has a lower rate of energy loss dE/dS than S and therefore less energy is deposited into the layers when electrons travel through ZnO than when it travels through ZnS. Adding a diffusion interface smooths out this transition from O to S atoms, resulting in a more gradual increase in the energy loss of the electrons in this region.

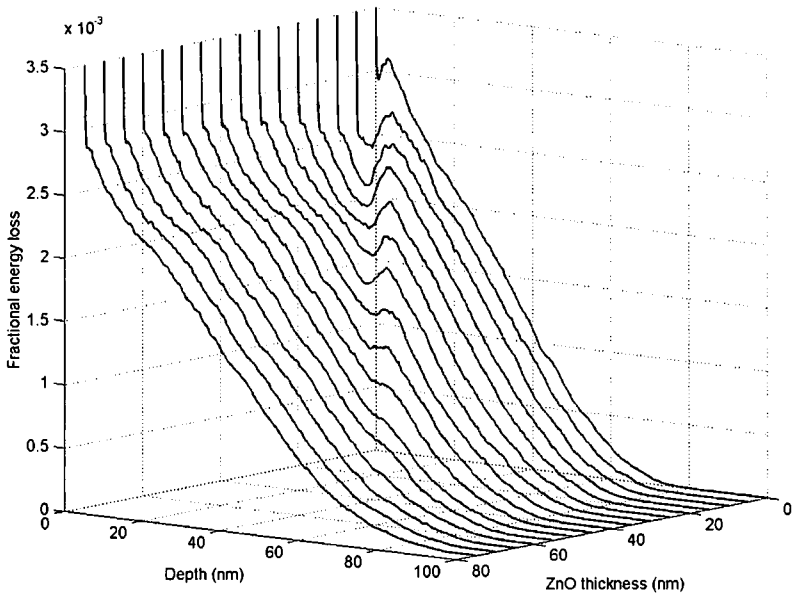

Figure 4.12: Simulated 2 keV energy loss profiles as function of the ZnO thickness. The diffusion interface was 10 nm thick.

In Figure 4.8 a collection of energy loss profiles is shown for increasing ZnO thicknesses. The interface width was kept constant at 10 nm. The effect of increasing the oxide thickness on the energy loss profile is evident from the movement of the transition region between ZnO and ZnS to higher values on the depth-scale. Although there is a slight increase in the electron range from the ZnS bulk to the ZnO layer, the area underneath each profile, which represents total energy loss, decreases with an increase in the ZnO thickness. In Figure 4.8 the backscattering coefficient and total energy loss as function of the ZnO thickness are compared. The correlation between these two parameters is clear from the trend displayed in the graph. As the thickness of this layer increases, the backscattering coefficient increases, therefore more still-energetic electrons leave the sample and less energy is deposited into the solid, confirming the decrease in energy loss with increase in ZnO thickness. Comparing the polar scattering angles of O and S atoms (Shown in Figure 4.6) at very low energies (below 1000 eV), O atoms have a larger polar scattering angle and therefore ZnO has a higher probability of contributing towards backscattered electrons. When the thickness of the ZnO layer exceeds the maximum penetration depth of the 2 keV electrons, the backscattering coefficient and total energy loss levels off.

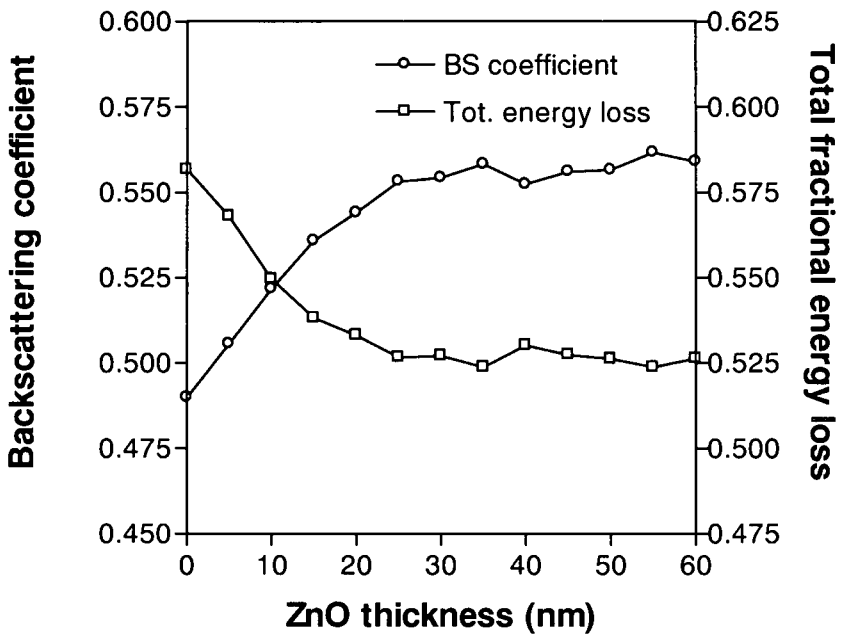

Figure 4.13: The backscattering coefficient and the total fractional energy loss as function of the ZnO thickness.

Chapter 5

Quantifying the CL intensity

5.1 Introduction

The energy that is lost by electrons in the phosphor powder generates electron-hole (e-h) pairs that can combine either radiatively or non-radiatively. In the case of radiative recombinations, photons are generated and propagate in all directions. Only a small fraction of these photons emerges from the surface, giving rise to measured CL intensity [47]. In this chapter an expression will be derived to calculate a normalized value for the CL intensity using the energy loss profiles simulated in the previous chapter. The CL intensity is then calculated as function of the oxide thickness for diffusion interfaces of variable thicknesses. These profiles are then compared to the measured oxide thickness after the CL degradation was experimentally performed.

5.2 An expression for the CL intensity

When an electron beam irradiates a semiconductor, e-h pairs are generated in the vicinity of the point of impact. The rate of e-h pair generation and the subsequent photon generation rate is determined by the energy loss rate of the incident electrons [48]. It can therefore be assumed that the CL intensity generated in the ZnS phosphor powder is proportional to the rate of the electron energy loss [16]. After the e-h pairs are created, other characteristic material properties determine the subsequent excess carrier distribution and radiative recombination rate.

5.2.1 The photon yield

The photon detection rate $N(\lambda, z)$ for photons of wavelength λ at a depth z is given by [49]:

$$N(\lambda, z) = Q(\lambda, z)[1 - A(\lambda, z)]D(\lambda) \quad [counts.s^{-1}] \tag{5.1}$$

with $Q(\lambda, z)$ a material dependent quantum or photon yield representing the number of photons of wavelength λ generated per second in the solid at depth z. The fraction of photons lost internally in the solid at depth z is given by $A(\lambda, z)$ and takes into account the effect of internal optical absorption, the total internal reflection loss and the Fresnel loss at the surface. The overall detection efficiency of the photometer or spectrometer is given by $D(\lambda)$.

The photon yield $Q(\lambda)$ is given by:

$$Q(\lambda, z) = G(z)\eta_i \tag{5.2}$$

where $G(z)$ is the e-h pair generation rate at depth z weighted by the internal radiative quantum efficiency η_i. For solids with energy gaps, η_i is the ratio of the band-edge radiative recombination rate to the total recombination rate. When radiative and non radiative processes compete in parallel, η_i can be expressed in terms of carrier lifetimes [50, 51].

The e-h generation rate G for semiconductors is given by [52]:

$$G = \frac{EI_b(1-\eta)}{qE_i} \quad [s^{-1}] \tag{5.3}$$

with E the electron beam energy, I_b the electron beam current, η the electron backscattering coefficient, q the electron charge and E_i the average energy required to create such an e-h pair.

Equation 5.3 can be expressed in terms of the energy loss of electrons in the solid. The electron beam current I_b is defined by the basic definition of charge per unit time where the charge is expressed as the product between the number of electrons per unit time and it's charge. In the previous chapter energy loss profiles which describe the energy loss as function of the interaction depth were simulated using the Monte Carlo method [53]. In the simulations a certain number of electrons were used to simulate an energy loss profile at a specific beam energy. If this number is n, the electron beam current per unit time is then given by:

$$I_b = nq/t \tag{5.4}$$

with q the electron charge. Substituting Equation 5.4 into Equation 5.3 yields:

$$G = \frac{En(1-\eta)}{E_i t} \tag{5.5}$$

The numerator in Equation 5.5 represents the total energy loss in the interaction volume. For the energy loss profile determined by the Monte Carlo simulation, the depth distribution of this total energy loss is known and therefore the e-h pair generation rate can be expressed as a function of the depth z:

$$G(z) = \frac{\Delta E(z)}{E_i t} \tag{5.6}$$

Due to the non-luminescent ZnO layer formed on top of the ZnS phosphor powder, only e-h pairs generated in ZnS will be able to combine radiatively and generate photons. Using the concept of a diffusion interface, which was developed in the previous chapter, the e-h pair generation rate in ZnS is given by:

$$G(z) = \frac{\Delta E(z) F_{ZnS}(z)}{E_i t} \tag{5.7}$$

with $F_{ZnS}(z)$ the atomic concentration of ZnS at a depth z. The exclusive energy loss in ZnS only can therefore be expressed as:

$$\Delta E_{ZnS}(z) = \Delta E(z) F_{ZnS}(z) \tag{5.8}$$

In Figure 5.2.1 an example is shown of an energy loss profile of 10^5 electrons, each with an initial energy of 2 keV. Using Equation 5.8 the energy loss profile in ZnS can be computed and is also shown in Figure 5.2.1. Note the gradual decrease of energy loss in the diffusion interface. Using the previous equation, Equation 5.7 then becomes:

$$G(z) = \frac{\Delta E_{ZnS}(z)}{E_i t} \tag{5.9}$$

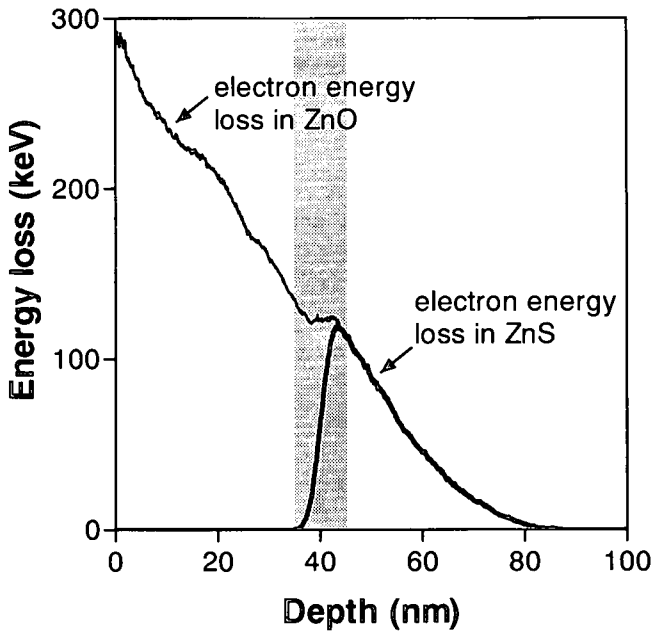

Figure 5.1: The electron energy loss as function of depth as computed with the Monte Carlo method for 10^5 electron trajectories each with an initial energy of 2 keV. The diffusion interface between the ZnO layer and the ZnS bulk is indicated by the shaded area and is 10 nm wide and the ZnO layer is 40 nm thick. The energy loss profile in ZnS is indicated by the thicker line.

5.2.2 The optical losses

The optical losses $A(\lambda, z)$ within the solid at depth z is described by [54]:

$$A(\lambda, z) \approx 1 - [(1 - R)(1 - cos(\theta_c))e^{-\alpha z}] \tag{5.10}$$

where $(1 - R)$ accounts for the normal reflection losses at the solid-vacuum interface, $(1 - cos(\theta_c))$ describes the total internal reflection at a certain critical angle θ_c determined by the material's refractive indices and $e^{-\alpha z}$ is the optical self-absorption. The α parameter is the absorption coefficient and z is the optical path length. For the ZnS phosphor this path length is the distance the photon must travel from it's point of generation in the ZnS bulk through the ZnO layer to the surface [22]. These two materials have different optical characteristics and absorb photons to different extents. To compensate for this a photon transmittance function $\alpha'(z)$ is defined:

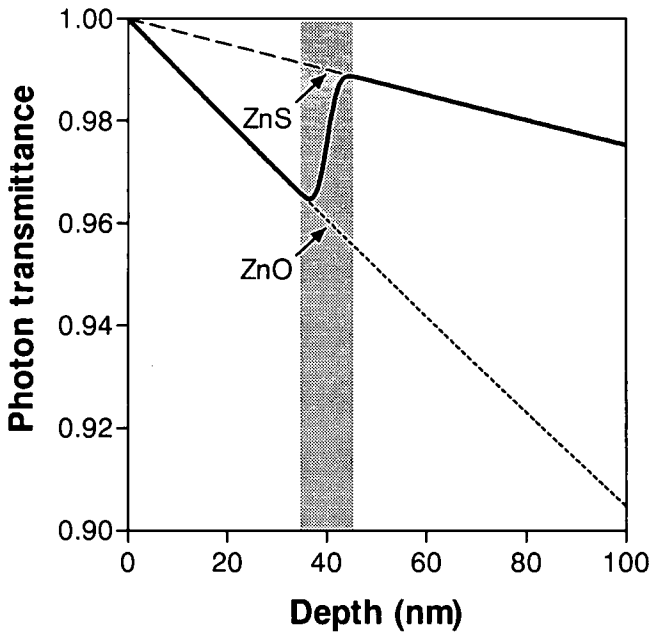

Figure 5.2: The photon transmittance as function of depth for ZnO and ZnS. Employing the concept of a diffusion interface, a composition of the two separate functions was obtained and is indicated by the thicker line.

$$\alpha'(z) = e^{-\alpha_{(ZnO)}z} F_{(ZnO)}(z) + e^{-\alpha_{(ZnS)}z} F_{(ZnS)}(z) \tag{5.11}$$

where the first term is the transmittance factor for ZnO adjusted with the atomic concentration of ZnO. The atomic concentration is obtained from a simulated depth profile, similar to the one shown in Figure 4.5. The second term is applicable to ZnS. In Figure 5.2.2 a plot of $\alpha'(z)$ as function of the depth is shown. This plot was constructed using dummy values for the absorption coefficients and serves only to illustrate the concept.

5.2.3 Quantification by normalization

Replacing $Q(\lambda, z)$ and $A(\lambda, z)$ in Equation 5.1 with the expressions in Equations 5.2 and 5.10 yields:

$$N(\lambda, z) = \left[\frac{\Delta E(z) F_{(ZnS)}(z)}{E_i t} \eta_i\right] \left[(1-R)(1-\cos\theta_c)\alpha'(z)\right] D(\lambda) \tag{5.12}$$

Some material properties like the average energy required to create an e-h pair and the radiative quantum efficiency, as well as some optical properties like the normal reflection losses at the solid-vacuum interface and the total internal reflection are independent of the energy loss in the solid. The time parameter referred to in Equation 5.4 also remains constant if the same amount of electrons are used during each Monte Carlo simulation. Furthermore, the detector efficiency $D(\lambda)$ also remains constant. All these parameters can be grouped into a single factor:

$$K = \frac{\eta_i}{E_i t}(1 - R)(1 - cos\theta_c)D \tag{5.13}$$

so that Equation 5.12 becomes:

$$N(\lambda, z) = \Delta E(z) F_{(ZnS)}(z) \alpha'(z) K \tag{5.14}$$

To obtain a value for the total cathodoluminescence generated in the volume, Equation 5.14 must be integrated along the entire pathlength of the interaction volume:

$$N_{total}(\lambda) = \int_{-\infty}^{0} N(\lambda, z) dz \tag{5.15}$$

Quantifying the CL intensity generated in a ZnS phosphor powder without any ZnO layer provides a reference value $(CL)_0$ to which subsequent values may be normalized. Calculating $CL/(CL)_0$ removes the constant K from Equation 5.14.

5.3 Absorption coefficients for ZnO and ZnS

To describe the absorption process of photons which are generated in the ZnS powder and travel through the ZnS bulk and ZnO layer, the absorption coefficients of these materials must be known for the function $\alpha'(z)$ given in Equation 5.11.

ZnO material is currently of great interest to many applications like window materials for solar cells, gas sensors and piezoelectric transducers with many research groups actively studying it's structural, electrical and optical properties [55, 56, 57, 58, 59, 60, 61, 62, 63]. The groups deposited the ZnO layer onto glass and quartz substrates using either pulsed laser deposition or radio frequency (r.f.) sputtering. The crystallinity of the material was determined using X-ray diffraction (XRD) and revealed a wurtzite structure. The optical properties of the material

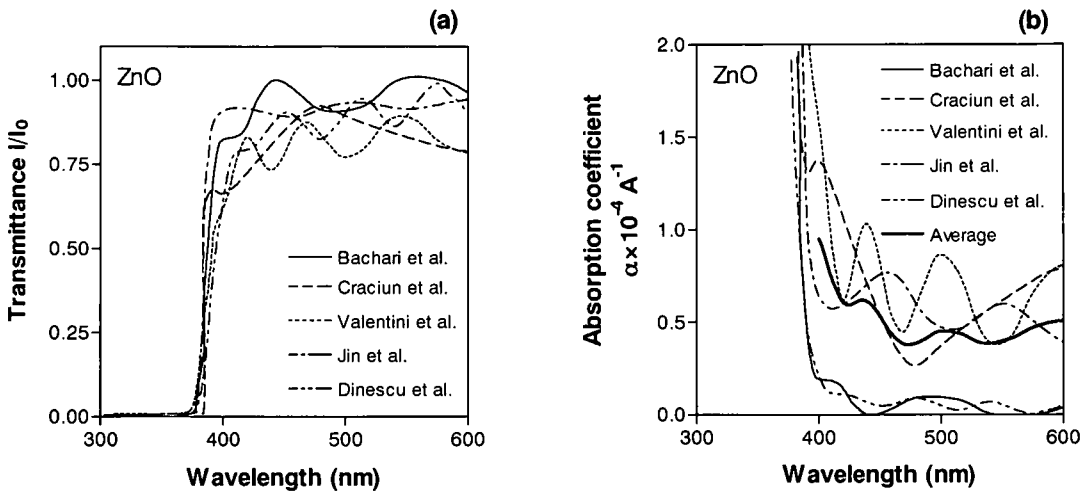

Figure 5.3: In (a) a selection of optical transmittance data measured for ZnO films of varying thicknesses prepared on mainly glass substrates by both pulsed laser deposition and r.f. sputtering techniques is shown. In (b) the absorption coefficient for ZnO is shown according to the optical transmittance data in (a) and transformed using Lambert's law of absorption.

was investigated by measuring the optical transmission through the ZnO films. A selection of transmittance data measured by the various groups are shown in Figure 5.3(a).

The relationship between the transmittance T, reflectance R and the absorption coefficient α is given by [64]:

$$T = \frac{(1-R)^2 e^{-\alpha t}}{1 - R^2 e^{-2\alpha t}} \tag{5.16}$$

with t the film's thickness. Ignoring the effects of reflection at the film interfaces, the absorption coefficient α as a first approximation is then given by:

$$\alpha = -ln(T)/t \tag{5.17}$$

the well known Lambert's law of absorption [65].

Using the values for the film thicknesses given in the corresponding references, Figure 5.3(b) was plotted showing the absorption coefficient for ZnO as function of wavelengths between 300 and 600 nm. The thicker line in Figure 5.3(b) represent an average absorption coefficient

function based on the five separate functions.

ZnS-films are used as anti-reflection coatings due to it's high absorption of wavelengths in the infrared region of the electromagnetic spectrum and high degree of transparency to light in the visible region of the spectrum [66]. This optical filter characteristics are confirmed by the results of Maruyama et al. [67] who showed that the absorption coefficient for crystalline ZnS rapidly decreases as the wavelength increases.

ZnS-based phosphors are available in different wavelength emitting variations. The ZnS:Cu,Al,Au powders, referred to as P22G, are doped with trace amounts of Cu, Al and Au and emit green light with a maximum peak intensity at 501 nm [8]. The ZnS:Ag,Cl powders, referred to as P22B, are doped with trace amounts of Ag and Cl emit blue light with a maximum peak intensity at 450 nm [68].

At these wavelengths ZnS has a absorption coefficient of about $3.3\times10^{-12}A^{-1}$ when the results of Maruyama et al. are extrapolated to longer wavelengths. Referring back to Figure 5.3(b), ZnO has an absorption coefficient of about $0.5\times10^{-4}A^{-1}$ for wavelengths between 450 and 500 nm. Since the difference in the wavelengths emitted by the P22G and P22B phosphors are small, the same absorption coefficients are applicable to both types of phosphor powders.

5.4 Comparing the energy loss profiles with other models

In Figure 5.4 a collection of energy loss profiles as function of the ZnO thickness is shown. These profiles were obtained using similar simulation parameters as those used to construct Figure 5.2.1 except for the width of the diffusion interface which was narrowed to 0.01 nm. This was done for comparison purposes with the CASINO code that do not accommodate a diffusion interface between dissimilar layer and bulk materials. Furthermore, where a predetermined distribution function is supposed to be used to describe the distribution of electron beam incident angles in a simulation [31], the angle was set to a normal incidence position, again for comparison purposes. The movement of the interface between the ZnO layer and the ZnS bulk can be seen starting from the profile at the back (no ZnO layer) to the foremost profile with the thickest ZnO layer. The effect of using the predetermined distribution function can also be seen when this plot is compared to the one shown in Figure 4.8 where such a distribution was used. To obtain the cumulative energy loss in ZnS for each of the energy loss profiles shown in Figure 5.4, Equation 5.8 can be integrated along the entire path length of the interaction volume:

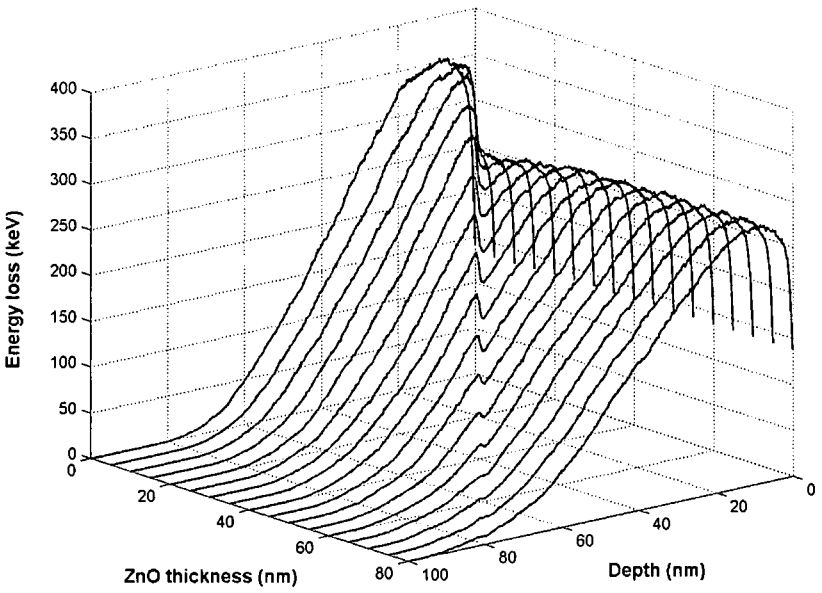

Figure 5.4: Calculated energy loss profiles for 2 keV electrons as function of the ZnO thickness. A total of 10^5 electrons were simulated in each profile. No diffusion interface was used in the simulation and the electron beam entered the sample at a normal incident angle.

$$\Delta E_{ZnS} = \int_{-\infty}^{0} \Delta E_{ZnS}(z) F_{ZnS}(z) dz \tag{5.18}$$

A plot of the normalized computed values as function of the ZnO thickness is shown in Figure 5.4.

The computed results can be compared to that generated by the CASINO code using the same parameters for the beam voltage and ZnO thickness used to compute the energy loss profiles displayed in Figure 5.4. Although no energy loss profiles are generated by the CASINO code, the fractional energy loss in the ZnS bulk is returned after the simulation if completed. Using this value a plot of the normalized values as function of the ZnO thickness is shown in Figure 5.4.

Comparing the two curves in Figure 5.4 the general trend is a rapid decrease in the energy loss as the thickness of the ZnO layer increases. From the relationship between the energy loss and CL intensity [16] this is in line with the observed decrease in CL intensity when the

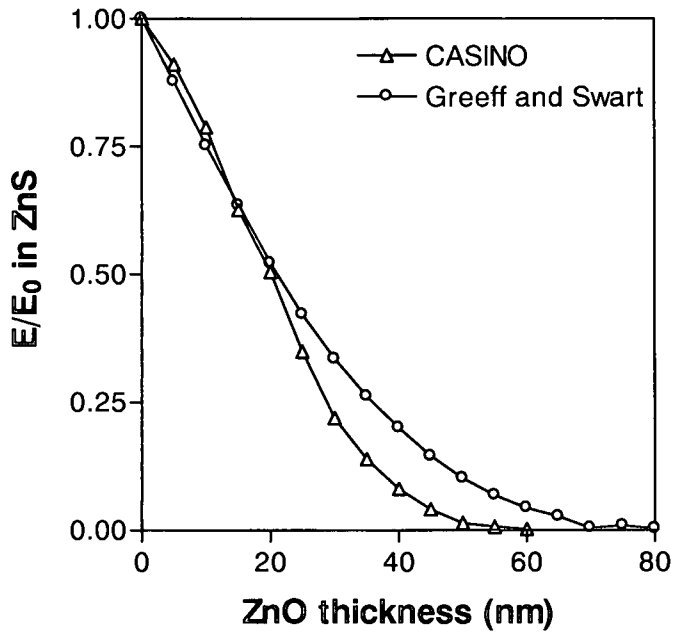

Figure 5.5: A comparison between two energy loss curves as function of the ZnO thickness using two different models. Both curves were generated for a 2 keV electron beam entering the sample at a normal incident angle.

ZnO thickness increases. The energy loss curve produced by the CASINO code decreases rapidly towards zero at around 60 nm. The curve predicted by Greeff and Swart reaches zero at an oxide thickness of about 80 nm which is 33% thicker. This difference can be attributed to different models used in the two codes. The CASINO code uses a model similar to that described by Greeff et al. [53] to describe the *energy loss* of the low energy electrons. However, a different model is used to describe the *polar scattering angles* of the electron trajectories after each scattering event. In the code by Greeff and Swart, a database [35] based on the Mott cross sections is used to calculate the elastic scattering angles and total cross sections. These parameters influence both the direction of the electron trajectories and energy loss in the solid. In the CASINO code these parameters are calculated using tabulated Mott cross sections.

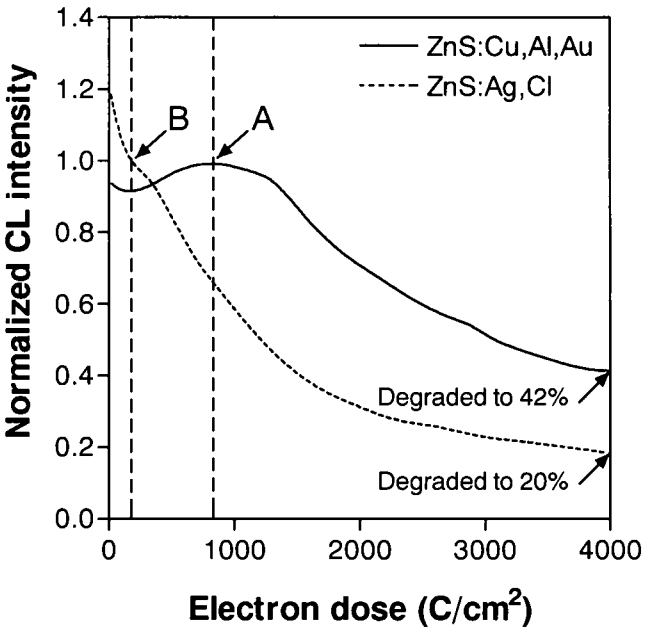

Figure 5.6: The normalized CL intensity measured as function of the electron dose during degradation of the ZnS:Cu,Al,Au and ZnS:Ag,Cl phosphor powder at a 2 keV beam energy [15].

5.5 Experimental measurement of the oxide thickness

Experimental measurements of the oxide thickness after degrading the phosphor powder by electron beam irradiation have been made by Swart et al. [8, 15]. The CL degradation profiles for ZnS:Cu,Al,Au and ZnS:Ag,Cl is shown in Figure 5.4. Both profiles were normalized to the relative CL intensity measured after the carbon on the phosphor powder was removed by the electron beam. For the ZnS:Cu,Al,Au phosphor the carbon was completely removed only after an electron dose of 800 C/cm^2. The normalization point is indicated by A in Figure 5.4). In the case of the ZnS:Ag,Cl phosphor powder the carbon was removed more rapidly and the profile is normalized to the CL intensity indicated by B in Figure 5.4.

In the first set of measurements [8] the ZnS:Cu,Al,Au phosphor powder was subjected to electron bombardment at 2 keV at an oxygen pressure of 1×10^{-6} Torr in a UHV chamber with a PHI Model 549 system while recording the CL data with a spectrometer. After the phosphor was degraded to 60% of the original CL intensity, corresponding to an electron dose of 38 C/cm^2, depth profiles were obtained by Ar ion sputtering and AES measurements. The

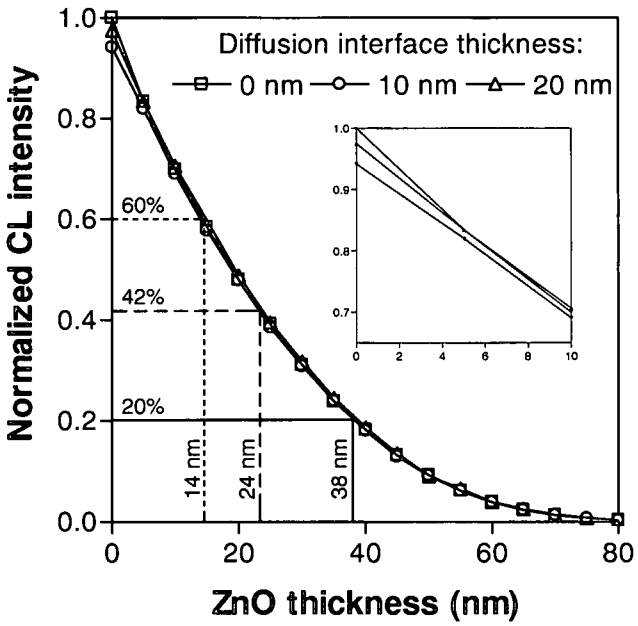

Figure 5.7: The normalized CL intensity as function of the ZnO thickness calculated with and without a diffusion interface between the ZnO layer and the ZnS bulk. The curves for the 10 and 20 nm wide diffusion interface were normalized with respect to the CL intensity for the oxide free ZnS with no diffusion interface. In the inset the CL intensities for the first 10 nm are shown enlarged.

sputtering rate was calibrated against a ZnO thin film of known thickness deposited onto a clear float glass substrate. The thickness of the oxide layer was measured as 3 nm. In the second set of measurements [15] the ZnS:Cu,Al,Au and ZnS:Ag,Cl phosphor powders were also subjected to electron bombardment at 2 keV and at an oxygen pressure of 5×10^{-7} Torr. The ZnS:Cu,Al,Au phosphor was degraded to 42% of it's original CL intensity and the ZnS:Ag,Cl phosphor to 20%, both corresponding to an electron dose of 4000 C/cm^2. Depth profiles were obtained in a PHI Quantum 2000 Scanning ESCA Microprobe system with Ar ion sputtering and XPS measurements. The sputtering was also calibrated against a ZnO thin film of standard thickness. The thickness of the oxide layer on the ZnS:Cu,Al,Au phosphor was measured as 11 nm and on the ZnS:Ag,Cl phosphor as 2.5 nm.

Phosphor type	*CL%*	*Measured (nm)*	*Simulation A (nm)*	*Simulation B (nm)*
ZnS:Cu,Al,Au	60	3	13	3
ZnS:Cu,Al,Au	42	11	22	12
ZnS:Ag,Cl	20	2.5	37	26

Table 5.1: A comparison between the experimentally measured oxide thicknesses on the phosphor powders and values predicted by the two simulations, Simulation A assumes a luminescent diffusion interface while Simulation B does not make the assumption.

5.6 Calculation of the CL intensity

In Figure 5.5 the normalized CL intensity as function of the ZnO thickness was calculated for different thickness diffusion interfaces between ZnO and ZnS. The curves were calculated using Equation 5.15 and the width of the interface was chosen as 10 and 20 nm. These values were chosen according to the previously measured XPS depth profiles [15].

The electron energy loss profiles were calculated at the same beam energy of 2 keV at which the phosphor powders were degraded. The predetermined distribution function was used to describe the distribution of electron beam incident angles over the surface of the phosphor powder [31]. Due to the small difference in absorption coefficients for light emitted by the phosphor powders, ZnS:Cu,Al,Au and ZnS:Ag,Cl, these simulated curves are applicable to both types of phosphors. The calculations for the diffusion interfaces were normalized with respect to the calculated CL intensity with no ZnO layer or diffusion interface present.

All three curves are identical, except for the first 5 nm oxide thickness where the two curves compensating for the diffusion interface have a lower intensity value. This difference is however very small and is shown enlarged in the inset in Figure 5.5. The first CL value of each curve regarding diffusion interfaces indicates the effect that any non-luminescent material has on the CL intensity in the absence of the oxide layer. In this simulation the decrease is the result of non-luminescent ZnO already present in the surface region prior to oxide growth. As the thickness of the non-luminescent surface region increases from 5 to 10 nm, the CL intensity also decreases accordingly because the largest part of electron energy loss takes place in the near-surface region. However, when the oxide layer starts to grow in thickness, the curves quickly fall together despite the difference in interface width since the majority of the energy loss now takes place within the ZnO layer. This indicates that any further decrease in the CL intensity is primarily due to oxide growth.

According to Figure 5.5 a decrease to 60% of the initial CL intensity corresponds to a 13 nm thick oxide layer while a decrease to 42% corresponds to an oxide layer 22 nm thick. A decrease to 80% of the initial CL intensity corresponds to a 37 nm thick oxide layer. In Table 5.6 these values, under the column *Simulation A*, are compared with the experimentally measured oxide thicknesses for the ZnS:Cu,Al,Au and ZnS:Ag,Cl phosphors. The experimental values are considerably less than the simulated values.

5.6.1 Non-luminescent diffusion interfaces

Up to now it was assumed that the ZnS in the diffusion interface was also luminescent. In fact, the formation of the interface itself may lead to the dissociation of all or some of the ZnS and ZnO to their respective atomic species due to the diffusion process. This will result in the interface being totally or partially non-luminescent. To test the influence of a totally non-luminescent layer on the CL curves shown in the Figure 5.5, the intensity calculations were repeated and the e-h pair generation in the diffusion interface disregarded. The results are shown in Figure 5.6.1. The curves for the 10 and 20 nm thick diffusion interface were normalized to the value of the CL intensity measured in the absence of an oxide layer or diffusion interface. This was done to accommodate for the initial stages of oxidation during nucleation and island formation. For example, in the absence of the oxide layer, the 20 nm diffusion interface should be interpreted as representative of the initial stages of oxidation with an incomplete oxygen coverage. As nucleation and island formation near completion and the oxide layer starts to grow uniformly as a thin film, diffusion processes results in the formation of a physical diffusion interface. CL intensities as shown in Figure 5.6.1 at a 0 nm ZnO thickness are therefore not a correct presentation of the initial diffusion interface width due to the uncertainty of the initial oxide growth process. As the ZnO layer continues to grow, the effect of the diffusion interface becomes clear.

The initial CL values are considerably less than those in Figure 5.5, because the non-luminescent material, in this case ZnO, prior to oxidation is thicker. As the width of the interface increases, the CL intensity decreases considerably more. Using the same degradation values as in Figure 5.5, the corresponding oxide thicknesses were predicted for the 20 nm wide diffusion interface. These values are listed in Table 5.6 under the column *Simulation B*. The values for the ZnS:Cu,Al,Au phosphor powder compare extremely well to the experimentally measured values, whilst the oxide layer on the ZnS:Ag,Cl phosphor powder is still much thinner than predicted.

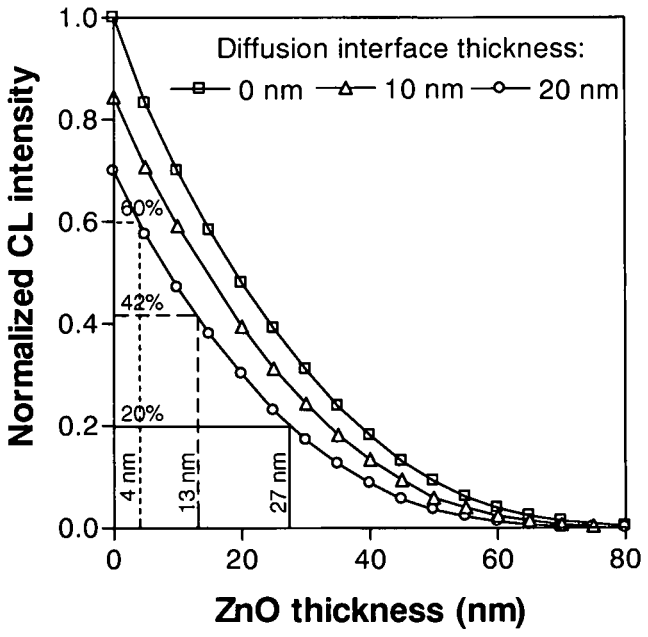

Figure 5.8: The same curves shown in Figure 5.5, but the CL intensity was calculated by disregarding the e-h generation rate in the diffusion interface. The curves were normalized in the same way as those in Figure 5.5.

5.6.2 Surface charging of the phosphor powder

During the experimental degradation of the phosphor powders, Oosthuizen et al. [9] measured a small shift of about 1 eV to higher energies for the Auger peaks of S during the initial stages of electron beam irradiation of the ZnS:Cu,Al,Au phosphor powder, shifting back to their normal positions after prolonged irradiation. More importantly, Swart et al. [15] measured a large Auger peak shift of about 46 eV to higher energies during electron beam irradiation of the ZnS:Ag,Cl phosphor powder. When an energetic electron beam irradiates a sample, secondary electrons are emitted form the sample's surface. The secondary yield (the ratio of secondary electrons emitted per incident electron) might be larger of smaller than 1. For dielectric targets, this ratio is smaller than 1 indicating a charge accumulation on the surface because it cannot be conducted away.

The presence of a surface charge relates to the CL intensity in two ways. Firstly, due to band bending the charge increases the probability that the generated e-h pair would be swept apart before radiative recombination can occur and therefore decrease the CL intensity. Secondly, assuming that ionized oxygen (O^-) is the rate determining factor for oxide growth, the presence

of a space charge would slow oxide growth because the negatively charged surface will repel the ionized oxygen. The fact that the oxide layer on the ZnS:Ag,Cl phosphor is more than four times thinner than the oxide layer on the ZnS:Cu,Al,Au phosphor after receiving the same electron dose correlates with the large charge measured on the surface of the ZnS:Ag,Cl phosphor. Even if the oxide layer is thinner in this case and the phosphor therefore should have a higher CL intensity, the overriding effect is still the surface charge build-up and reduced probability of e-h pairs recombining radiatively.

It was also shown by Swart et al. [8] that if the electron beam was turned off for a while during the degradation process of ZnS:Ag,Cl the measured CL intensity increased by 20% the moment the beam was turned on again. However, within seconds the CL decreased again to the same intensity before the beam was turned off. This can be explained in the following way. When the beam was turned off, the surface charge was conducted away from the target area, allowing e-h pairs to combine normally as soon as the irradiation was resumed and increased the CL intensity. However, the surface is quickly charged again and reduces the CL intensity accordingly. These results confirm that the decrease in CL is also partially the result of surface charging.

Therefore, in the case of the ZnS:Cu,Al,Au phosphor powder the decrease in CL intensity is singularly the result of the non-luminescent oxide growth around the powder and the formation of a non-luminescent diffusion interface with a lot of defects as predicted by Swart et al. [8] between the oxide and the powder itself. For the ZnS:Ag,Cl powder the degradation in CL intensity is due not only to the oxide growth and diffusion interface but also due to the trapping of charge over the range of the primary electrons during electron irradiation of the phosphor powder.

Chapter 6

Summary and general conclusions

During the electron beam irradiation of the phosphor powders, the intensity of the generated CL degrades as a result of the formation of a non-luminescent ZnO layer around the ZnS particles. The formation of this oxide layer is the result of surface chemical reactions between the ZnS phosphor and water vapor with the reaction stimulated by the electron beam. As the thickness of the oxide layer increases, the energy losses in the ZnS decrease. Since there is a direct relationship between the CL intensity and the energy loss in ZnS, growth of the oxide layer therefore decreases the CL intensity. The phosphor powder consists of both flat and spherical particles and due to their morphology oxide growth leads to varying effective ZnO thicknesses that detrimentally influence the CL generation to various extents.

The Monte Carlo method was used to simulate the interaction of the electron beam with the surface of the phosphor powder. A Gaussian distribution function was used to simulate the spread of the beam and the incident angle with the particle surface was calculated for each electron path. Simulating a sufficient number of electron paths, an angular distribution was determined. This histogram indicated the spread of incident angles as a function of the incident angle itself.

For the spherical particles, the results from the simulation indicated that the beam profile, neither in shape nor diameter, does not influence the angular distribution as long as the FWHM beam diameter is larger than the size of the spherical particle it irradiates. As the beam diameter is increased the angular distribution converges, making it possible to apply this common distribution to any diameter electron beam where the basic requirement concerning the FWHM beam diameter has been met. Since the flat particles are randomly orientated in the powder between 0 and 90°, there is a uniform angular distribution which is independent

upon the incident angle of the electron beam.

The angular distributions of the flat and spherical particles were combined and a function was fitted to these results. This function was used as a probability density function in determining the electron beam incident angle during the Monte Carlo simulations of the electron trajectories in the solid.

To accurately simulate the electron energy loss profiles for the phosphors, the concept of a diffusion interface between the ZnO layer and ZnS bulk material was developed. This was done by varying the concentration of S and O atoms in the interface during the Monte Carlo simulation of the electron trajectories. Modeling the interface in such a way provides a better theoretical description of the electron trajectories and energy loss in the interface region, since a sharp interface between the two layers very seldom exists.

From the simulated trajectory data for the electrons and the corresponding energy losses, energy loss profiles were calculated that indicated the cumulative energy loss of all the electrons as a function of the interaction volume's depth as well as the thickness of the ZnO layer. The energy loss profiles showed that the transition region between the ZnO layer and the ZnS bulk corresponds to a sharp increase in energy loss due to the higher rate of electron energy loss in ZnS. Furthermore, in the presence of a diffusion interface this increase in energy loss is spread over the entire width of the interface. In it's absence, the sudden increase in electron energy loss from ZnO to ZnS is unrealistically rapid. As the thickness of the ZnO layer increases, the energy loss in ZnO increases with an overall decrease in the total energy loss due to the increased backscattering coefficient associated with the ZnO material.

The energy loss profile was also considerably influenced by the incident angle of the electron beam. When the energy loss was simulated using the angular distribution, a large amount of energy loss occured in the extreme surface layers. In contrast, a normal incident angle resulted in an energy loss profile with a maximum energy loss deeper into the surface layers. This indicated that though the CL degradation is primarily due to the growth of the non-luminescent ZnO layer, the morphology of the phosphor powder also effects the CL intensity. These results suggests that a thin film of luminescent phosphor, instead of a powder, will be more effective at producing light in the presence of a ZnO layer since the energy loss profile is not as sensitive to the luminescence characteristics of the upper surface layers.

An expression was derived to quantify the CL generated in ZnS phosphor powders using the electron energy loss profiles. This expression employs a photon transmittance function, based on the simulated ZnO/ZnS concentration profile, to compensate for the absorption of photons

moving through the ZnS and ZnO material. Other quantum mechanical and optical parameters of the photon generation, transport and detection are eliminated by normalizing the results with respect to a calculation performed for a ZnS material without an oxide layer and which is penetrated by an electron beam at a normal incident angle.

The electron energy loss profiles were used to construct a curve describing the energy loss in the ZnS as function of the ZnO thickness for a specific beam energy. This curve was compared to the results of another Monte Carlo simulation on the electron energy loss in ZnO/ZnS material. According to both models the energy loss decreases rapidly as the thickness of the ZnO layer increases. However, the authors' calculated curve indicated that electrons penetrate about 33% deeper into the ZnO/ZnS material than indicated by the other model.

Using the energy loss profiles and the CL quantification expression, curves relating the normalized CL intensity to the ZnO thickness was calculated, again for a specific beam energy. In calculating the CL intensity it was assumed that the ZnS material within the boundary of the diffusion interface was non-luminescent. For a diffusion interface of a certain width, the CL intensity decreases rapidly as the thickness of the ZnO layer increases. This correlates with the fact that the thickness of the oxide layer is proportional to the energy loss in the ZnS. As the thickness of the diffusion interface increases, the CL intensity decreases more rapidly. This again correlates with abovementioned fact because the diffusion interface, similar to the oxide layer, is also a non-luminescent layer.

For the ZnS:Cu,Al,Au phosphor powder the predicted oxide thickness compared extremely well with previous experimental measurements if it was assumed that the interface between the ZnO layer and ZnS bulk was 20 nm wide. However, using the same simulation parameters the experimentally measured oxide thickness on the ZnS:Ag,Cl phosphor powder was much thinner than the predicted value. This difference between the experimental and predicted value can be attributed to the build-up of charge on the surface of the ZnS:Ag,Cl phosphor powder which influences the e-h recombination and rate of oxide growth.

In conclusion, the quantification model which was developed in this study gives a good description of the degradation in the CL intensity, assuming that only the growth of the ZnO layer contributes towards the CL decrease, as was the case for the ZnS:Cu,Al,Au phosphor. However, this model fails to describe the degradation in CL for the ZnS:Ag,Cl phosphor powders. This supports the evidence that for this particular type of phosphor ZnO growth is not solely responsible for the CL degradation. The decrease in CL is rather due to a combination of two factors: ZnO growth and surface charging.

Future work must focus on verifying the CL quantification model by expanding the number of experimentally measured ZnO thicknesses currently available after the CL was degraded to different extents. In this study only two thickness measurements were available for the ZnS:Cu,Al,Au phosphor powder while one measurement was available for the ZnS:Ag,Cl phosphor. Additional thickness measurements on the ZnS:Cu,Al,Au phosphor will provide more experimental points on the theoretical CL curve, while measurements on the ZnS:Ag,Cl phosphor will allow for corrections to be made to the current quantification model.

The presence of a surface charge influences the e-h recombination rate and increases in magnitude as the irradiation time increases. In essence the Monte Carlo method is a time independent process, but a time step can be attributed to the simulation in terms of beam current and the number of electron trajectories simulated. If the surface charge collection is known as a function of time, it should be possible to make the necessary correction to the quantification model.

Since the CL degradation profiles were experimentally measured at 2 keV, all the simulations in this study were performed at the same beam energy. To verify the quantification model further, the experimental ZnO thickness measurements should also be performed for phosphor powders degraded at beam energies different from 2 keV. At high beam energies the electrons have a deeper penetration depth and therefore the CL should be influenced less than for lower energy electrons. This trend is accommodated for by the quantification model, but the question is to which extent.

In obtaining the thickness measurements of the oxide layer, the CL degradation profiles as function of the irradiation time or electron dose are also usually available. Using these curves, the oxide thickness after the CL was degraded to a certain extent can be related to a degradation time. This will make it possible to express the CL quantification model in a time scale and compare it directly to the experimentally measured degradation profiles.

The impact of this study on current FED technology is concentrated in the research areas of improving the lifetime of phosphor powders used at low energies and also the setup and structure of the field emitter array and the phosphor screen. Using the quantification model, the influence of the non-luminescent oxide layer around the phosphor powder on the CL intensity can be predicted without performing the degradation experimentally. CL degradation may therefore by minimized using different beam energies or phosphor particle shapes. Also, controlling the amount of species responsible for the oxide formation, the influence of this on the thickness of the oxide layer and eventually the CL intensity may be tested. In another area the quantification model may be applied to improve the setup and structure of the field emitter

array as well as the phosphor screen. The influence of the diameter and shape of the beam on the CL intensity was shown in this study. The CL intensity may be maximized by controlling the tip's shape, and therefore the electron beam's shape, as well as the voltage applied to the focusing grid between the field emitter array and the phosphor screen. Concerning the phosphor screen itself, the difference in energy loss and subsequent CL intensity between a flat thin film of ZnS and the ordinary powder was already discussed earlier.

Appendix A

The Monte Carlo method

A.1 Introduction

The Monte Carlo method provides approximate solutions to a variety of mathematical problems by performing statistical sampling experiments on a computer. It employs a random number generator to sample a probability density function and predict the possible outcome of a certain event, described by this density function.

The method was named by the physicist Enrico Fermi after the city in the Monaco principality, because of it's association with the roulette wheels in the casinos. Mathematically seen, the roulette wheel is a perfect random number generator as can be constructed by mechanical means. The name and the systematic development of Monte Carlo methods dates from about 1944.

A.2 Illustration of the Monte Carlo method

A simple example to illustrate the use of the Monte Carlo method is the approximation of π. In Figure A.2 a unit circle is shown lying within a square with sides of length 2. If a random point (x, y), with $x \in [0, 1]$ and $y \in [0, 1]$ is chosen, the probability that this random point lies inside the upper right quarter of the unit circle (indicated by the shaded area) is given by the proportion between the area of the unit circle and the upper right square:

$$P(x^2 + y^2 < 1) = \frac{A_{circle}}{A_{square}} = \frac{\pi/4}{2^2/4} = \pi/4 \tag{A.1}$$

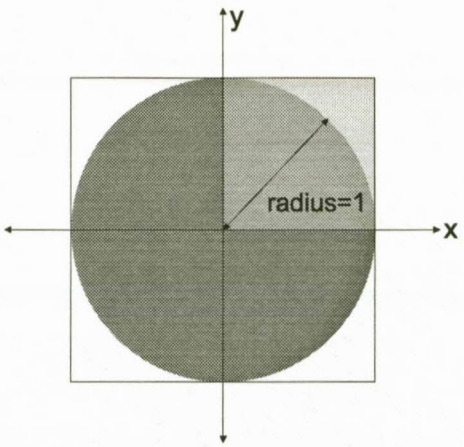

Figure A.1: Using the Monte Carlo method to approximate the value for π. The unit circle lies within a square with sides of length 2. The approximation uses the ratio of random points that lie inside the quarter circle to the total number of randomly chosen points.

If n random points are chosen and m of those points lie inside the unit circle, the probability that any random point lies inside the circle is given by:

$$P(x^2 + y^2 < 1) = m/n \tag{A.2}$$

and therefore the value of π can be approximated by the following expression:

$$\pi = \frac{4m}{n} \tag{A.3}$$

In Figure A.2 a graph is shown giving the approximation for the value of π using a different number of random points each time. The value for π was sampled 5 different times for each number of random points. When a small number of points is used, the approximation vary greatly. However, as the number of random points increases, the values vary less and the accuracy of the approximation increases. When 10^6 random points is used the value for π is approximated as 3.142 which is the mean of 5 samples.

Increasing the number of samples, increases the accuracy of the simulation, but also increases the computational time. This increase is linear with the number of samples. There is therefore a trade-off between the accuracy of the approximation and the computational time.

The same applies to the application of the Monte Carlo technique to simulating the electron

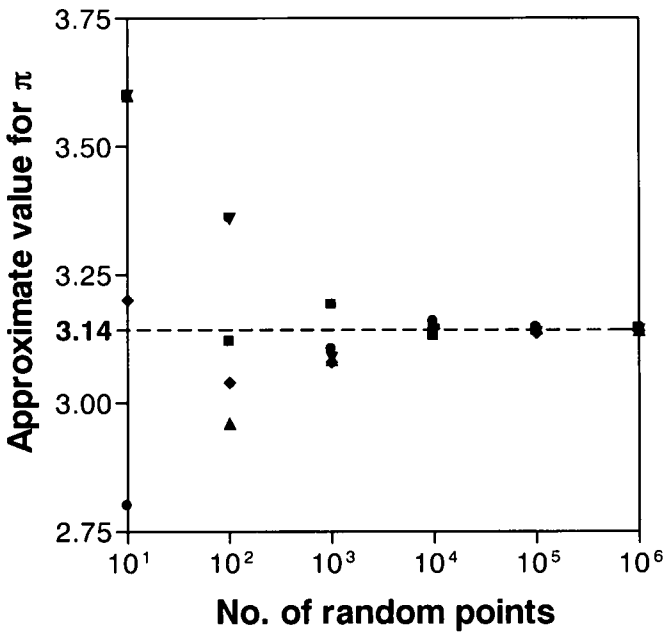

Figure A.2: An approximation for the value of π as function of the number of random points used in the Monte Carlo method. The accuracy of the approximation increases as the number of random points is increased.

trajectories in the phosphor. Since an energy loss profile is determined using these electron trajectories, the approximation's accuracy is increased by increasing the number of simulated trajectories. For the simulations performed in Chapter 4 good statistics is obtained when 10^5 trajectories is used, but this results in a computational time of about 11 hours on a 400 MHz PC after the code was compiled to a stand-alone DOS program from the MATLAB source code. To speed up these calculations the same DOS program was executed on a group of computers, with similar parameters except for the thickness of the ZnO layer that was varied from one computer to the next.

A.3 The period of the random generator

The random number generator used in this study to perform the Monte Carlo simulations was the native MATLAB version. The generator can generate all the floating point numbers in the closed interval [2^{-53}, 1-2^{-53}] and theoretically can generate over 2^{1492} values before repeating itself.

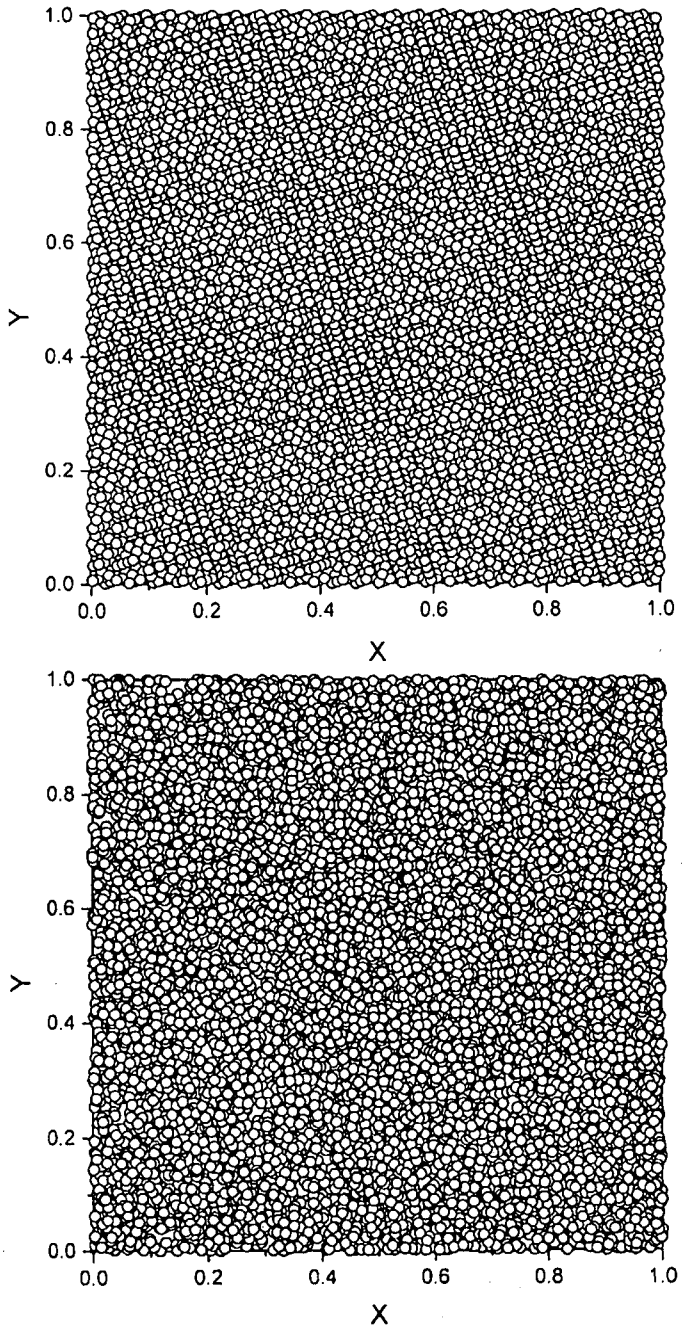

Figure A.3: **A "parking lot" test on two different random number generators. 10^5 points are plotted using consecutive pairs of random numbers as x- and y-coordinates. The top graph is an example of a "bad" generator because it exhibits a striped pattern. The bottom graph is an example of a "good" generator [69].**

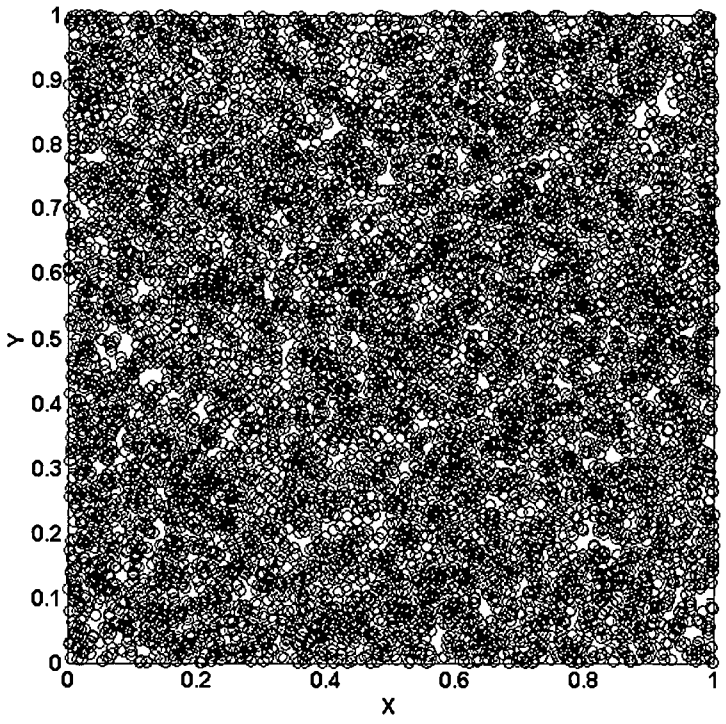

Figure A.4: A test for the native Matlab random number generator using a similar method used in Figure A.3.

In Figure A.3 two graphs is shown created with two different random number generators. Each graph contains 10^5 points plotted using consecutive pairs of random numbers as x- and y-coordinates. The top graph is an example of a "bad" generator because it exhibits a striped pattern while the bottom graph is an example of a "good" generator. The native MATLAB random number generator code was tested using this method and the result is shown in Figure A.3.

Comparing Figure A.3 with the bottom graph in Figure A.3 indicates the adequate randomness of the MATLAB-generator.

Appendix B

The NIST database

B.1 Introduction

Much attention has been devoted to the problem of elastic scattering of photoelectrons and Auger electrons in solids. It has been found that elastic electron collisions in the solid should be accounted for in the mathematical formalism of quantitative analysis by Auger electron spectroscopy and X-ray photoelectron spectroscopy. In these spectroscopies elastic collisions are neglected, assuming the electrons follow linear trajectories. This formalism may not be sufficiently accurate for all solids, energies, or experimental conditions and require a more reliable theory to describe the elastic electron scattering process in solids. The theoretical models describing the inelastic electron backscattering from surfaces also need cross sections for the elastic scattering events in the solid. All of the above theoretical models require knowledge of differential and total elastic scattering cross sections.

B.2 The theory of elastic scattering of electrons

Elastic scattering processes involve a change in direction of an electron on collision with a scattering center described by a particular potential. Such events may occur when an electron encounters an atomic layer in a solid. The elastic interactions influence the electron's trajectory in the solid, particularly for large scattering angles, and must be accounted for in a theoretical description of electron transport. The corresponding theoretical approaches are based on a number of assumptions specifying the structure of the solid as well as the interaction of an electron with the solid. The following assumptions concerning the electron and solid is made:

- The solid is a set of randomly distributed scattering centers which corresponds to the atoms in the solid. The solid is therefore assumed to be amorphous or polycrystalline so that diffraction phenomena can be neglected.
- The incident electron interacts with only one scattering center during a scattering event. The potentials of other centers are neglected.
- Each scattering center in the solid is approximated by the potential of the corresponding isolated atom.

Therefore an accurate description of the two-body interaction between an electron and a scattering center is required in the theoretical description of electron transport. The elastic scattering of an electron by an atom is a well known problem in quantum mechanics and associated with tedious calculations. However, in practice a number of additional assumptions are made to simplify the numerical calculation of the scattering potential.

It is convenient to describe the scattering event in terms of a quantity referred to as the *scattering cross section*. Suppose that a flux of electrons with density of N particles per unit area per second is scattered by a certain potential $V(r)$. This potential is usually assumed to have spherical symmetry. The number of electrons n scattered into a small solid angle is proportional to the density N and the solid angle $\Delta\Omega$. The proportionality coefficient is called the differential elastic scattering cross section and is denoted by $d\sigma/d\Omega$:

$$n = \frac{d\sigma}{d\Omega} N \Delta\Omega \tag{B.1}$$

The quantity $(d\sigma/d\Omega)\Delta\Omega$ has the dimension of length squared and can be considered as the fraction of the cross section of the incoming electron beam which is scattered into the solid angle $\Delta\Omega$. On integration of the differential elastic scattering cross section over all scattering angles, the total elastic scattering cross section is obtained:

$$\sigma_t = \int_{4\pi} \frac{d\sigma}{d\Omega} d\Omega \tag{B.2}$$

The total cross section σ_t also has the dimension of length squared. Because of spherical symmetry of the scattering potential, the scattering problem also has cylindrical symmetry. This means that the probability of elastic scattering at a polar angle θ is not a function of the azimuthal angle. A description of electron scattering by a given scattering center requires

knowledge of the probability density function of the polar scattering angles. This function $H(\theta)$ can be expressed in terms of the elastic scattering cross sections as follows:

$$H(\theta) = \frac{d\sigma/d\theta}{\sigma_t} = \frac{(d\Omega/d\theta)(d\sigma/d\Omega)}{\sigma_t} = \frac{2\pi sin\theta(d\sigma/d\Omega)}{\sigma_t} \tag{B.3}$$

B.3 Methods to calculate the elastic scattering cross section

The interaction between an electron and the potential $V(r)$ is described by the Schrödinger equation:

$$\left[\Delta + K^2 - \frac{2m}{\hbar^2}V(r)\right]\psi(r) = 0 \tag{B.4}$$

where K is the length of the wave vector describing the incoming electron of energy E:

$$K = \sqrt{\frac{2mE}{\hbar^2}} \tag{B.5}$$

and where m is the electron mass and $\hbar$ is Planck's constant divided by 2π. At large distances from the scattering center, the solution $\psi(r)$ should approach a superposition of the incident plane wave and the outgoing spherical wave:

$$\psi(r) \underset{r\to\infty}{\to} e^{i\mathbf{K}\cdot\mathbf{r}} + \frac{1}{r}f(\theta)e^{i\mathbf{K}\cdot\mathbf{r}} \tag{B.6}$$

The amplitude of the spherical wave and therefore also the scattering probability is usually only a function of the polar scattering angle θ. The functional dependence on the angle θ is accounted for by a function $f(\theta)$ called the scattering amplitude. It can be proven that [70]:

$$\frac{d\sigma}{d\Omega} = |f(\theta)|^2 \tag{B.7}$$

Thus, knowledge of the function $f(\theta)$ is sufficient in order to determine the differential elastic scattering cross section and, on integration, the total elastic scattering cross section. From Equation B.3 the distribution of the polar scattering angles for a given scattering center is obtained. Using the so-called partial wave expansion method (PWEM), the scattering amplitudes

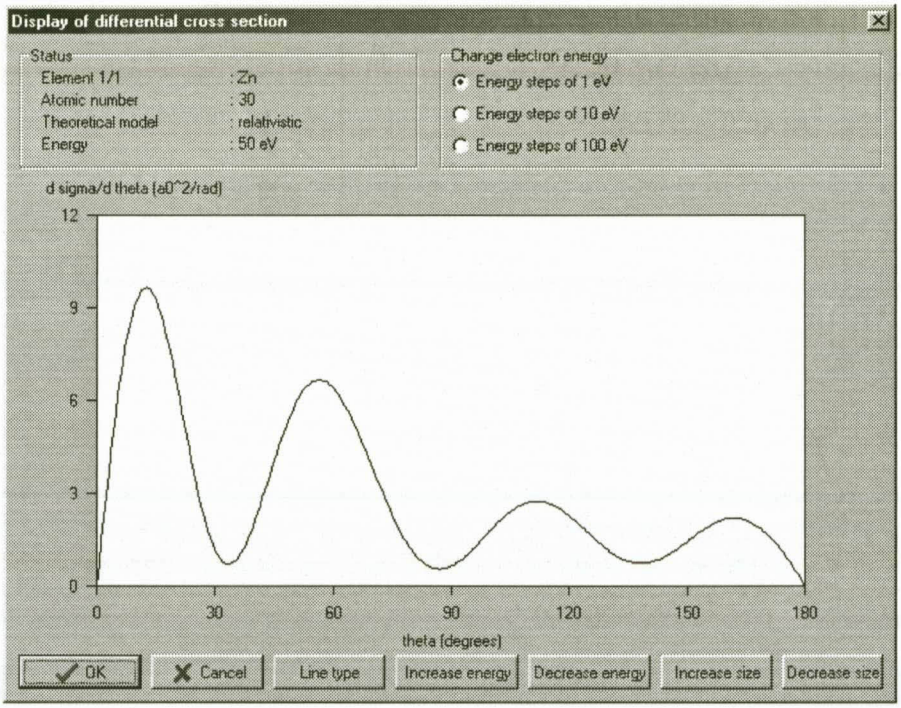

Figure B.1: A screen shot of a window displaying the differential scattering cross section of Zn at 50 eV. The same graph is displayed in Figure B.4(a).

$f(\theta)$ using both relativistic and nonrelativistic approaches can be calculated. For a detailed discussion concerning these approaches, see the NIST database reference material [35]. Generally the relativistic approach is considered to be more reliable of the two approaches [71, 72].

B.4 Using the database

Elastic scattering cross sections are available in published tabulations [71, 73, 74, 75, 76, 77, 78], but the data are not complete and generally not in the form of a computer controlled database. The best database currently available on this subject is that of the National Institute of Standards and Technology (NIST) in Maryland, USA developed by Proff. A. Jablonksi and S. Tougaard. The NIST's Elastic electron scattering cross section database is part of their Standard Reference Data program. The database provides nonrelativistic and relativistic elastic electron scattering cross sections for elements with atomic numbers between 1 and 96 and for electron energies between 50 eV and 9999 eV.

The database is able to provide the differential elastic scattering cross sections in different coordinate systems (See Figure B.4 for an example), create files containing the elastic scattering cross section for specified elements, energies and coordinate systems and parameters for a random number generator to provide the polar scattering angles used in Monte Carlo electron trajectory simulations.

In Figure B.4(a), (b) and (c) the relativistic differential cross section for Zn at 50, 500 and 5000 eV is shown in the coordinate system of $d\sigma/d\theta$ vs. θ. Cross sections in these coordinates are obtained after integration of the differential cross section $d\sigma/d\Omega$ with respect to the azimuthal angle at a constant polar angle θ:

$$\frac{d\sigma}{d\theta} = 2\pi \frac{d\sigma}{d\Omega} \sin\theta \tag{B.8}$$

Using these files, the database is able to generate parameters that is used by a random number generator to provide the scattering angles for variable electron energies. This generator provides the polar scattering angles at any specified energy in the range from 50 eV to 9999 eV and is ideal for simulations of electron trajectories with decreasing energy as a result of inelastic collisions. The generator is supplied in the form of Fortran source code that generates a large number of scattering angles which is then displayed in the form of a histogram. In Figure B.4 a comparison is shown between the relativistic differential cross section for Zn at 50 eV (Obtained from the NIST database) and a histogram consisting of 10000 random scattering angles (Obtained using the generated files and the Fortran source code).

B.5 Converting Fortran files to Matlab MEX-files

Although MATLAB is a complete and self-contained environment for programming and manipulating data, it is also sometimes useful to interact with data and programs outside the MATLAB environment. For this reason an Application Program Interface (API) supporting these external interfaces is provided. One of these supported functions is the ability to call C or Fortran programs from within MATLAB. Fortran MEX-files are built by using the original Fortran code together with additional calls to API routines that interfaces the Fortran computational routine with MATLAB. Once compiled, these files are referred to as MEX-files (Matlab Executable) and are dynamically linked subroutines that the MATLAB interpreter can automatically load and execute just like any other built-in MATLAB function. For a complete technical reference on the compilation of MEX-files refer to the MATLAB documentation [79].

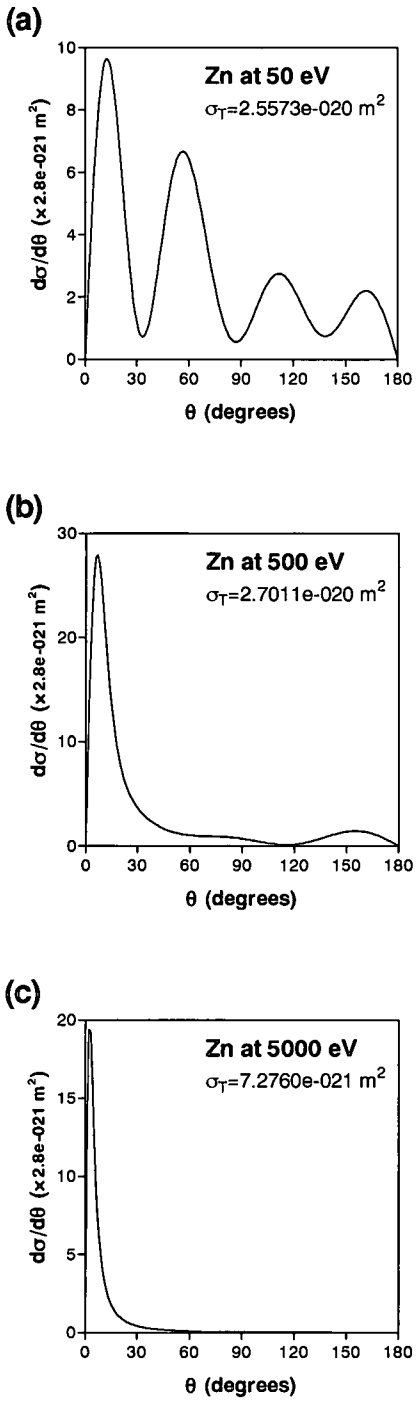

Figure B.2: The relativistic differential cross section as function of the angle θ for Zn at (a) 50, (b) 500 and (c) 5000 eV calculated according to the NIST database [35].

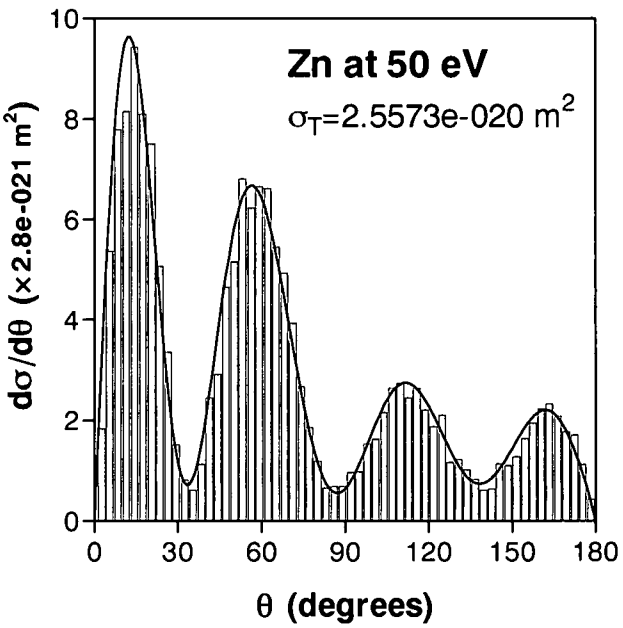

Figure B.3: The relativistic differential cross section as function of the angle θ for Zn at 50 eV and compared to a histogram consisting of 10^4 random scattering angles. The cross section was calculated using the NIST database program itself, while the histogram was calculated using the supplied Fortran source code.

B.6 MEX-file listing

Below a complete listing is given of the MEX-file used to obtain the scattering angles from the NIST database. The first (indented) part contains the API routines necessary to interface the code with the MATLAB interpreter. The second (non-indented) part contains the original Fortran source code supplied with the NIST database to provide the scattering angles for variable electron energies using a random number generator. In the MATLAB environment, a call to the MEX-file named `nist2.dll` has the following syntax:

```
[theta,sigma]=nist2(A,E)
```

where `theta` is the polar scattering angle given in degrees and `sigma` is the total elastic scattering cross section given in m^2 for an element with atomic number A at an energy E given in eV.

```
C     CALCULATE THETA AND SIGMA FROM NIST DATABASE
C     FOR VARIABLE ENERGY FILES
C     A.P. GREEFF 30/03/2000
C
C               THIS IS A MEX GATEWAY FUNCTION FOR MATLAB
C
                      SUBROUTINE mexFunction(nlhs,plhs,nrhs,prhs)
                      IMPLICIT REAL*8(A-H,Q-Z)
                      INTEGER plhs(*),prhs(*)
                      INTEGER mxCreateFull
                      INTEGER z_pr,energy_pr,theta_pr,sigma_pr
                      INTEGER nlhs,nrhs
                      INTEGER mxGetM,mxGetN,mxIsNumeric
                      REAL*8 z,energy,theta,sigma

C               CHECK FOR PROPER NUMBER OF ARGUMENTS

                      IF (nrhs .NE. 2) THEN
                            CALL mexErrMsgTxt('2 inputs required.')
                      ELSEIF (nlhs .ne. 2) THEN
                            CALL mexErrMsgTxt('2 ouputs required.')
                      ENDIF

C               CHECK TO SEE BOTH INPUTS ARE NUMERIC

                      IF (mxIsNumeric(prhs(1)) .ne. 1) THEN
                            CALL mexErrMsgTxt('Input #1 is not numeric.')
                      ELSEIF (mxIsNumeric(prhs(2)) .ne. 1) THEN
                            CALL mexErrMsgTxt('Input #2 is not numeric.')
                      ENDIF

C               CHECK THAT INPUT #1 IS A SCALAR

                      m=mxGetM(prhs(1))
                      n=mxGetN(prhs(1))
                      IF(n .ne. 1 .or. m .ne. 1) THEN
                            CALL mexErrMsgTxt('Input #1 is not a scalar.')
                      ENDIF

C               CHECK THAT INPUT #2 IS A SCALAR

                      m=mxGetM(prhs(2))
                      n=mxGetN(prhs(2))
                      IF(n .ne. 1 .or. m .ne. 1) THEN
                            CALL mexErrMsgTxt('Input #2 is not a scalar.')
                      ENDIF

C               CREATE MATRIX FOR THE RETURN ARGUMENT

                      plhs(1)=mxCreateFull(1,1,0)
                      plhs(2)=mxCreateFull(1,1,0)
                      z_pr=mxGetPr(prhs(1))
                      energy_pr=mxGetPr(prhs(2))
                      theta_pr=mxGetPr(plhs(1))
                      sigma_pr=mxGetPr(plhs(2))
```

```
C                LOAD THE DATA INTO FORTRAN ARRAYS

                       CALL mxCopyPtrToReal8(z_pr,z,1)
                       CALL mxCopyPtrToReal8(energy_pr,energy,1)

C                CALL THE COMPUTATIONAL SUBROUTINE

                       CALL NIST2(z,energy,theta,sigma)

C                LOAD THE OUTPUT INTO A MATLAB ARRAY

                       CALL mxCopyReal8ToPtr(theta,theta_pr,1)
                       CALL mxCopyReal8ToPtr(sigma,sigma_pr,1)
                       RETURN
                       END

C                 CALL THE ORIGINAL FORTRAN ROUTINE

                       SUBROUTINE NIST2(z,energy,theta,sigma)
                       IMPLICIT REAL*8(A-H,Q-Z)

                       index=3
                       idum=1
                       icross=2
                       iz=z
                       theta=GENER(index,idum,icross,iz,energy,sigma)

                       RETURN
                       END

C     THIS IS THE ORGINAL FORTRAN CODE (EXAMPLE2.FOR) BY A.
C     JABLONKSKI FOR ACCESS TO NIST DATABASE
C     ***************************************************************
C


      FUNCTION GENER(INDEX,IDUM,ICROSS,IZ,ENERGY,SIGMA)
      IMPLICIT real*8(A-H,O-Z)
      REAL X1
      COMMON DL50,PARAM,V(98),SPWEM(61)
      COMMON /ALPHA/X1(61,201)
      SAVE /ALPHA/
      IF (IDUM .GT. 0) THEN
        DL50=DLOG(5.0D1)
        PARAM=(DLOG(9.999D3)-DL50)/6.0D1
        END IF
      DLENER=DLOG(ENERGY)
      J=1+IDINT((DLENER-DL50)/PARAM)
      E2=DL50+J*PARAM
      E1=E2-PARAM
      IF (DLENER-E1 .LT. E2-DLENER) I=J
      IF (DLENER-E1 .GE. E2-DLENER) I=J+1
      K=1+IDINT(200*RANDOMNUMBER(IDUM,ICROSS,IZ))
      RA=RANDOMNUMBER(IDUM,ICROSS,IZ)
      X=(X1(I,K+1)-X1(I,K))*RA
      Q=X1(I,K)+X
```

```
      COM=1.0D0-2.0D0*Q*Q
      IF (INDEX .EQ. 1) THEN
        IF (COM .GE. 1.0D0) COM=1.0D0
        IF (COM .LE. -1.0D0) COM=-1.0D0
        GENER=COM
        END IF
      IF (INDEX .EQ. 2 .OR. INDEX .EQ. 3) THEN
        IF (COM .GE. 1.0D0) X=0.0D0
        IF (COM .LE. -1.0D0) X=3.1415926535898D0
        IF (COM .LT. 1.0D0 .AND. COM .GT. -1.0D0) X=DACOS(COM)
        IF (INDEX .EQ. 2) GENER=X
        IF (INDEX .EQ. 3) GENER=X*5.729577951308D1
        END IF
      SIGMA=CROSS(ENERGY)*2.800D-21
      RETURN
      END
C
C     ****************************************************************
C
      FUNCTION CROSS(ENERGY)
      IMPLICIT real*8(A-H,O-Z)
      COMMON DL50,PARAM,V(98),SPWEM(61)
      DLENER=DLOG(ENERGY)
      J=1+IDINT((DLENER-DL50)/PARAM)
      IF (J .EQ. 1) THEN
        E0=DL50
        E1=E0+PARAM
        E2=E1+PARAM
        CROSS=VALUE(E0,E1,E2,SPWEM(1),SPWEM(2),SPWEM(3),DLENER)
      ENDIF
      IF (J .GT. 1 .AND. J .LT. 61) THEN
        E0=DL50+(J-2)*PARAM
        E1=E0+PARAM
        E2=E1+PARAM
        CROSS=VALUE(E0,E1,E2,SPWEM(J-1),SPWEM(J),SPWEM(J+1),DLENER)
      ENDIF
      IF (J .GE. 61) THEN
        E0=DL50+58*PARAM
        E1=E0+PARAM
        E2=E1+PARAM
        CROSS=VALUE(E0,E1,E2,SPWEM(59),SPWEM(60),SPWEM(61),DLENER)
      ENDIF
      RETURN
      END
      FUNCTION VALUE(A,B,C,Y0,Y1,Y2,X)
      IMPLICIT real*8(A-H,O-Z)
      P1=(X-B)*(X-C)*Y0/((A-B)*(A-C))
      P2=(X-A)*(X-C)*Y1/((B-A)*(B-C))
      P3=(X-A)*(X-B)*Y2/((C-A)*(C-B))
      VALUE=P1+P2+P3
      RETURN
      END
C
C     ****************************************************************
C
      FUNCTION RANDOMNUMBER(IDUM,ICROSS,IZ)
```

```
C
C     THE RANDOM NUMBERS ARE SUBMITTED HERE TO THE RANDOMIZING SHUFFLE.
C
      IMPLICIT real*8(A-H,O-Z)
      REAL X1
      COMMON DL50,PARAM,V(98),SPWEM(61)
      COMMON /ALPHA/X1(61,201)
      DIMENSION MAT(10)
      CHARACTER CHF,CHZ*2,CHD*8
      IF (IDUM.GT.0) THEN
C
C       DETERMINE THE NAME OF THE FILE WITH PARAMATERS FOR THE
C       RANDOM NUMBER GENERATOR
C
        IF (ICROSS .EQ. 1) CHF='D'
        IF (ICROSS .EQ. 2) CHF='E'
        IZZ=IZ
        CALL DIGIT(IZZ,2,MAT)
        CHZ=CHAR(48+MAT(1))//CHAR(48+MAT(2))
        CHD='D'//CHF//CHZ//'.001'
C
C       READ THE PARAMETERS FOR THE RANDOM NUMBER GENERATOR
C
        OPEN(1,FILE=CHD,STATUS='OLD')
        READ(1,*)EDUM
        DO 10 J=1,61
        READ(1,*)SPWEM(J)
        DO 20 I=1,201
        READ(1,*)X1(J,I)
  20    CONTINUE
  10    CONTINUE
        CLOSE(1)

        DO 11 J=1,97
CALL RANDOM_NUMBER(RRR)
DUM=RRR
C        DUM=RANG(IDUM)
  11    CONTINUE
        DO 12 J=1,97
CALL RANDOM_NUMBER(RRR)
V(J)=RRR
C        V(J)=RANG(IDUM)
  12    CONTINUE
CALL RANDOM_NUMBER(RRR)
V(98)=RRR
C        V(98)=RANG(IDUM)
        ENDIF
      J=1+INT(9.7D1*V(98))
      V(98)=V(J)
      RANDOMNUMBER=V(98)
CALL RANDOM_NUMBER(RRR)
V(J)=RRR
C      V(J)=RANG(IDUM)
      RETURN
      END
      FUNCTION RANG(IDUM)
```

```
      IMPLICIT real*8(A-H,O-Z)
      REAL X
      IF (IDUM .GT. 0) THEN
      CALL NSEED(1)
      IDUM=-1
      ENDIF
  100 CONTINUE
      CALL NRANDOM(X)
      IF (X .LE. 0.0) GO TO 100
      RANG=X
      RETURN
      END
C
C     ****************************************************************
C
      SUBROUTINE DIGIT(N,L,M)
C
C     SUBPROGRAM DECOMPOSES AN INTEGER NUMBER INTO THE SEPARATE DIGITS.
C     LAST DIGIT OF THE INTEGER N IS CONTAINED IN L-TH ELEMENT OF THE
C     TABLE M. IF THE NUMBER N HAS L DIGITS, THE FIRST DIGIT IS
C     CONTAINED IN THE FIRST ELEMENT OF THE TABLE M. IF THE NUMBER N
C     HAS LESS THAN L DIGITS, FIRST ELEMENTS OF THE TABLE M CONTAIN
C     ZEROS.
C
C     INPUT PARAMETERS
C     N - AN INTEGER NUMBER
C     C - NUMBER OF THE CONSIDERED DECIMAL PLACES
C
C     OUTPUT PARAMETERS
C     M - TABLE CONTAINING L DIGITS OF THE NUMBER N
C
      IMPLICIT real*8(A-H,O-Z)
      DIMENSION M(10)
      DO 10 I=1,10
      M(I)=0
   10 CONTINUE
      DO 20 I=1,L
      J=MOD(N,10)
      N=(N-J)/10
      M(L-I+1)=J
   20 CONTINUE
      RETURN
      END
C
C     ****************************************************************
C
C     THE FOLLOWING SUBPROGRAMS GENERATE THE RANDOM NUMBERS UNIFORMLY
C     DISTRIBUTED OVER THE INTERVAL FROM 0 TO 1.
C     THE MULTIPLICATIVE CONGRUENTIAL ALGORITHM IS USED IN CALCULATIONS
C
C     X(N+1) = 214013*X(N)+2531011 (MOD 2**31)
C
      SUBROUTINE NSEED(ISEED)
      IMPLICIT real*8(A-H,O-Z)
      REAL X
      COMMON/COMSEED/IOMODE,I1,X,D1,D2,D3
```

```
IOMODE=ISEED
I1=65536
X=32768.0
D1=214013.0D0
D2=2531011.0D0
D3=2147483648.0D0
END
SUBROUTINE NRANDOM(RANVAL)
IMPLICIT real*8(A-H,O-Z)
REAL RANVAL,X
COMMON/COMSEED/IOMODE,I1,X,D1,D2,D3
IOMODE=DMOD(IOMODE*D1+D2,D3)
RANVAL=(IOMODE/I1)/X
END
```

B.7 Computing the total elastic scattering cross section

Using the MEX-file `nist2.dll` the total elastic scattering cross section σ can be determined as a function of the electron energy for any element with atomic numbers between 1 and 96. Due to the random number generator in the MEX-file a different polar scattering angle is returned each time a call to this file is made, but the value for the total elastic scattering cross section remains constant at a given electron energy. A comparison between the scattering cross sections of Zn, S and O between 50 eV and 5000 eV is shown in Figure B.7. The data was obtained in the MATLAB environment with repeated calls to the MEX-file at different energies for each element in a `for-end` loop statement.

B.8 Computing the polar scattering angle

Different from the previous case, the polar scattering angle depends on *both* the electron energy and the value returned by the random number generator. To eliminate the randomness of the scattering angle each time a called is made to the MEX-file, the random number generator was disabled in the MEX-file and a "random" number was supplied as one of the function's arguments:

```
[theta,sigma]=nist2(A,E,R)
```

All the parameters have the same meaning as the original MEX-file with the addition of R representing a number between zero and 1. In Figure 4.6(a) and (b) the polar scattering angles are shown for S and O respectively. The data was obtained in the MATLAB environment

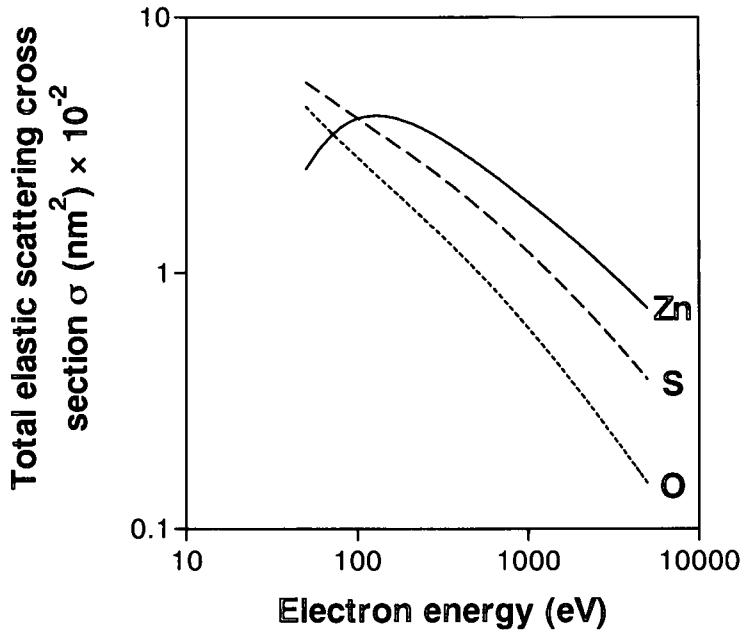

Figure B.4: A *log-log* plot showing the total elastic scattering cross section as function of electron energy for Zn, S and O.

with a two dimensional grid containing the energies E from 50 eV to 5000 eV and numbers R between 0 and 1 using the `for-end` loop statement. Using the modified MEX-file values for the polar scattering angle was obtained at each of these grid points to construct a three dimensional grid displaying the relation between the polar scattering angle, the electron energy and a random number.

B.9 Accelerating the main computational routine

During the Monte Carlo simulation of the electron trajectories, each electron is scattered several times along it's trajectory in the solid. With each of these scattering events, the total elastic scattering cross section, as well as the polar scattering angle should be known for the electron at a certain energy associated with a certain scattering center. On average, a single call to the MEX-file takes approximately 0.17 seconds on a 400 MhZ PC. Considering that the trajectories of at least 10^4 electrons should be simulated to obtain good statistical results, the problem concerning computational speed is obvious. To address this problem, the total elastic scattering cross sections and polar scattering angles is determined using the data displayed

in Figures B.4 and 4.6 and a fast linear interpolation function in the MATLAB environment. This improves the performance by about 340% and since these calculations make up the gross of the Monte Carlo computational routine, it leads to a significant speed increase. The data for the total elastic scattering cross section and the polar scattering angles values are stored in the native MATLAB data format and loaded into memory during the start of the Monte Carlo simulation.

B.10 Comparison with other available data

The obvious question when using the NIST database is whether or not it supplies total elastic scattering cross sections and polar scattering angles that is comparable with that of other models. In the documentation supplied with the NIST database extensive comparisons are made between the differential elastic scattering cross sections generated by the database and other models. However, since the original Fortran source code supplied with the database was modified to a MATLAB MEX-file, the other models used in the comparison serves as a benchmark to test whether the correct values are actually obtained from the database's generated files.

A commonly used elastic scattering cross section is the screened Rutherford cross section which has a convenient analytical form and is very straightforward to implement in a Monte Carlo calculation. However, the screened Rutherford cross section is only applicable to high energy electrons and low atomic number materials. Without correction for relativistic effects, the total screened Rutherford elastic cross section, σ_R for the scattering of an electron from a single atom can be written as:

$$\sigma_R = 5.21 \times 10^{-21} \left(\frac{Z}{E}\right)^2 \frac{\pi}{\alpha(1+\alpha)} \quad (cm^2) \tag{B.9}$$

where Z is the atomic number of the atom, E is the incident electron energy in keV and α is a screening parameter defined as:

$$\alpha = 3.4 \times 10^{-3} \frac{Z^{0.67}}{E} \quad (eV) \tag{B.10}$$

An alternative is the partial wave expansion method of the Mott scattering cross section proposed by Reimer and Lodding [78]. This is the same theory that the NIST database is based upon. A simplification, proposed by Browning et al. [80, 81], extracts the trends from

the Mott scattering results and use this to apply corrections to the screened Rutherford model. The elastic scattering cross section is given by:

$$\sigma = 4.7 \times 10^{-18} \frac{(Z^{1.33} + 0.032Z^2)}{(E + 0.0155Z^{1.33}E^{0.5})} \times \frac{1}{(1 - 0.02Z^{0.5}e^{-u^2})} \quad (cm^2) \tag{B.11}$$

with u defined as:

$$u = log_{10}(8 \times E \times Z^{-1.33}) \tag{B.12}$$

A comparison between the total elastic scattering cross sections calculated using these two expression and that obtained from the NIST database is shown in *log-log* plots in Figure B.10 for (a) Zn, (b) S and (c) O atoms. The screened Rutherford method is labeled TECS1 and the empirical Mott method TECS2. For elements with low atomic numbers, all three methods give agreeable results. However, as the atomic number increases, the difference in values between the various models becomes more extreme. Another noticeable difference is the decrease in the cross section for Zn atoms according to the NIST database, while the other models show an increase.

Using the screened Rutherford scattering model, the polar scattering angles is determined in the following way. The probability $P(\theta)$ for elastic scattering into an angular range from 0 to a given angle θ_1 can be found by integrating the probability density function $H(\theta)$ given in Equation B.3:

$$P(\theta) = \int_0^{\theta_1} H(\theta) d\theta = \int_0^{\theta_1} \frac{2\pi \sin\theta (d\sigma/d\Omega)}{\sigma_R} d\theta \tag{B.13}$$

Expressing the probability $P(\theta)$ as a random number R between 0 and 1, Equation B.13 can be rewritten as [82]:

$$\cos\theta = 1 - \frac{2\alpha R}{1 + \alpha - R} \tag{B.14}$$

where α is the screening parameter previously defined. Using this expression, the polar scattering angles as function of the electron energy and a random number can be generated. The scattering angles associated with a S atom is shown in Figure B.10. Comparing this to the scattering angles generated with the NIST database, Figure 4.6(a), the two graphs are very similar.

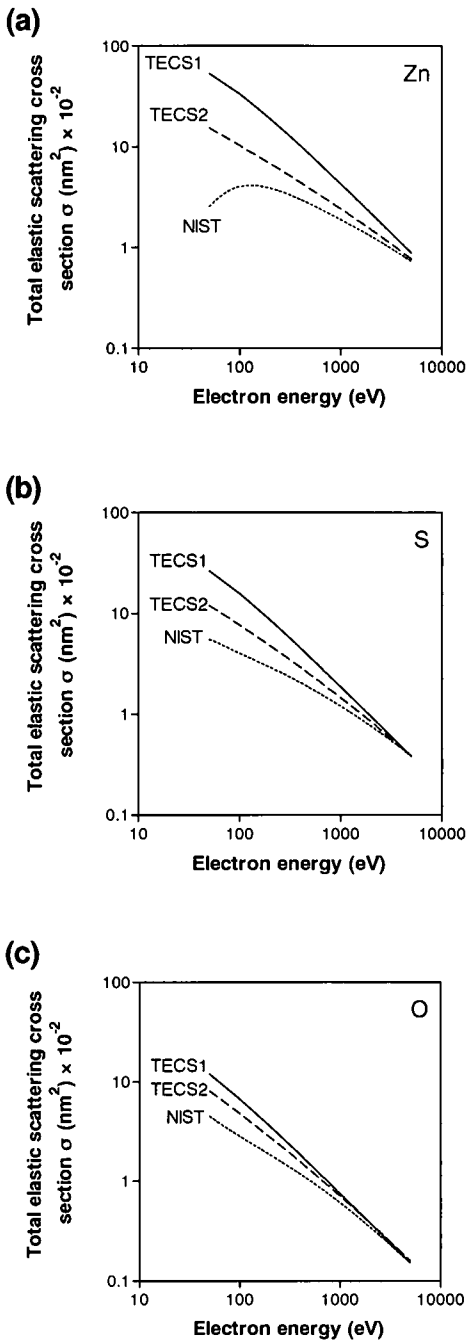

Figure B.5: The total elastic scattering cross section as function of the electron's energy for (a) Zn, (b) S and (c) O atoms calculated using different scattering models. The label `NIST` refers to the NIST database, `TECS1` to the screened Rutherford scattering model and `TECS2` refers to the empirical Mott scattering model.

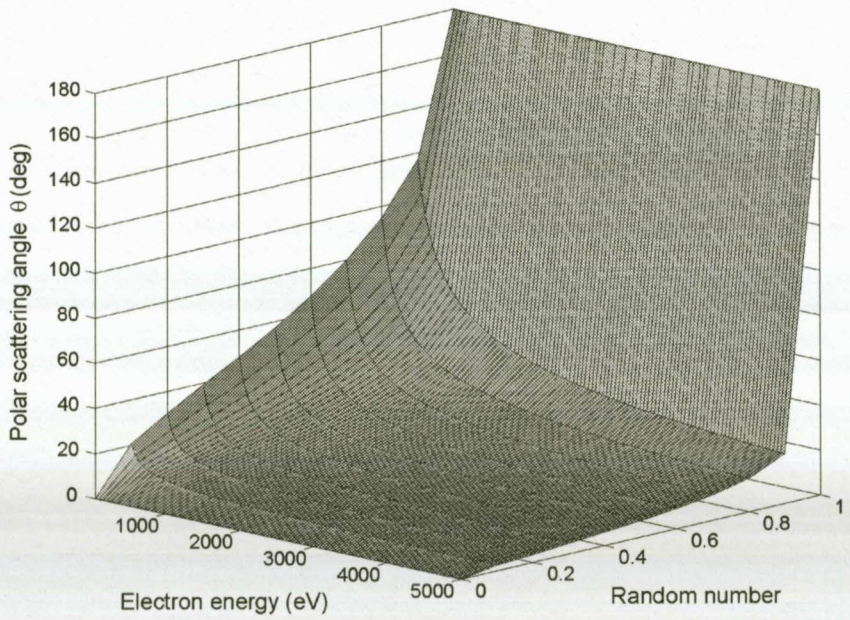

Figure B.6: The polar scattering angles for S atoms as function of the electron energy and a random number according to the Rutherford scattering model. Compare this with the results from the NIST database displayed in Figure 4.6(a) on page 51.

Appendix C

Coordinate transformations

C.1 Transforming from spherical to Cartesian coordinates

Whenever electrons of sufficient energy penetrate a solid, scattering occurs from atoms in the solid, changing the trajectory of the incident electron. Such a scattering event is shown in Figure C.1. The scattering vector itself can be described in terms of three variables: the azimuthal scattering angle ϕ, the polar scattering angle θ and the step length r to the next scattering position. In Figure C.1 these three parameters are indicated in the $x'y'z'$-coordinate system. The direction of the trajectory is therefore determined by two angles. Keeping the polar scattering angle θ fixed, possible electron trajectories is indicated for other azimuthal scattering angles ϕ. These possible trajectories form a so-called scattering cone associated with a fixed polar scattering angle.

Given the (r, θ, ϕ) values of a scattering event, these values can be transformed to a chosen set of Cartesian coordinates (x', y', z') in the following way. Referring back to Figure C.1, the projection of a vector of length r in the ϕ and θ direction onto the $x'y'$-plane yields the components $x' = pcos(\phi)$ and $y' = psin(\phi)$. The component of a projection onto the z'-axis is $z' = rcos(\theta)$. But $p = rsin(\theta)$ and therefore:

$$\begin{aligned} x' &= rsin(\theta)cos(\phi) \\ y' &= rsin(\theta)sin(\phi) \\ z' &= rcos(\theta) \end{aligned} \tag{C.1}$$

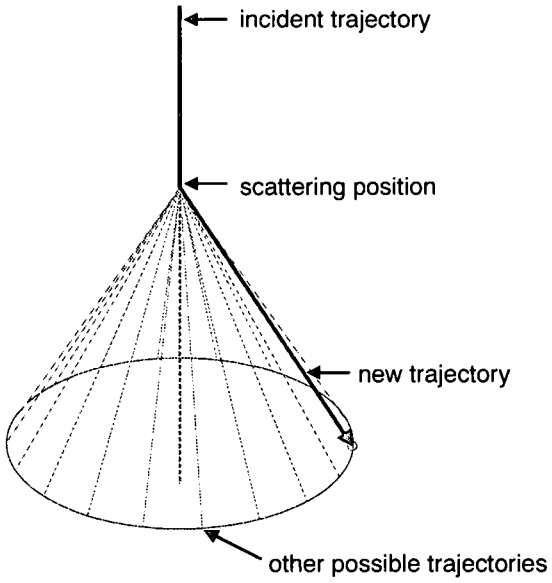

Figure C.1: **When an incident electron is scattered by an atom in a solid, the electron's trajectory changes according to physical laws describing the scattering event. Several possible electron trajectories are possible, as indicated by the scattering cone.**

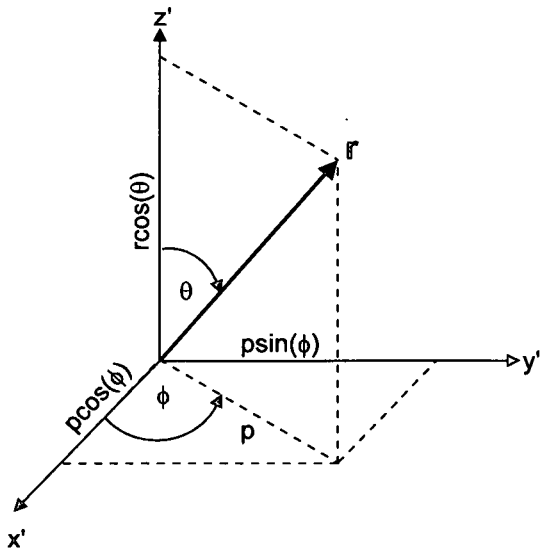

Figure C.2: **The scattering vector r can be expressed in terms of three parameters: the length of the vector r, the polar scattering angle θ and the azimuthal scattering angle ϕ.**

or expressed in the form of a spherical transformation matrix $\mathbf{R}$:

$$\mathbf{R} = \mathbf{r} \begin{bmatrix} \sin(\theta)\cos(\phi) \\ \sin(\theta)\sin(\phi) \\ \cos(\theta) \end{bmatrix} \tag{C.2}$$

C.2 Rotating Cartesian coordinates

In the previous section the transformation from spherical to Cartesian coordinates took place in the reference frame of $x'y'z'$-coordinates. But, assuming the electron's reference frame is represented by the $x'y'z'$-coordinates, it is not always identical to the "laboratory" xyz-coordinates. When the electron penetrates the solid at an angle normal to the surface, the electron's initial trajectory is parallel to the z-axis of the "laboratory" coordinates. Therefore the first scattering vector can be described in terms of either $x'y'z'$ or xyz-coordinates by only applying the transformation matrix $\mathbf{R}$. But after the first scattering event, the electron's reference frame rotates according to the scattering angles ϕ and θ. Now the electron's reference frame is not the same as that of the "laboratory" coordinates anymore. To express the scattering vector in terms of xyz-coordinates, the transformation matrix $\mathbf{R}$ should first be applied to project the vector onto the $x'y'z'$ coordinates. These coordinates should again be projected onto the reference frame of the xyz-coordinates. In this manner the electron's reference frame is rotated to align with the "laboratory" reference frame. See Figure C.2 for an illustration.

For a rotation about the z-axis, Figure C.2, the angle between the rotating axes is α. For rotations around the y- and z-axes the angles between the rotating axes are β and γ respectively. As matrices, each of these rotations can be expressed as:

$$\mathbf{X} = \begin{bmatrix} 1 & 0 & 0 \\ 0 & \cos(\alpha) & \sin(\alpha) \\ 0 & -\sin(\alpha) & \cos(\alpha) \end{bmatrix} \tag{C.3}$$

and

$$\mathbf{Y} = \begin{bmatrix} \cos(\beta) & 0 & -\sin(\beta) \\ 0 & 1 & 0 \\ \sin(\beta) & 0 & \cos(\beta) \end{bmatrix} \tag{C.4}$$

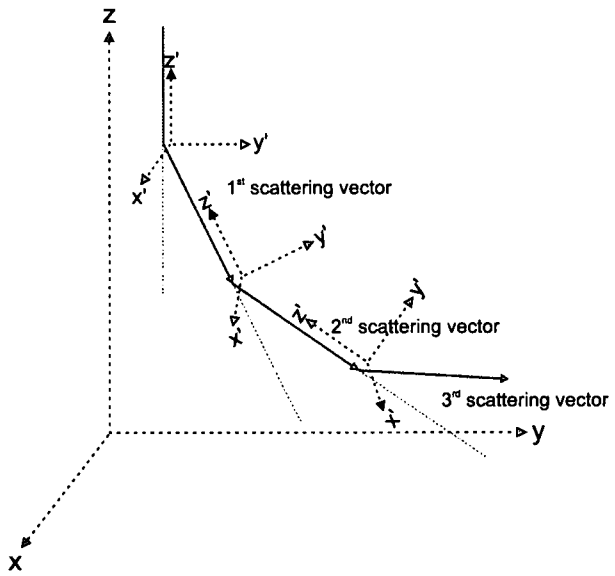

Figure C.3: Prior to the first scattering event, the electron's reference frame is identical to the "laboratory" coordinates. For the second scattering event, the electron's reference frame rotates by an amount determined by the previous scattering angles. To describe the second scattering event in terms of the "laboratory" coordinates, the electron's reference frame should be aligned with first scattering vector. The same applies for the third scattering event.

and

$$\mathbf{Z} = \begin{bmatrix} \cos(\gamma) & -\sin(\gamma) & 0 \\ \sin(\gamma) & \cos(\gamma) & 0 \\ 0 & 0 & 1 \end{bmatrix} \tag{C.5}$$

To describe the rotation of any particular reference frame within another, only two of three rotation matrices need to be applied to the coordinates.

The rotation angles is determined in the following way. To describe a scattering event in terms of the "laboratory" coordinates, the electron's reference frame should be aligned with the previous scattering vector. Therefore the two angles for the two rotation matrices is determined between the previous scattering vector and the "laboratory" coordinates.

For the rotation around the y-axis, the β-angle between the scattering vector $\mathbf{r}$ and the z-axis is:

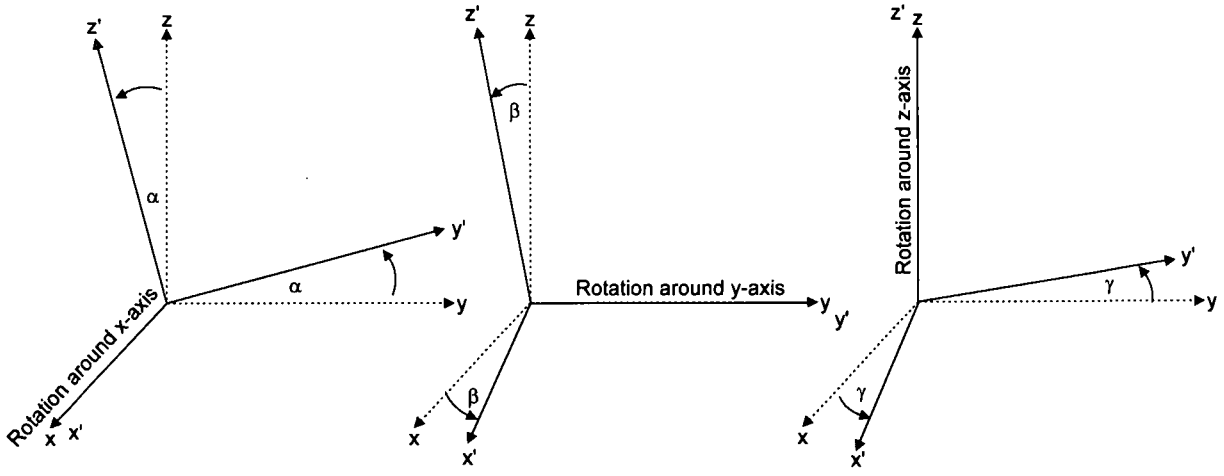

Figure C.4: In Cartesian coordinates there are three possible rotation, one around each axis. The angle α describes the rotation around the x-axis, while angles β and γ describes the rotations around the y- and z-axes.

$$cos(\beta) = \frac{\mathbf{r} \cdot \mathbf{k}}{|\mathbf{r}||\mathbf{k}|} \tag{C.6}$$

with $\mathbf{k}$ the z-axis unit vector.

For the rotation around the z-axis, the γ-angle between the projection of the scattering vector $\mathbf{r}$ onto the xy-plane and the x-axis is:

$$cos(\gamma) = \frac{\mathbf{P}_{xy}\mathbf{r} \cdot \mathbf{i}}{|\mathbf{r}||\mathbf{i}|} \tag{C.7}$$

with $\mathbf{k}$ the z-axis unit vector and $\mathbf{P_{xy}}$ the projection matrix:

$$\mathbf{P_{xy}} = \begin{bmatrix} 1 & 0 & 0 \\ 0 & 1 & 0 \\ 0 & 0 & 0 \end{bmatrix} \tag{C.8}$$

In the electron's reference frame the new position after the scattering event can be expressed as

$$\mathbf{x}' = \mathbf{x}'_0 + \mathbf{R} \tag{C.9}$$

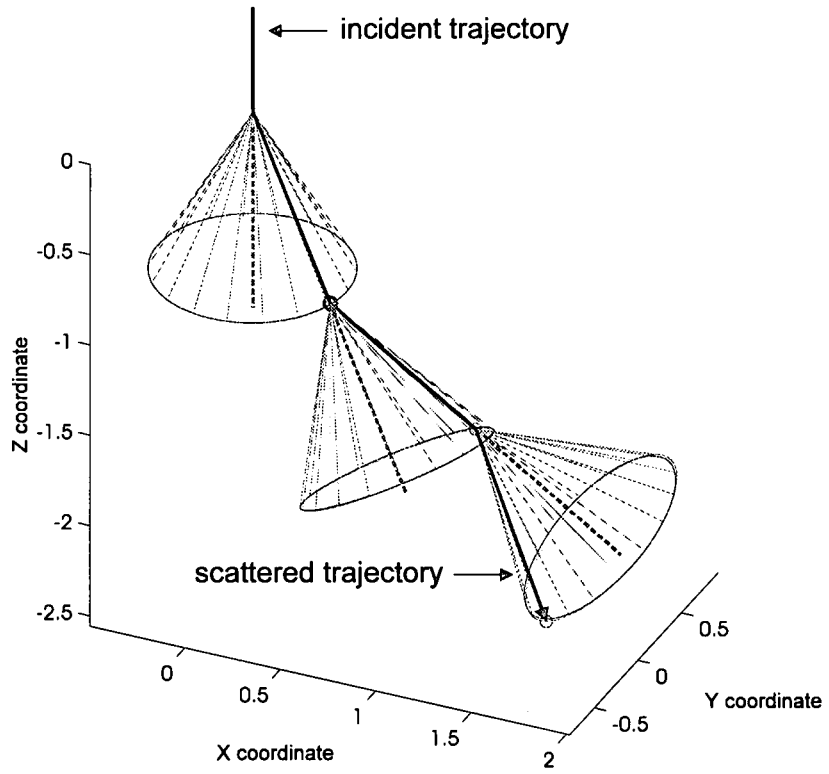

Figure C.5: Three consecutive scatter cones, all with the same polar scattering angle. The first scattering vector can be expressed in terms of $x'y'z'$-coordinates by applying the transformation matrix $\mathbf{R}$. If this electron penetrated the solid at a normal incident angle, the electron's frame of reference is similar to that of the "laboratory coordinates" and therefore "laboratory" xyz-coordinates is identical to the $x'y'z'$-coordinates. But after the first scattering event, the electron's reference frame rotated in accordance with the scattering angles ϕ and θ. The scattering vector can now be expressed in terms of $x'y'z'$-coordinates by applying the transformation matrix $\mathbf{R}$ and these coordinates projected onto xyz-coordinates by applying the rotation matrices $\mathbf{Y}$ and $\mathbf{Z}$. After the second scattering event, the electron's reference frame is rotated by an cumulative amount determined by the first event's scattering angles as well as the second event's scattering angles.

where $\mathbf{x}'$ and $\mathbf{x}'_0$ is the final and initial coordinates of the particle and $\mathbf{R}$ is the transformation matrix containing information about the length and direction of the scattering vector. Rotating this coordinate system to the "laboratory" reference frame involves the following matrix operation:

$$\mathbf{YZx}' = \mathbf{YZx}'_0 + \mathbf{YZR} \tag{C.10}$$

but since $\mathbf{YZx}' = \mathbf{x}$ and $\mathbf{YZx}'_0 = \mathbf{x}_0$, Equation C.10 becomes

$$\mathbf{x} = \mathbf{x}_0 + \mathbf{YZR} \tag{C.11}$$

with matrices $\mathbf{Y}$ and $\mathbf{Z}$ containing information about the angles of rotation between the reference frames of the electron and the "laboratory".

In Figure C.2 three consecutive scattering events are displayed. The polar scattering angle with respect to the $x'y'z'$-axis was identical for all three events and therefore the scattering cones are also identical in dimensions. The length of the scattering vector is also the same, but the azimuthal scattering angle is different for the three cones.

Appendix D

The MATLAB source code

D.1 Electron beam and grain interaction calculations

D.1.1 grains9(total,xoffset,yoffset,range,beamprofile,histres)

Refer to Section 3.4 on page 25.

This source code calculates the distribution of incident angles over a group of 9 spherical shaped phosphor grains which is each 2 μm in diameter. The parameter `total` refers to the total number of electron paths to simulate, `xoffset` and `yoffset` refers to the electron beam's x and y positional offset from the center, `range` refers to the maximum lateral spread of electron paths, `beamprofile` is a value between zero and 1 that determines the beam profile and `histres` determines the histogram's resolution. A value of 1 sets the histogram's resolution to 10 degrees while values of 2 and 3 set it to 5 and 2 degrees respectively. Refer to Section 3.4 on page 25 for a complete discussion on the effect of the parameters `range` and `beamprofile` on the distribution of incident angles.

```
function f=grains9(total,xoffset,yoffset,range,beamprofile,histres)
% GRAINS9. M Generates 9 evenly distributed spheres with
% random position for e-beam defined by vectors
% XR and YR according to error function
% 13/01/00 A.P. Greeff
%
% GRAINS9(TOTAL,XOFFSET,YOFFSET,RANGE,BEAMPROFILE,HISTRES) with
% RANGE=max 6um
% BEAMPROFILE=0 to 1
% HISTRES: 1=10deg, 2=5deg, 3=2deg
```

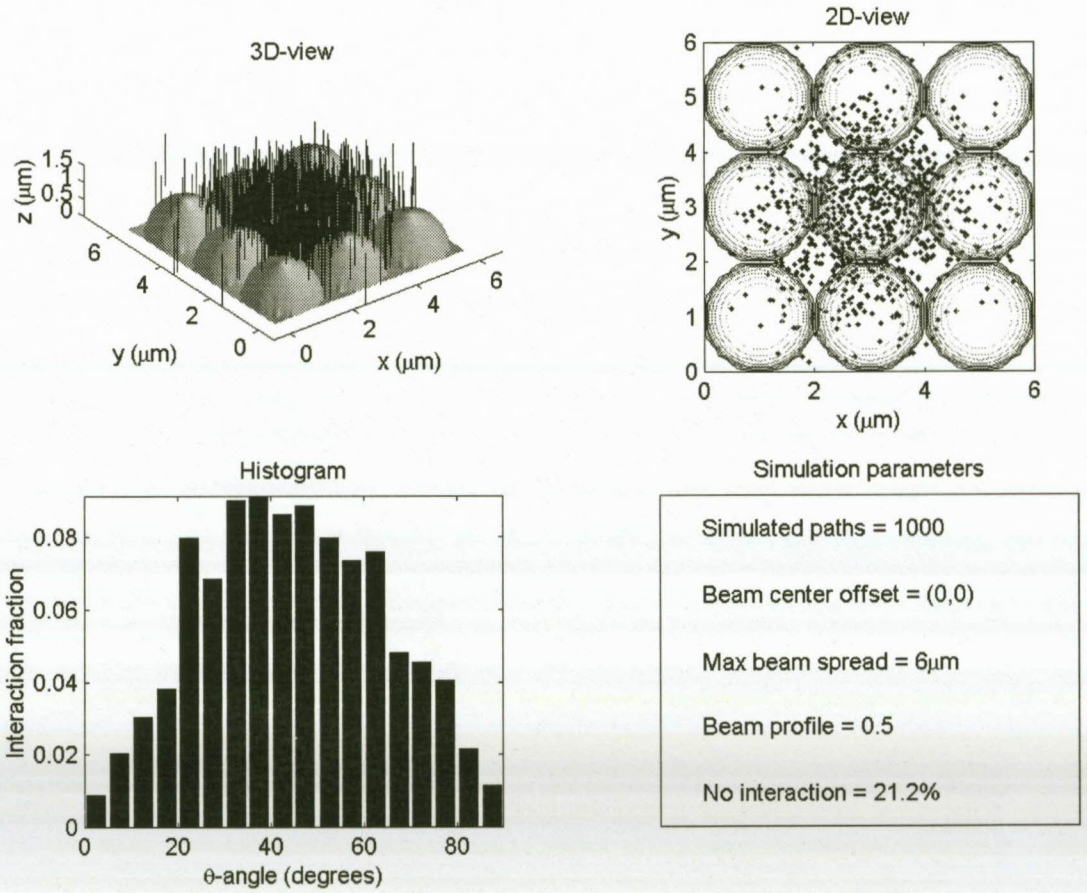

Figure D.1: The output screen of the MATLAB function `grains9.m` called from the command window using the syntax: `grains9(1000,0,0,6,0.5,2)`. Refer to the text for an explanation of the parameters. In this particular case a 10^3 electron paths were simulated with no electron beam offset. The electron beam was spread over an area of 6 $\mu m \times$ 6 μm and had a profile parameter of 0.5. The histogram resolution was set to intervals of 5^o each. The No interaction parameter in the lower right window refers to the percentage of electron paths that did not interact with any of the spheres. These paths are ignored when computing the histogram. For a simulation using 100 spheres and 10^5 electron paths, refer to Section 3.4 on page 25.

```
disp('Setting up spheres...')
[x,y]=meshgrid(0:0.1:6,0:0.1:6);
z1=sqrt(1-(x-1).^2-(y-1).^2);
z2=sqrt(1-(x-1).^2-(y-3).^2);
z3=sqrt(1-(x-1).^2-(y-5).^2);
z4=sqrt(1-(x-3).^2-(y-1).^2);
z5=sqrt(1-(x-3).^2-(y-3).^2);
z6=sqrt(1-(x-3).^2-(y-5).^2);
z7=sqrt(1-(x-5).^2-(y-1).^2);
z8=sqrt(1-(x-5).^2-(y-3).^2);
z9=sqrt(1-(x-5).^2-(y-5).^2);

% Generate (x,y) positions with MC in error function
disp('Generating random (x,y) pairs...')
randx=rand(1,total);
randy=rand(1,total);
% Distribute according to data from Oosthuizen
range=6;
xr=xoffset+(1-((erfinv(2*randx-1)/beamprofile)+4)/8)*range;
yr=yoffset+(1-((erfinv(2*randy-1)/beamprofile)+4)/8)*range;
zr=[];
theta=[];
X=[xr;xr];
Y=[yr;yr];
Z=[0;1.5];
outboundary=0;

% Sorting loop
disp('Sorting (x,y) pairs...');
for n=1:total;

   flag=0;

   %Sphere 1
   if (xr(n)-1).^2+(yr(n)-1).^2 <= 1
      zr(n)=sqrt(1-(xr(n)-1).^2-(yr(n)-1).^2);
      flag=1;
   end
   %Sphere 2
   if (xr(n)-3).^2+(yr(n)-1).^2 <= 1
      zr(n)=sqrt(1-(xr(n)-3).^2-(yr(n)-1).^2);
      flag=1;
   end
%Sphere 3
   if (xr(n)-5).^2+(yr(n)-1).^2 <= 1
      zr(n)=sqrt(1-(xr(n)-5).^2-(yr(n)-1).^2);
      flag=1;
   end
%Sphere 4
   if (xr(n)-1).^2+(yr(n)-3).^2 <= 1
      zr(n)=sqrt(1-(xr(n)-1).^2-(yr(n)-3).^2);
      flag=1;
   end
%Sphere 5
   if (xr(n)-3).^2+(yr(n)-3).^2 <= 1
      zr(n)=sqrt(1-(xr(n)-3).^2-(yr(n)-3).^2);
```

```
      flag=1;
   end
%Sphere 6
   if (xr(n)-5).^2+(yr(n)-3).^2 <= 1
      zr(n)=sqrt(1-(xr(n)-5).^2-(yr(n)-3).^2);
      flag=1;
   end
   %Sphere 7
   if (xr(n)-1).^2+(yr(n)-5).^2 <= 1
      zr(n)=sqrt(1-(xr(n)-1).^2-(yr(n)-5).^2);
      flag=1;
   end
%Sphere 8
   if (xr(n)-3).^2+(yr(n)-5).^2 <= 1
      zr(n)=sqrt(1-(xr(n)-3).^2-(yr(n)-5).^2);
      flag=1;
   end
%Sphere 9
   if (xr(n)-5).^2+(yr(n)-5).^2 <= 1
      zr(n)=sqrt(1-(xr(n)-5).^2-(yr(n)-5).^2);
      flag=1;
   end
      %If (xr,yr) is not within boundaries of grains
   if (xr(n) <=0 | xr(n) >= range) & (yr(n) <=0 | yr(n) >= range)
      disp('Out of bounds!')
      zr(n)=[];
      outboundary=outboundary+1;
   end
   if flag == 0
      zr(n)=-1;
   end
end

theta=acos(zr);

disp('Plotting...')
subplot(2,2,1)
plot3(X,Y,Z,'k')
hold on
surfl(x,y,real(z1))
disp('Sphere 1 finished...')
surfl(x,y,real(z2))
disp('Sphere 2 finished...')
surfl(x,y,real(z3))
disp('Sphere 3 finished...')
surfl(x,y,real(z4))
disp('Sphere 4 finished...')
surfl(x,y,real(z5))
disp('Sphere 5 finished...')
surfl(x,y,real(z6))
disp('Sphere 6 finished...')
surfl(x,y,real(z7))
disp('Sphere 7 finished...')
surfl(x,y,real(z8))
disp('Sphere 8 finished...')
surfl(x,y,real(z9))
```

```
disp('Sphere 9 finished...')
axis equal
shading interp
colormap gray
title('3D-view')

xlabel('x (\mum)')
ylabel('y (\mum)')
zlabel('z (\mum)')
hold off

subplot(2,2,2)
plot(xr,yr,'k.')
hold on
contour(x,y,real(z1))
contour(x,y,real(z2))
contour(x,y,real(z3))
contour(x,y,real(z4))
contour(x,y,real(z5))
contour(x,y,real(z6))
contour(x,y,real(z7))
contour(x,y,real(z8))
contour(x,y,real(z9))
title('2D-view')

axis equal
axis([0 6 0 6])
xlabel('x (\mum)')
ylabel('y (\mum)')
hold off

if histres == 1
   X=[4.5:9:85.5]
   X(11)=180;
elseif histres == 2
   X=2.5:5:87.5;
   X(19)=180;
elseif histres == 3
   X=1:2:89;
   X(46)=180;
end

N=hist(theta,X*(pi/180));
W=N/sum(N);
% Beam that had no interaction
nointeraction=W(size(X,2))*100
W=W(1:size(X,2)-1);
X=X(1:size(X,2)-1);
W=W/sum(W);
subplot(2,2,3)
bar(X,W,'k')
xlabel('\theta-angle (degrees)')
ylabel('Interaction fraction')
axis([0 90 0 max(W(1:size(X,2)-1))])
title('Histogram')
```

```
subplot(2,2,4)
groupx=[0 0 1 1 0];
groupy=[0 1 1 0 0];
plot(groupx,groupy,'k')
text(0.1,0.9,['Simulated paths = ',num2str(total)])
text(0.1,0.7,['Beam center offset = (',num2str(xoffset),',',num2str(yoffset),')'])
text(0.1,0.5,['Max beam spread = 'num2str(range) '\mum'])
text(0.1,0.3,['Beam profile = ',num2str(beamprofile)])
text(0.1,0.1,['No interaction = ',num2str(nointeraction),'%'])
axis off
title('Simulation parameters')
disp('Saving screen to "theta9.jpg"...')
print 'theta9' -djpeg
disp('Saving X and W to "theta9.dat"...')
outputdata=[X' W'];
save 'theta9.dat' outputdata -ascii
disp('Finished')

figure(1)
f=total;
```

D.2 Comparing the NIST database to other models

D.2.1 rutherford1(Z,E)

Refer to Section B.10 on page 101.

This source code calculates the total elastic scattering cross section according to the Rutherford scattering model. The parameters Z and E refers to atom's atomic number and the incident electron's energy.

```
function f=rutherford1(Z,E)
% RUTHERFORD1.M Calculate the total elastic scattering cross section in m^2
% using screened Rutherford cross section
% From: R. Browing et al. J. Vac. Sci. Technol. B9(6) (1991), pp 3578-3581
% 16/01/2000 A.P. Greeff
%
% RUTHERFORD1(Z,E) with
% Z=atomic number,
% E=electron energy (eV)

E=E*10e-3; % Convert from eV to keV
sigma=3.4e-3*Z^0.67/E; % Screening parameter
f=5.21e-21*(Z/E)^2*pi/(sigma*(1+sigma));
f=f*1e-4; % Convert from cm^2 to m^2
```

D.2.2 mott(Z,E)

Refer to Section B.10 on page 101.

This source code calculates the total elastic scattering cross section using an empirical form of the Mott scattering model. The parameters Z and E refers to atom's atomic number and the incident electron's energy.

```
function f=mott(Z,E)
% MOTT.M Calculate the total elastic scattering cross section in m^2
% using an emperical form of the Mott cross section
% From: R. Browing et al. J. Appl. Phys. 76(4) (1994), pp 2016-2022
% 16/01/2000 A.P. Greeff
%
% MOTT(Z,E) with
% Z=atomic number,
% E=electron energy (eV)

E=E*10e-3; % Convert from eV to keV
u=log10(8*E*Z^(-1.33));
f=4.7e-18*((Z^(1.33)+0.032*Z^2)/(E+0.0155*Z^(1.33)*E^(0.5)))*(1/(1-0.02*Z^(0.5)*exp(-u^2)));
f=f*1e-4; % Convert from cm^2 to m^2
```

D.2.3 rutherford2(Z,E,R)

Refer to Section B.10 on page 102.

This source code calculates the polar scattering angle using the screened Rutherford model. The parameters Z and E refers to atom's atomic number and the incident electron's energy, while R represents a random number between zero and 1.

```
function f=rutherford2(Z,E,R)
% RUTHERFORD2.M Calculate the polar scattering angle in degrees
% using a random number and the screened Rutherford scattering model
% From: D.E. Newbury et al. in "Advanced scanning electron microscopy and
% X-ray microanalysis" Plenum Press, Ney York and London, 1987, p20
% 15/01/2000 A.P. Greeff
%
% RUTHERFORD2(Z,E,R) with
% Z=atomic number,
% E=electron energy (eV),
% R=random number

sigma=3.4*Z^(0.66)/E;
costheta=1-((2*R'*sigma)/(1+sigma-R));
f=acos(costheta)*180/pi;
```

D.3 Electron trajectory and energy loss calculations

D.3.1 `trajectory(total,starte,incidentangle,buf,halfmark)`

Refer to Section 4.7 on page 50.

This is the main program used to simulate the low energy electron trajectories in ZnO and ZnS using the Monte Carlo method. It is called from within the MATLAB command window and produces an output screen displayed in Figure D.3.1. The parameter `total` refers to the number of simulated electron trajectories, `starte` is the initial energy of the incident electrons expressed in eV, `incidentangle` refers to the angle of incidence between the electron beam and the surface of the solid, `buf` is the thickness of the diffusion interface between the start of the interface and the 50% mark, while `halfmark` refers to the depth at the 50% mark for the O profile. Both are expressed in units of *meter*. An example of a ZnO/ZnS concentration profile illustrating these two parameters is shown in Figure D.3.1. If the `incidentangle` parameter is set to 180, the angular distribution generated by `distribution.m` is used to generate the different incident angles for the electron beam.

The element's total elastic scattering cross sections and polar scattering angles as obtained from the NIST database is located in a file called `nist.mat`. The rest of the calculations concerning physical and mathematical aspects, like the elastic mean free path, the energy loss factor, etc. is performed using custom written MATLAB subroutines. Refer to the rest of this section for a listing and short description of each subroutine's source code.

Assigning the subroutine `trajectory.m` to a variable called, for example `data`, in the MATLAB command window an output screen similar to that in Figure D.3.1 is generated as well as a three dimensional matrix consisting of row, columns and pages. Each scattering event is an additional row in a matrix where the electron's xyz coordinates and energy is represented by separate columns and each electron's scattering information is then collected in a separate page of the matrix.

```
function mc=trajectory(total,starte,startbeta,buf,halfmark)

% TRAJECTORY.M Monte Carlo simulations for electron
% trajectories in %ZnO/ZnS. Uses DIFFINTERFACE.M to simulate
% the diffusion interface %between ZnO and ZnS
% 22/06/2000 A.P. Greeff
%
% TRAJECTORY(TOTAL,STARTE,INCIDNENTANGLE,BUF,HALFMARK) with
% TOTAL=total number of simulated electron trajectories
```

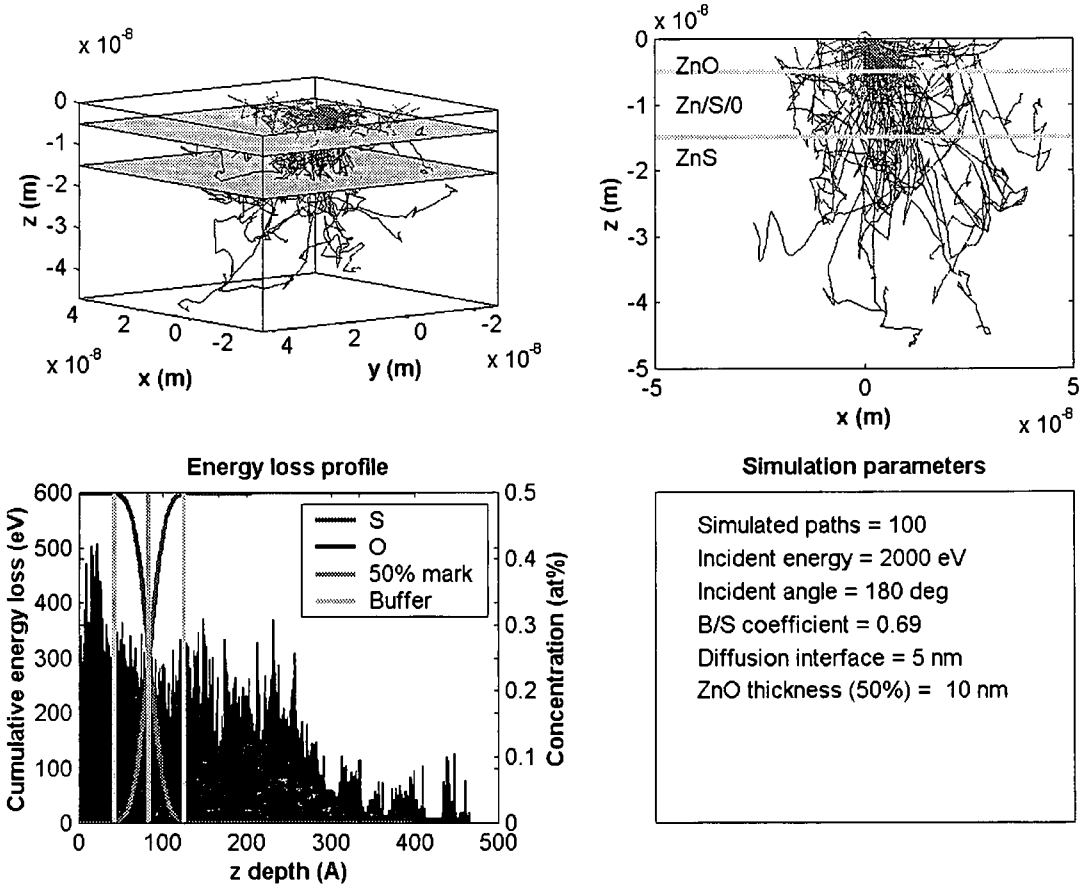

Figure D.2: **The output screen of the MATLAB function `trajectory.m` called from command window using the syntax: `trajectory(100,2000,180,5e-9,-10e-9)`. In this particular case 100 electron trajectories were simulated, each with an initial electron energy of 2 keV and the incident angles distributed according to the `distribution.m` subroutine. The thickness of the buffer layer was 5 nm and the depth of the 50% mark for the O profile is 10 nm. In the top part of the screen both three and two dimensional plots of the electron trajectories are shown. The volume between the two gray planes represent the diffusion interface consisting of Zn, S and O atoms of varying concentrations. The volume above the top plane only consists of only ZnO, while the volume below the bottom plane consists only of only ZnS. In the bottom left of the screen an energy loss profile is displayed with an overlayed concentration profile plot. This indicates the amount of energy loss in ZnO and ZnS. In the bottom right window an information panel shows the simulation parameters as well as the backscattering coefficient indicating the fraction of electron that exited the sample again.**

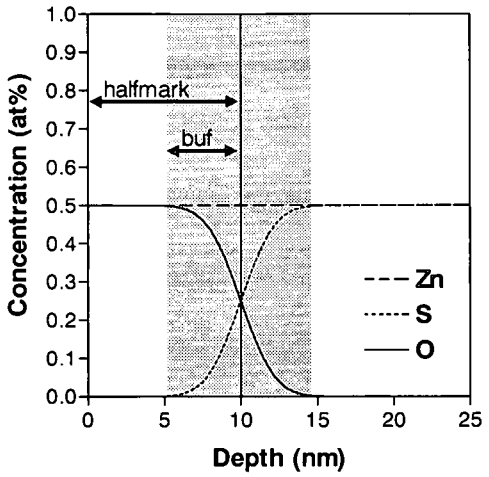

Figure D.3: A plot showing the concentration profile for a ZnO layer of certain thickness on top of ZnS. The parameter `halfmark` refers to the depth of the 50% mark for the O profile, while `buf` refers to the thickness of the diffusion interface between the start of the interface and the `halfmark` position. For this particular case `halfmark` has a value of 10 nm and `buf` a value of 5 nm.

```
% STRATE=initial beam energy in eV
% INCIDENTANGLE=beam incident angle (180 to use DISTRIBUTION.M)
% BUF=depth of diffusion interface
% HALFMARK=50% width of diffusion interface

data=[]; % Reset DATA matrix
backscatter=0; % Reset counter for backscsattered electrons
region=0; % Region = S concentration.

% Load data tabels for lookup
load nistdata.mat

% Material parameters [Zn S O]
z=[30 16 8]; % Atomic number
a=[63.57 32.064 15.999]; % Atomic weight (g/mol)
   rho=[7.14 2.07 1.14]; % Denisty (g/cm3)

for i=1:total % Loop for TOTAL electron trajectories

disp([i])

% Initial parameters
   R0=[0;0;0]; % Starting coordinate

   if startbeta == 180
      beta=distribution; % Sample incident angle from DISTRIBUTION.M
   else
      beta=startbeta; % Incident angle
```

```
   end

   gamma=0; % Rotation around x-axis
   e=starte; % Incident electron energy
   count=1; % Start counter for number of electron paths simulated
   data(count,1:3,i)=R0'; % Initialize DATA matrix with starting position
   data(count,4,i)=e; % Initialize DATA matrix with starting energy
   data(count,5,i)=region; % Initialize DATA matrix with starting region

% Get SIGMA from NIST database and pack into matrix
   sigma_zn=interp1(energydata_Zn(1,:),sigmadata_Zn,e);
   sigma_s=interp1(energydata_S(1,:),sigmadata_S,e);
   sigma_o=interp1(energydata_O(1,:),sigmadata_O,e);
   sigma=[sigma_zn sigma_s sigma_o];

% Distance travelled by electron prior to 1st collision
   f=diffinterface(buf,halfmark,0);
   s=-emfp(f,a,sigma,rho)*log(rand);
   e=e+deds(rho,f,z,e,a)*s;
   R=newposition(R0,s,0,0,0,beta,gamma);
   R0=R;
   count=2;
   data(count,1:3,i)=R';
   data(count,4,i)=e;
   data(count,5,i)=f(2);

% Begin loop
   count=3;
   while count >= 2

% Get SIGMA from NIST database and pack into matrix
   sigma_zn=interp1(energydata_Zn(1,:),sigmadata_Zn,e);
   sigma_s=interp1(energydata_S(1,:),sigmadata_S,e);
   sigma_o=interp1(energydata_O(1,:),sigmadata_O,e);
   sigma=[sigma_zn sigma_s sigma_o];

% Determine PHI scattering angle (deg)
   phi=round(360*rand);
% Determine concentration of Zn,S and O at depth Z
   f=diffinterface(buf,halfmark,R(3));
% Determine THETA angle from element responsible for scattering
   selecttheta=select1of3(f,sigma);
   if selecttheta==1
      theta=interp2(energydata_Zn,Rdata_Zn,thetadata_Zn,e,rand,'*linear');
   elseif selecttheta==2
      theta=interp2(energydata_S,Rdata_S,thetadata_S,e,rand,'*linear');
   elseif selecttheta==3
      theta=interp2(energydata_O,Rdata_O,thetadata_O,e,rand,'*linear');
   end

% Determine step length (m) and dE/dS
s=-emfp(f,a,sigma,rho)*log(rand);
bethe=deds(rho,f,z,e,a)*s;
% Calculate energy loss
if e+deds(rho,f,z,e,a)*s <= 50
      % 2nd last scattering event -> 50eV
```

```
      f=diffinterface(buf,halfmark,R(3));
      bethe=deds(rho,f,z,e,a);
      s=(50-e)/deds(rho,f,z,e,a);
      R=newposition(R0,s,theta,phi,0,beta,gamma);
      if R(3) > 0
         backscatter=backscatter+1;
         disp('Backscattered')
    break
      end
      beta=newbeta(R,R0);
      gamma=newgamma(R,R0);
      data(count,1:3,i)=R;
      data(count,4,i)=50;
      data(count,5,i)=region;
      count=count+1;
      R0=R;
      % last scattering event -> 0eV
      f=diffinterface(buf,halfmark,R(3));
      bethe=deds(rho,f,z,50,a);
      s=(0-50)/deds(rho,f,z,50,a);
      sigma_zn=interp1(energydata_Zn(1,:),sigmadata_Zn,50);
      sigma_s=interp1(energydata_S(1,:),sigmadata_S,50);
      sigma_o=interp1(energydata_O(1,:),sigmadata_O,50);
      sigma=[sigma_zn sigma_s sigma_o];

      selecttheta=select1of3(f,sigma);
if selecttheta==1
theta=interp2(energydata_Zn,Rdata_Zn,thetadata_Zn,e,rand,'*linear');
   elseif selecttheta==2
        theta=interp2(energydata_S,Rdata_S,thetadata_S,e,rand,'*linear');
   elseif selecttheta==3
       theta=interp2(energydata_O,Rdata_O,thetadata_O,e,rand,'*linear');
    end

      phi=round(360*rand);
      R=newposition(R0,s,theta,phi,0,beta,gamma);
      if R(3) > 0
         backscatter=backscatter+1;
         break
      end
      data(count,1:3,i)=R;
      data(count,4,i)=0;
      data(count,5,i)=f(2);
break
   else e=e+deds(rho,f,z,e,a)*s;
   end

% Calculate new R vector
R=newposition(R0,s,theta,phi,0,beta,gamma);
if R(3) > 0
      backscatter=backscatter+1;
      disp('Backscattered')
    break
   end

% Calculate new beta angle
```

```
beta=newbeta(R,R0);

% Calculate new gamma angle
gamma=newgamma(R,R0);

% Store data into DATA matrix at page(count)
data(count,1:3,i)=R;
   data(count,4,i)=e;
   data(count,5,i)=f(2);

% Reassign values for next loop
R0=R;
count=count+1;

end
end

disp(['Backscattering coefficient: ' num2str(backscatter/total)])
mc=data;


% Plot the trajectories in 3D
   subplot(2,2,1)
   trajectoryplot3D(data);
   layer3d(halfmark+buf)
   layer3d(halfmark-buf)
   view(-127.5,8)

% Plot the trajectory in 2D
   subplot(2,2,2)
   trajectoryplot2d(data);
   axisdata=axis;
   line_x=[axisdata(1) axisdata(1);axisdata(2) axisdata(2)];
   line_y=[halfmark-buf halfmark+buf;halfmark-buf halfmark+buf];
   plot(line_x,line_y,'y','LineWidth',2)
   text(axisdata(1)*.9,halfmark,'Zn/S/O')
   text(axisdata(1)*.9,(halfmark+buf)*0.8,'ZnO')
   text(axisdata(1)*.9,(halfmark-buf)*1.2,'ZnS')

% Determine the energy loss profile
subplot(2,2,3)
energylossplot(energylosscompute(data),buf,halfmark);

% Display information panel
   subplot(2,2,4)
   groupx=[0 0 1 1 0];
   groupy=[0 1 1 0 0];
   plot(groupx,groupy,'k')
   text(0.1,0.9,['Simulated paths = ',num2str(total)])
   text(0.1,0.8,['Incident energy = ',num2str(starte) ' eV'])
   text(0.1,0.7,['Incident angle = 'num2str(startbeta) ' deg'])
   text(0.1,0.6,['B/S coefficient = ',num2str(backscatter/total)])
   text(0.1,0.5,['Diffusion interface = 'num2str(buf*1e9) ' nm'])
   text(0.1,0.4,['ZnO thickness (50%) = 'num2str(halfmark*1e9) ' nm'])
   title(['Simulation parameters'])
   h=get(gca,'title');
```

```
set(h,'FontWeight','bold');
axis off

figure(1)
```

D.3.2 energyloss(total,starte,incidentangle,buf,halfmark)

Refer to Section 4.7 on page 50.

This program is similar to the main program `trajectory.m` except that the electron trajectories and energy loss profile are not displayed in an output screen, but the energy loss profile is saved to a native MATLAB data file called `eloss###.mat` where `###` is a number. All the parameters have the same meaning as in `trajectory.m`. To prevent `energyloss.m` overwriting the existing data file, the filename is truncated with the value of a counter stored in `status.mat`. The value of the counter is reset using `setstatus.m` with zero as an argument.

To obtain statistically significant energy loss profiles, 100 electron trajectories are not adequate. Increasing the amount of simulated electrons in the case of `trajectory.m` complicates the plotting of every single electron trajectory. It is therefore more convenient to use `energyloss.m` and increase the number of simulated electrons to 10^5 in order to obtain statistically significant results. Increasing the number of electron trajectories linearly increases the speed of program execution.

```
function energyloss(total,starte,incidentangle,buf,halfmark)
% ENERGYLOSS.M Calculate the energy loss profiles using the
% Monte Carlo method to simulate low energy electron trajectories
% 02/01/2001
%
% ENERGYLOSS(TOTAL,STARTE,INCIDNENTANGLE,BUF,HALFMARK) with
% TOTAL=total number of simulated electron trajectories
% STRATE=initial beam energy in eV
% INCIDENTANGLE=beam incident angle (180 to use DISTRIBUTION.M)
% BUF=depth of diffusion interface
% HALFMARK=50% width of diffusion interface

tic;

data=zeros(100,5); % Allocate memory vir DATA matrix
totaleloss=zeros(2000,1); % Allocate memory vir ELOSS matrix
backscatter=0; % Reset counter for backscattered electrons
region=0; % Reset region to S
perc=0; % Reset COMPLETE counter
```

```
% Material parameters [Zn S O]
z=[30 16 8]; % Atomic number
a=[63.57 32.064 15.999]; % Atomic weight (g/mol)
rho=[7.14 2.07 1.14]; % Density (g/cm3)
thetavector=[1 2 3]; % Index for polar scattering angle

% Load data tabels for lookup
load c:\matlabr11\toolbox\matlab\montecarlo\nistdata.mat Rdata_Zn energydata_Zn sigmadata_Zn thetadata_Z

fprintf(1,['  Copyright A.P. Greeff 2000 \n']);
fprintf(1,['  MONTE CARLO CALCULATION IN PROGRESS ... \n']);
fprintf(1,['  COMPLETE 0']);

for i=1:total % Loop for TOTAL electron trajectories

% Reset random generator to new state
rand('state',sum(100*clock));

% Display COMPLETE counter
perc=i/total*100;
if perc==10 | perc==20 | perc==30 | perc==40 | perc==50 | perc==60 | perc==70 | perc==80 | perc==90
fprintf(1,['>']);
elseif perc==100
fprintf(1,['100%%']);
fprintf(1,['\n']);
end

% Initial parameters
R0=[0;0;0]; % Starting coordinate
if incidentangle == 180
beta=distribution; % Use DISTRIBUTION.M
else
beta=incidentangle; % Use user specified value
end
gamma=0; % Rotation around x-axis
e=starte; % Incident electron energy
count=1; % Start counter for number of electron paths simulated
data(count,1:3)=R0'; % Initialize DATA matrix with starting position
data(count,4)=e; % Initialize DATA matrix with starting energy
data(count,5)=region; % Initialize DATA matrix with starting region

% Get SIGMA from NIST database and pack into matrix
sigma_zn=interp1(energydata_Zn(1,:),sigmadata_Zn,e,'*linear');
sigma_s=interp1(energydata_S(1,:),sigmadata_S,e,'*linear');
sigma_o=interp1(energydata_O(1,:),sigmadata_O,e,'*linear');
sigma=[sigma_zn sigma_s sigma_o];

% Distance travelled by electron prior to 1st collision
f=diffinterface(buf,halfmark,0);
s=-emfp(f,a,sigma,rho)*log(rand);
e=e+deds(rho,f,z,e,a)*s;
R=newposition(R0,s,0,0,0,beta,gamma);
R0=R;
count=2;
data(count,1:3)=R';
data(count,4)=e;
```

```
data(count,5)=f(2);

% Begin loop
count=3;
while count >= 2

% Reset random generator to new state
rand('state',sum(100*clock));

% Get SIGMA from NIST database and pack into matrix
sigma_zn=interp1(energydata_Zn(1,:),sigmadata_Zn,e,'*linear');
sigma_s=interp1(energydata_S(1,:),sigmadata_S,e,'*linear');
sigma_o=interp1(energydata_O(1,:),sigmadata_O,e,'*linear');
sigma=[sigma_zn sigma_s sigma_o];

% Determine PHI scattering angle (deg)
phi=round(360*rand);

% Determine concentration of Zn,S and O at depth Z
f=diffinterface(buf,halfmark,R(3));

% Determine THETA angle from element responsible for scattering
selecttheta=select1of3(f,sigma);
if selecttheta==1
theta=interp2(energydata_Zn,Rdata_Zn,thetadata_Zn,e,rand,'*linear');
elseif selecttheta==2
theta=interp2(energydata_S,Rdata_S,thetadata_S,e,rand,'*linear');
elseif selecttheta==3
theta=interp2(energydata_O,Rdata_O,thetadata_O,e,rand,'*linear');
end

% Determine step length (m) and dE/dS
s=-emfp(f,a,sigma,rho)*log(rand);
bethe=deds(rho,f,z,e,a)*s;

% Calculate energy loss
if e+deds(rho,f,z,e,a)*s <= 50
% 2nd last scattering event -> 50eV
f=diffinterface(buf,halfmark,R(3));
bethe=deds(rho,f,z,e,a);
s=(50-e)/deds(rho,f,z,e,a);
R=newposition(R0,s,theta,phi,0,beta,gamma);
if R(3) > 0
backscatter=backscatter+1;
break
end
beta=newbeta(R,R0);
gamma=newgamma(R,R0);
data(count,1:3)=R';
data(count,4)=50;
data(count,5)=region;
count=count+1;
R0=R;
% last scattering event -> 0eV
f=diffinterface(buf,halfmark,R(3));
bethe=deds(rho,f,z,50,a);
```

```
s=(0-50)/deds(rho,f,z,50,a);
% Get SIGMA from NIST database and pack into matrix
sigma_zn=interp1(energydata_Zn(1,:),sigmadata_Zn,50);
sigma_s=interp1(energydata_S(1,:),sigmadata_S,50);
sigma_o=interp1(energydata_O(1,:),sigmadata_O,50);
sigma=[sigma_zn sigma_s sigma_o];

selecttheta=select1of3(f,sigma);

if selecttheta==1
theta=interp2(energydata_Zn,Rdata_Zn,thetadata_Zn,e,rand,'*linear');
elseif selecttheta==2
theta=interp2(energydata_S,Rdata_S,thetadata_S,e,rand,'*linear');
elseif selecttheta==3
theta=interp2(energydata_O,Rdata_O,thetadata_O,e,rand,'*linear');
end

phi=round(360*rand);
R=newposition(R0,s,theta,phi,0,beta,gamma);
if R(3) > 0
backscatter=backscatter+1;
break
end
data(count,1:3)=R';
data(count,4)=0;
data(count,5)=f(2);
break
else e=e+deds(rho,f,z,e,a)*s;
end

% Calculate new R vector
R=newposition(R0,s,theta,phi,0,beta,gamma);
if R(3) > 0
backscatter=backscatter+1;
break
end

% Calculate new beta angle
beta=newbeta(R,R0);

% Calculate new gamma angle
gamma=newgamma(R,R0);

% Store data into DATA matrix at page(count)
data(count,1:3)=R';
data(count,4)=e;
data(count,5)=f(2);

% Reassign values for next loop
R0=R;
count=count+1;

end

% Calculate energy loss for one datapage
thiseloss=energylosscompute(data);
```

```
% Pad THISELOSS with zeros up to 2000 elements
thiseloss(size(thiseloss,1)+1:2000)=0;
totaleloss=totaleloss+thiseloss;
data=zeros(100,5); % Clear

end

BS=backscatter/total;

% Write ELOSS###.MAT data file
load('status.mat','status')
status=status+1;
filename=['eloss' num2str(status) '.mat'];
save(filename,'totaleloss','BS','total','starte','incidentangle','buf','halfmark')
save('status.mat','status')
fprintf(1,['  Data saved to ELOSS' num2str(status) '.MAT \n']);


t=toc;
fprintf(1,['  Computation time: ' num2str(t) ' seconds \n']);
```

D.3.3 mip(Z)

Refer to Section 4.4 on page 45.

This is one of the subroutines of the main programs `trajectory.m` and `energyloss.m` and calculates the mean ionization potential. This is a measure of the average energy loss per interaction considering all possible energy loss processes. The parameter Z is a vector containing the atomic numbers of the Zn, S and O atoms.

```
function f=mip(Z)
% MIP.M Calculate mean ionization potential in eV using Berger-Selzer formula
% From: D.E. Newbury et al. in "Advanced scanning electron microscopy and X-ray microanalysis"
% Plenum Press, Ney York and London, 1987, p15
% 15/01/2000 A.P. Greeff
%
% MIP(Z) with
% Z=atomic number

f=(9.76.*Z+58.5.*Z.^-.19);

for i=1:size(Z,2)
   if Z(i) <= 12
      f(i)=11.5*Z(i);
   end
end
```

D.3.4 emfp(F,A,sigma,rho)

Refer to Section 4.3 on page 42.

This is a subroutine of the main programs `trajectory.m` and `energyloss.m` and calculates the elastic mean free path of electrons in the solid. The parameter `F` is a vector containing the Zn, S and O concentration expressed as a fraction, `A` is a vector containing the atomic masses in *g/mol*, `sigma` a vector containing the total elastic scattering cross sections in m^2 and `rho` a vector containing the densities of Zn, S and O in g/cm^3.

```
function f=emfp(F,A,sigma,rho)
% EMFP.M Calculate electron mean free path in m
% From: P. Hovington et al. Scanning 19, pp1-14 (1997) and D.E. Newbury in
% "Advanced scanning electron microscopy and X-ray microanalysis"
% Plenum Press, Ney York and London, 1987, p4
% 28/07/2000 A.P. Greeff
%
% EMFP(F,A,sigma,rho) with
% F=atomic fraction,
% A=atomic mass (g/mol),
% sigma=total cross section (m^2),
% rho=density (g/cm^3)

C=(F./A)/sum(F./A); % Convert form at% to wt%
f=(1e-6/6.023e23)*((C*A')/(F*rho'))/(F*sigma');
```

D.3.5 diffinterface(buf,halfmark,zdepth)

Refer to Section 4.5 on page 47.

This is a subroutine of the main programs `trajectory.m` and `energyloss.m` and returns the atomic concentration of Zn, S and O at a particular depth. The parameter `buf` is the thickness of the diffusion interface between the start of the interface and the 50% mark of the O profile and `halfmark` refers to depth of the 50% mark of the O profile. All the parameters are expressed in units of meters. See Figure D.3.1 on page 122 for an illustration of these parameters.

```
function f=diffinterface(buf,halfmark,zdepth)
% DIFFINTERFACE.M Simulate a diffusion interface between ZnO layer
% and ZnS bulk using error function.
% 22/06/2000 A.P. Greeff
%
% [F_Zn F_S F_O]=DIFFINTERFACE(buf,halfmark,zdepth) with
```

```
% buf=diffusion interface thickness (m),
% halfmark=ZnO thickness (50%) (m),
% zdepth=Given ZnO depth (m)
% Important: HALFMARK and ZDEPTH is negative, do not set BUF=0

f_Zn=0.5;
f_S=(erf((-zdepth*1e9+b*1e9)/(a*1e9/2))+1)/4;
f_O=0.5-f_S;
f=[f_Zn f_S f_O];
```

D.3.6 select1of3(F,sigma,theta)

Refer to Section 4.5 on page 47.

This is a subroutine of the main programs `trajectory.m` and `energyloss.m` and selects the atom, either Zn, S or O, that is responsible for the electron scattering event. The result of the selection is returned as the row index of the vector F. For example, if the Zn atom is responsible for the scattering `select1of3.m` will return a value of 1.

The selection is based upon each atom's elemental contribution towards the total elastic scattering cross section as well as the concentration of each element. The parameter F is a vector containing the Zn, S and O concentration expressed as a fraction, sigma is a vector containing the total elastic scattering cross sections of the three elements in m^2.

```
function f=select1of3(F,sigma)
% SELECT1OF3.M Select 1 of 3 possible vector elements contributing to
% scattering according to it's elemental contribution to the compound's
% total elastic scattering cross section
% 20/7/2000 A.P. Greeff
%
% SELECT1OF3(F,sigma) with
% F=concentration,
% sigma=total elastic scattering cross section vector (m^2),

index=[1 2 3];
R=rand;
setpoint1=(F(1)*sigma(1))/(F*sigma');
setpoint2=(F(1:2)*sigma(1:2)')/(F*sigma');

if 0 <= R & R <= setpoint1
   f=index(1);
elseif setpoint1 <= R & R <= setpoint2
   f=index(2);
elseif setpoint2 <= R & R <= 1
   f=index(3);
else
   f=NaN;
end
```

D.3.7 newposition(R0,S,theta,phi,alpha,beta,gamma)

Refer to Section C.1 on page 105.

This is one of the subroutines of the main programs `trajectory.m` and `energyloss.m` and calculates the end coordinates of the scattering vector given the initial coordinates, polar and azimuthal scattering angles as well as the three rotational angles. The parameter R0 is the initial xyz coordinates, S is the step length, `theta` and `phi` is the polar and azimuthal scattering angles, while `alpha`, `beta` and `gamma` is the three rotational angles.

```
function f=newposition(r0,s,theta,phi,alpha,beta,gamma)
% NEWPOSITION.M Translate from spherical to "laboratory" cartesian coordinates
% 21/11/1999 A.P. Greeff
%
% NEWPOSITION(r0,s,theta,phi,alpha,beta,gamma) with
% r0=row vector containing intial coordinates
% s=step length
% theta=polar scattering angle
% phi=azimuthal scattering angle
% alpha=rotational angle
% beta=rotational angle, calculate with newbeta.m
% gamma=rotational angle, calculate with newgamma.m

% Convert degree angles to radians
rad=360/(2*pi);
theta=theta/rad;
phi=phi/rad;
alpha=alpha/rad;
beta=beta/rad;
gamma=gamma/rad;

% Set up X,Y,Z rotation matrix
Xrot=[1 0 0;0 cos(alpha) sin(alpha);0 -sin(alpha) cos(alpha)];
Yrot=[cos(beta) 0 -sin(beta);0 1 0;sin(beta) 0 cos(beta)];
Zrot=[cos(gamma) -sin(gamma) 0;sin(gamma) cos(gamma) 0;0 0 1];

% Set up speherical to cartesian transformation
SPH=[sin(theta)*cos(phi);sin(theta)*sin(phi);-cos(theta)];

%Calculate new position
f=r0+s*Zrot*Yrot*Xrot*SPH;
```

D.3.8 newbeta(R,R0)

Refer to Section C.2 on page 107.

This is one of the subroutines of the main programs `trajectory.m` and `energyloss.m` that

calculates one of the rotational angles used to project the coordinates in the electron's reference frame onto the "laboratory" reference frame. The parameters R and R0 is the final and initial xyz coordinates for a scattering event in units of meter.

```
function f=newbeta(R,R0)
% NEWBETA Calculate new beta rotarion angle in degrees
% 17/01/2000 A.P. Greeff
%
% NEWBETA(R,R0) with
% R=new position,
% R0=old position

a=R-R0;
f=round(acos(-a(3)/sqrt(a(1)^2+a(2)^2+a(3)^2))*180/pi);
```

D.3.9 newgamma(R,R0)

Refer to Section C.2 on page 107.

This is subroutine of the main programs `trajectory.m` and `energyloss.m` and calculates the other rotational angle used to project coordinates in the electron's reference frame onto the "laboratory" reference frame. The parameters R and R0 is the final and initial xyz coordinates for a scattering event in units of meter.

```
function f=newgamma(R,R0)
% NEWGAMMA Calculate new gamma rotation angle in degrees
% 17/01/2000 A.P. Greeff
%
% NEWGAMMA(R,R0) with
% R=newposition,
% R0=old position

a=R-R0;
projxy=[1 0 0;0 1 0;0 0 0]; %From xy-projection matrix
a=projxy*a; %Project a vector onto xy plane
f=round(acos(a(1)/sqrt(a(1)^2+a(2)^2+a(3)^2))*180/pi);
if a(2) <= 0
   f=360-f;
end
```

D.3.10 energylosscompute(data)

Refer to Section 4.8 on page 52.

This is one of the subroutines of the main programs `trajectory.m` and `energyloss.m` and computes the cumulative energy loss of the electrons in the solid during the Monte Carlo simulation. The parameter data refers to a matrix containing the coordinates of each scattering event as well as the electron energy at each of these events. This matrix is generated by assigning it to `trajectory.m`.

```
function f=energylosscompute(data)
% ENERGYLOSSCOMPUTE.M Determine energy loss in layers each 1A thick
% from matrix called DATA.
% 31/05/2000 A.P. Greeff
%
% ENERGYLOSSCOMPUTE(data) with
% data=data matrix generated by TRAJECTORY.M

% Determine the maximum Z depth
zmin=0;
for i=1:size(data,3)
   if min(data(:,3,i)) < zmin
      zmin=min(data(:,3,i));
   end
end
energydata=zeros(round(-zmin*1e10)+10,1);

% Sorting loop for pages of DATA
for i=1:size(data,3)

   datapage=stripzeros(data(:,:,i));

   diffenergy=diff(datapage(:,4));
   diffzpos=diff(datapage(:,3)*1e10);
   for k=1:size(diffzpos,1)
      if diffzpos(k)==0
         diffzpos(k)=1;
      end
   end
   eloss=diffenergy./diffzpos;

   start=1;

% Sorting loop for columns of DATA
for j=1:size(datapage,1)-1

   tempenergydata=zeros(round(-zmin*1e10)+10,1);

   start;
   stop=start+round(-diffzpos(j,:));
   if stop <= 0
      stop=1;
   end


   % electron downwards
   if eloss(j,:) > 0
      tempenergydata(start:stop)=eloss(j,:);
```

```
   % electron upwards
   elseif eloss(j,:) < 0
      tempenergydata(stop:start)=-eloss(j,:);
   elseif eloss(j,:) == 0
      break
   end

   if j ~= size(datapage,1)-1 | j ~= 1
      if eloss(j,:) > 0
    tempenergydata(stop)=0;
      elseif eloss(j,:) < 0
         tempenergydata(start)=0;
      end
   end
   energydata=energydata+tempenergydata;

   if stop <=0
      stop
      disp('You are here')
      start=1
   else
      start=stop;
   end
end
end

f=energydata;
```

D.3.11 distribution

Refer to Section 3.7 on page 35.

This is a subroutine of the main programs and calculates the electron's initial incident angle from a probability density function. The function is solved using the numerical Newton-Rhapson iteration method. The density function was determined using the results obtained from the source code listed in Section D.1.1 on page 114.

```
function f=distribution
% DISTRIBUTION.M Distribute electron beam incident angles between 0 and
% 90 degrees according to prob. density function f(t)=0.044sin(2t)+0.00278
% using the Monte Carlo technique. Value for t is determined numerically using
% Newton-Rhapson method from: Burden and Faires in "Numerical
% analysis" 5th edition PWS Publishing Company, Boston (1993) p 56
% 10/05/2000 A.P. Greeff
%
% DISTRIBUTION with no argument

a=0.044;
b=0.0278;
t0=pi/4;
```

```
P=rand;
if P == 1
   P=0.999
end

for i=1:10


F=(cos(2*t0)-2*b*t0/a-1+(2+b*pi/a)*P)/(-2*sin(2*t0)-2*b/a);
t=t0-F;

  if abs(t-t0) < 0.001
     break
  end

t0=t;

end

if i == 10
   disp('Method failed')
end

f=t*180/pi;
```

D.3.12 trajectoryplot3d(data)

This is a subroutine of the main programs `trajectory.m` and is used to plot the electron trajectories from information contained in the matrix called `data` in a three dimensional view. An example can be seen in the top left corner of the output screen of `trajectory.m` in Figure D.3.1 on page 121. The subroutine can also be called from the MATLAB command window as a stand alone routine.

```
function f=trajectoryplot3D(data)
% TRAJECTORYPLOT3D.M Plot electorn trajectories in 3D using matrix
% generated by TRAJECTORY.M
% 31/05/2000 A.P. Greeff
%
% TRAJECTORYPLOT3D(data) with
% data=data matrix generated by TRAJECTORY.M

for i=1:size(data,3);
   datapage=stripzeros(data(:,:,i));
   X=datapage(:,1);
   Y=datapage(:,2);
   Z=datapage(:,3);
   region=datapage(:,5);

   if datapage(size(datapage,1),4)==0
      plot3(X,Y,Z,'b')
```

```
      hold on
   else
      plot3(X,Y,Z,'r')
      hold on
   end

   for i=1:size(datapage,1)
    if region(i)==1
       plot3(X(i),Y(i),Z(i),'g.')
    end
   end

end

box on
xlabel('x (m)')
h=get(gca,'xlabel');
set(h,'FontWeight','bold');
ylabel('y (m)')
h=get(gca,'ylabel');
set(h,'FontWeight','bold');
zlabel('z (m)')
h=get(gca,'zlabel');
set(h,'FontWeight','bold');
axis equal
rotate3d on
```

D.3.13 layer3d(z)

This is a subroutine of the main program `trajectory.m` and is used to add a plane at a depth specified by the parameter z given in units of meter. An example can be seen in top left corner of the output screen of `trajectory.m` in Figure D.3.1 on page 121 where `layer3d.m` is used to indicate the upper and lower regions of the diffusion interface.

```
function f=layer3d(z)
% LAYER3D.M Use patch.m to indicate a surface or interface layer
% 01/06/2000 A.P. Greeff
%
% LAYER3D(z) with
% z=depth (m)
% Important: z is negative

axisdata=axis;
Xpatchdata=[axisdata(1);axisdata(1);axisdata(2);axisdata(2)];
Ypatchdata=[axisdata(3);axisdata(4);axisdata(4);axisdata(3)];
Zpatchdata=[z;z;z;z];
patch(Xpatchdata,Ypatchdata,Zpatchdata,'y')
```

D.3.14 energylossplot(data,buf,halfmark)

This is a subroutine of the main program `trajectory.m` and plots the energyloss profile computed by the subroutine `energylosscompute.m` from the matrix called `data`. Overlayed with this is a plot of the concentration profile determined by the parameters `buf` and `halfmark`. An example can be seen in the bottom left corner of the output screen of `trajectory.m` in Figure D.3.1 on page 121. Overlaying the two plots gives an indication of the amount of energy lost in each of the regions.

```
function f=energylossplot(data,buf,halfmark)
% ENERGYLOSSPLOT.M Plot the energy loss profile computed by ENERGYLOSSCOMPUTE.M
% 01/06/2000 A.P. Greeff
%
% ENERGYLOSSPLOT(data,buf,halfmark) with
% data=energy loss profile generated by ENERGYLOSSCOMPUTE.M,
% buf=diffusion interface thickness (m),
% halfmark=ZnO thickness (50%) (m),

bar(data,'k')
hold on
axisdata=axis;
xlabel('z depth (A)')
h=get(gca,'xlabel');
set(h,'FontWeight','bold');
ylabel('Cumulative energy loss (eV)')
h=get(gca,'ylabel');
set(h,'FontWeight','bold');
title('Energy loss profile')
h=get(gca,'title');
set(h,'FontWeight','bold');

x=0:size(data,1);

c_S=(erf((x*1e-1+halfmark*1e9)/(buf*1e9/2))+1)/4;
c_O=0.5-(erf((x*1e-1+halfmark*1e9)/(buf*1e9/2))+1)/4;

h1=gca;
h2=axes('Position',get(h1,'Position'));
plot(x,c_S,'r','LineWidth',2)
hold on
plot(x,c_O,'b','LineWidth',2)
ylabel('Concentration (at%)')
h=get(gca,'ylabel');
set(h,'FontWeight','bold');
b_x=[-halfmark -halfmark]*1e10;
b_y=[0 0.5];
plot(b_x,b_y,'g','LineWidth',2)
a_x=[-halfmark-buf -halfmark+buf;-halfmark-buf -halfmark+buf]*1e10;
a_y=[0 0; 0.5 0.5];
plot(a_x,a_y,'y','LineWidth',2)
legend('S','O','50% mark','Buffer')
```

```
set(h2,'YAxisLocation','right','Color','none','XTickLabel',[])
set(h2,'XLim',get(h1,'XLim'),'Layer','top')
```

D.3.15 stripzeros(A)

This is one of the subroutines of the main programs that removes the zeros in the data matrix generated by `trajectory.m`. The parameter `A` refers to a matrix containing the coordinates of each scattering event as well as the electron energy at each of these events.

```
function f=stripzeros(A)
% STRIPZEROS.M Remove end zeros in matrix generated by TRAJECTORY.M
% 23/05/2000 A.P. Greeff
%
% STRIPZEROS(data) with
% data=data matrix generated by TRAJECTORY.M

rows=size(A,1);

for i=1:rows
   if A(i,1)+A(i,2)+A(i,3)+A(i,4)==0
      A=A(1:i-1,:);
      break
   end
end

f=A;
```

D.4 Cathodoluminescence calculations

D.4.1 cl(elossfile,correction)

Refer to Section 5.6 on page 71.

This source code calculates the relative cathodoluminescence generated during the energy loss of electrons moving through a solid. The parameter `elossfile` refers to a file generated by the program `energyloss.m` that contains the energy loss profile and other parameters used during the Monte Carlo simulation of the electron trajectories. The parameter `correction` can be set to zero if the ZnS in the diffusion interface is luminescent, else a value of 1 assumes that the material in the interface is non-luminescent.

```
function f=cl(filename)
global totaleloss
```

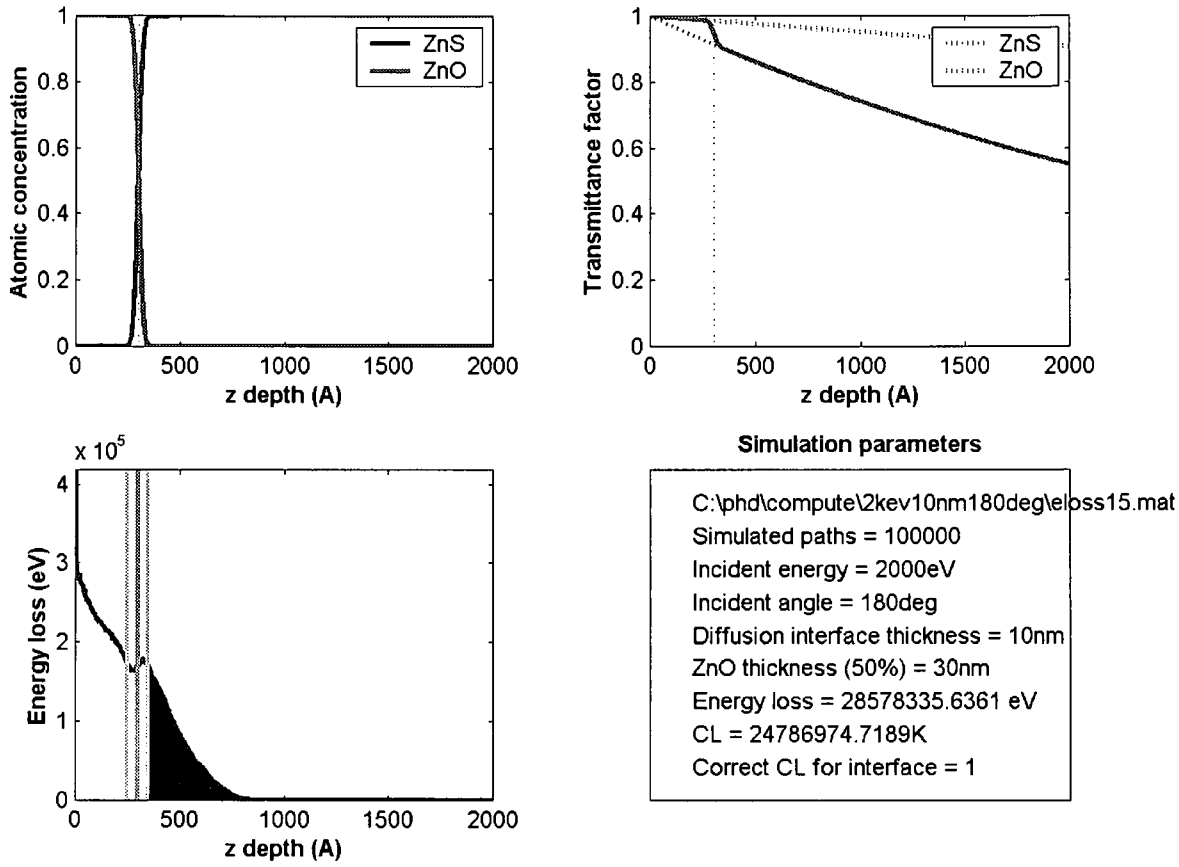

Figure D.4: **The output screen of the MATLAB function `cl.m` called from within the command window using the following syntax: `cl('eloss15.mat',1)`. In this case the data file containing the previously calculated energy loss profile is eloss15.mat while the parameter "1" indicates that if was assumed that the diffusion interface is non-luminescent. In the top left of the screen a ZnO/ZnS concentration profile is shown for a 30 nm thick ZnO layer and a 10 nm wide diffusion interface. The simulation parameters were obtained from the file eloss15.mat. In the top right window the photon transmittance profile for ZnO and ZnS is shown. The solid line represents the combined transmittance profile according to the ZnO/ZnS concentration profile. Applying the ZnS concentration profile to the energy loss profile shown, eliminates that part of the profile representing energy loss in the ZnO region and diffusion interface. The remainder of the profile is represented by the shaded area. In the bottom right window the simulation parameters is displayed along with the calculated cathodoluminescence intensity.**

```
% CL.M Calculate the generated CL using data in the ELOSS###.MAT file
% 13/09/2000 A.P. Greeff
%
% CL('filename') with
% filename=name of MATLAB data file

loadfile=['load ' filename];
eval(loadfile)

% Parameters:
alpha_ZnO=2e-4; % Absorption coefficient in ZnO (A-1)
alpha_ZnS=4e-4; % Absorption coefficient in ZnS (A-1)

% Calculate concentration profile for ZnO and ZnS
for i=1:2000
F(i,1:3)=diffinterface(buf,halfmark,-i*1e-10);
end
F_ZnS=F(:,2)*2;
F_ZnO=F(:,3)*2;
clf
subplot(2,2,1)
plot(F_ZnS,'b','LineWidth',2)
hold on
plot(F_ZnO,'r','LineWidth',2)
X=[-halfmark*1e10 -halfmark*1e10];
Y=[0 1];
plot(X,Y,'g','LineWidth',2)
xlabel('z depth (A)')
h=get(gca,'xlabel');
set(h,'FontWeight','bold');
ylabel('Atomic concentration')
h=get(gca,'ylabel');
set(h,'FontWeight','bold');
legend('ZnS','ZnO')

% Calculate the absorption
z=1:2000;
abs_ZnO=exp(-alpha_ZnO*z);
abs_ZnS=exp(-alpha_ZnS*z);
abs_total=F_ZnO.*abs_ZnO'+F_ZnS.*abs_ZnS';
subplot(2,2,2)
plot(abs_ZnS,'b:','LineWidth',2)
hold on
plot(abs_ZnO,'r:','LineWidth',2)
plot(abs_total,'m','LineWidth',2)
X=[-halfmark*1e10 -halfmark*1e10];
Y=[0 1];
plot(X,Y,'g','LineWidth',2)
xlabel('z depth (A)')
h=get(gca,'xlabel');
set(h,'FontWeight','bold');
ylabel('Absorption coefficient')
h=get(gca,'ylabel');
set(h,'FontWeight','bold');
legend('ZnS','ZnO')
```

```
% Calculate the generation
generation=totaleloss.*F_ZnS;
subplot(2,2,3)
plot(totaleloss,'b','LineWidth',2)
hold on
bar(generation,'g')
X=[-halfmark*1e10 -halfmark*1e10];
Y=[0 max(totaleloss)];
axis([0 2000 0 max(totaleloss)])
plot(X,Y,'g','LineWidth',2)
xlabel('z depth (A)')
h=get(gca,'xlabel');
set(h,'FontWeight','bold');
ylabel('Energy loss (eV)')
h=get(gca,'ylabel');
set(h,'FontWeight','bold');

% Calculate CL intensity
CL=generation'*abs_total;

% Plot information
subplot(2,2,4)
groupx=[0 0 1 1 0];
groupy=[0 1 1 0 0];
plot(groupx,groupy,'k')
text(0.1,0.9,['Data file = ' filename])
text(0.1,0.8,[cd])
text(0.1,0.7,['Simulated paths = ' num2str(total)])
text(0.1,0.6,['Incident energy = ' num2str(starte) 'eV'])
text(0.1,0.5,['Incident angle = ' num2str(incidentangle),'deg'])
text(0.1,0.4,['Diffusion interface = ' num2str(buf*1e9) 'nm'])
text(0.1,0.3,['ZnO thickness (50%)w = ' num2str(-halfmark*1e9) 'nm'])
%text(0.1,0.2,['CL n.a. = ' num2str(sum(generation)) 'K'])
text(0.1,0.2,['CL = ' num2str(CL) 'K'])
axis off
title('Simulation parameters')
h=get(gca,'title');
set(h,'FontWeight','bold');


disp('Saving F_ZnS to FZnS.dat ...')
outputfile=[z'/10 F_ZnS];
save 'FZnS.dat' outputfile -ascii

disp('Saving F_ZnO to FZnO.dat ...')
outputfile=[z'/10 F_ZnO];
save 'FZnO.dat' outputfile -ascii

disp('Saving A_ZnS to AZnS.dat ...')
outputfile=[z'/10 abs_ZnS'];
save 'AZnS.dat' outputfile -ascii

disp('Saving A_ZnO to AZnO.dat ...')
outputfile=[z'/10 abs_ZnO'];
save 'AZnO.dat' outputfile -ascii
```

```
disp('Saving A_total to ATotal.dat ...')
outputfile=[z'/10 abs_total];
save 'ATotal.dat' outputfile -ascii

disp('Saving ELOSS to ELOSS.DAT ...')
outputfile=[z'/10 totaleloss];
save 'eloss.dat' outputfile -ascii

disp('Saving G to G.dat ...')
outputfile=[z'/10 generation];
save 'G.dat' outputfile -ascii

disp('Saving CL to CL.dat ...')
save 'CL.dat' CL -ascii



f=[num2str(CL) 'K'];
```

Bibliography

[1] Office of the Under Secretary of Defense for Acquisition and Technology, The Acquisition of Flat Panel Displays for Military Applications, March 1998, p18. (http://www.acq.osd.mil/es/fpd/fpd.pdf)

[2] Electroluminescent Technology, Planar System Inc. March 1999 (http://www.planar.com/Website/Main.nsf/Pages/KM1021)

[3] Electroluminescent Displays, Planar System Inc. March 1999 (http://www.planar.com/Website/docs.nsf/Pages/KM1063)

[4] Candescent Technologies Corporation, Technology Primer, December 1999 (http://www.candescent.com/Candescent/techprim.htm)

[5] FED construction, Futuba Europe January 2000 (http://www.futaba-eu.com/docs/fed-construction.htm)

[6] How FED's work, PixTech Inc., April 1999 (http://www.pixtech.com/howfeds.htm)

[7] P.H. Holloway, J. Sebastian, T.A. Trottier, H.C. Swart, Solid State Technol. 38 (1995) 47.

[8] H.C. Swart, J.S. Sebastian, T.A. Trottier, S.L. Jones, P.H. Holloway, J. Vac. Sci. Technol. A 14 (1996) 1697.

[9] L. Oosthuizen, H.C. Swart, P.E. Viljoen, P.H. Holloway and G.L.P. Berning, Appl. Surf. Sci. 120 (1997) 9.

[10] P.H. Holloway, T.A. Trottier, B. Abrams, C.K. Kondoleon, S.Jones, J.S. Sebastian, W.J. Thomes, J. Vac. Sci. Technol. 17 (1999) 758.

[11] P.H. Holloway, T.A. Trottier, J.S. Sebastian, S.L. Jones, X.-M. Zhang, J.-S. Bang, B. Abrams, W.J. Thomes and T.-J. Kim, J. Appl. Phys. 88 (2000) 483.

[12] B.L. Abrams, W. Roos, P.H. Holloway and H.C. Swart, Surf. Sci. 451 (2000) 174.

[13] S. Itoh, T. Kimizuka and T. Tanegawa, J. Electrochem. Soc. 136 (1989) 1819.

[14] T.A. Trottier, Ph.D. thesis, University of Florida, 1997.

[15] H.C. Swart, A.P. Greeff, P.H. Holloway, G.L.P. Berning, Appl. Surf. Sci. (1999) 63.

[16] J.D. Kingsley, J.S. Prener, J. Appl. Phys. 43 (1972) 3073.

[17] M. Toth and M.R. Phillips, Scanning 20 (1998) 425.

[18] The CASINO page, July 1999 (www.gme.usherb.ca/casino/index.html)

[19] P. Hovington, D. Drouin, R. Gauvin, Scanning 19 (1997) 1.

[20] D. Drouin, P. Hovington, R. Gauvin, Scanning 19 (1997) 20.

[21] P. Hovington, D. Drouin, R. Gauvin, Scanning 19 (1997) 29.

[22] J.C.H. Phang, K.L. Pey and D.S.G. Chan, IEEE Transactions on Electron Devices 39 (1992) 782.

[23] F.-L. Zhang, Y.-D. Jiang, S. Yang, J. Penczek, B.K. Wagner, Z.-L. Wang and C.J. Summers, Technical Digest of IVMC'97 Korea (1997) 266.

[24] T.E. Everhart and P.H. Holf, J. Appl. Phys. 42 (1971) 5837.

[25] H.C. Swart, L. Oosthuizen, P.H. Holloway, G.L.P. Berning, Surf. Int. Anal. 26 (1998) 337.

[26] H.C. Swart and K.T. Hillie, Surf. Int. Anal. 30 (2000) 383.

[27] R.L. Burden and J.D. Faires, Numerical Analysis, 5th edition (PWS Publishing Company, Boston, 1993) p.56.

[28] R. Shimizu and Z.-J. Ding, Rep. Prog. in Physics 55 (1992) 487.

[29] L. Reimer and D. Stelter, Scanning 8 (1986) 265.

[30] P.G.T. Howell and A. Boyde, Scanning 20 (1998) 45.

[31] A.P. Greeff and H.C. Swart, Surf. Int. Anal. 29 (2000) 807.

[32] F.W. Sears and G.L. Salinger, Thermodynamics, Kinetic Theory, and Statistical Thermodynamics, 3rd edition (Addison-Wesley Publishing Company, London, 1986) p.281.

[33] D.E. Newbury, D.C. Joy, P. Echlin, C.E. Fiori and J.I. Goldstein, Advanced Scanning Electron Microscopy and X-Ray Microanalysis, 1st edition (Plenum Press, New York, 1986) p.4.

[34] Z.-J. Ding and R. Shimizu, Scanning 18 (1996) 92.

[35] NIST Elastic Electron Scattering Cross Section Database, Standard Reference Data Program, Database 64. National Institute of Standards and Technology, Standard Reference Data Program, Gaithersburg (1996). www.nist.gov/srd/.

[36] Z.-J. Ding and R. Shimizu, Surf. Sci. 197 (1998) 539.

[37] R. Shimizu and S. Ichimura, Toyota Foundation Research Report No. I-006, Toyota Foundation, Tokyo (1981).

[38] D. C. Joy and S. Luo, Scanning 11 (1989) 176.

[39] M.J. Berger and S.M. Seltzer, Studies in Penetration of Charged Particles in Matter, Nuclear Science Series Report No. 39, NAS-NRC Publication No 1133 (National Academy of Science, Washington DC, 1964) p.205.

[40] C.J. Tung, J.C. Ashley and R.H. Ritchie, Surf. Sci. 427 (1979) 427.

[41] T.S. Rao-Sahib and D.B. Wittry, J. Appl. Phys 45 (1974) 5060.

[42] D.C. Joy, S. Luo, R. Gauvin, P. Hovington and N. Evans, Scanning Microscopy 10 (1996) 653.

[43] D.R. Askeland, The Science and Engineering of Materials, 3rd SI edition (Chapman and Hall, London, 1996) p.265.

[44] P.G. Shewmon, Diffusion in Solids (McGraw-Hill Book Company, New York, 1963) p.5.

[45] R. Browning, T. Eimori, E.P. Traut, B. Chui and F.W. Pease, J. Vac. Sci. Technol. B 9 (1991) 3578.

[46] U. Werner, F. Koch and G. Oelgart, J. Phys. D:Appl. Phys. 21 (1988) 116.

[47] K.L. Pey, D.S.H. Chan and J.C.H. Phang, Scanning Microscopy 9 (1995) 355.

[48] S. Myhajlenko, Luminescence of solids, 1st edition, Ed. D.R. Vij (Plenum Press, New York, 1998) p.135.

[49] J.B. Steyn, P. Giles and D.B. Holt, J. Microsc. 107 (1976) 107.

[50] Z. Czyzewski and D.C. Joy, Scanning 12 (1990) 5.

[51] W. Park, T.C. Jones, S Schön, W. Tong, M. Chaichimansour, B.K. Wagner and C.J. Summers, J. Crystal Growth 184 (1998) 1123.

[52] S.M. Davidson, J. Microsc. 110 (1977) 177.

[53] A.P. Greeff and H.C. Swart, Surf. Int. Anal. 31 (2001) 448-456.

[54] G. Pfefferkorn, W. Brocker and M. Hastenrath, Scan. Electron. Microsc. 251 (1980) 251.

[55] A. Velentini, A. Quirini and L. Vasanelli, Thin Solid Films 176 (1989) L167-L171.

[56] M. Jin and L.S. Ying, Thin Solid Films 237 (1994) 16.

[57] V. Craciun, J. Elders, J.G.E. Gardeniers and I.W. Boyd, Appl. Phys. Lett. 65 (1994) 2963.

[58] K.L. Narasimhan, S.P. Pai, V.R. Palkar and R. Pinto, Thin Solid Films 295 (1997) 104.

[59] E.M. Bachari, G. Baud, S. Ben Amor and M. Jacquet, Thin Solid Films 348 (1999) 165.

[60] M. Matsuoka and K. Ono, J. Vac. Sci. Technol. A 7 (1989) 2975.

[61] M. Dinescu and P. Verandi, Appl. Surf. Sci. 106 (1996) 146.

[62] M. Krunks and E. Mellikov, Thin Solid Films 270 (1995) 33.

[63] G.J. Exarhos and S.K. Sharma, Thin Solid Films 270 (1995) 27.

[64] B.S. Farag and S.A. Khodier, Thin Solid Films 201 (1991) 231.

[65] D.W. Tenquist, R.M. Whittle and J. Yarwood, in University Optics Volume 2 (Gordon and Breach Science Publishers, New York 1970) p.227.

[66] A. Ashour, H.H. Afifi and S.A. Mahmoud, Thin Solid Films 248 (1994) 253.

[67] T. Maruyama and T. Kawaguchi, Thin Solid Films 188 (1990) 323-327.

[68] F.-L. Zhang, S. Yang, C. Stoffers, J. Penczek, P.N. Yocom, D. Zaremba, B.K. Wagner and C.J. Summers, Appl. Phys. Lett. 72 (1998) 2226.

[69] S.P. Landau and K. Binder, A Guide to Monte Carlo Simulations in Statistical Physics (Cambridge University Press, UK 2000) p.37.

[70] A. Jablonksi, Phys. Rev. B. 47 (1993), 7420.

[71] Z. Czyzewski, D.O. MacCallum, A. Romig and D.C. Joy, J. Appl. Phys. 68 (1990) 3066.

[72] A. Jablonksi, Phys. Rev. B. 43 (1991), 7546.

[73] M. Fink and A.C. Yates, At. Data Nucl. Data Tables 1 (1970) 385.

[74] M. Fink and J. Ingram, At. Data Nucl. Data Tables 4 (1972) 129.

[75] D. Gregory and M. Fink, At. Data Nucl. Data Tables 14 (1974) 39.

[76] M.E. Riley, C.J. McCallum and F. Biggs, At. Data Nucl. Data Tables, 14 (1975) 443.

[77] M.J. Berger, S.M. Seltzer, R. Wang and A. Schecter, Elastic Scattering of Electrons and Positrons by Atoms: Database ELAST, NIST Internal Report NISTIR 5188 (National Institute of Standards and Technology,Gaithersburg,MD)

[78] L. Reimer and B. Lödding, Scanning 6 (1984) 128.

[79] MATLAB Application Program Interface Guide Version 5, The MathWorks Inc. (1998) p.4-2.

[80] R. Browning, T. Eimori, E.P. Traut, B. Chui and R.F.W. Pease, J. Vac. Sci. Technol. B 9 (1991) 3578.

[81] R. Browning, T.Z. Li, B. Chui, J. Ye, R.F.W. Pease, J. Appl. Phys 76 (1994) 2016.

[82] D.E. Newbury, D.C. Joy, P. Echlin, C.E. Fiori and J.I. Goldstein, Advanced Scanning Electron Microscopy and X-ray microanalysis (Plenum Press, New York, 1987) p.20.

Conference contributions

Here follows a list of contributions presented at local and international conferences based on the work done in this study.

International conferences

1. H.C. Swart and A.P. Greeff, *A Monte Carlo Simulation of the effect of a ZnO layer on the Cathodoluminescence of a FED phosphor*, Asian-Pacific Surface and Interface Analysis Conference (2000), Beijing, China
2. H.C. Swart, K.T. Hillie and A.P. Greeff, *The effect of temperature on the degradation of ZnS FED phosphors*, Asian-Pacific Surface and Interface Analysis Conference (2000), Beijing, China
3. A.P. Greeff and H.C. Swart, *A Monte Carlo simulation of cathodoluminescence generated in ZnS phosphor powders*, 14th International Conference on Defects in Insulating Materials (2000), Johannesburg, South Africa

Local conferences

1. A.P. Greeff and H.C. Swart, *Quantifying the cathodoluminescence generated in ZnS phosphor powders*, Annual conference of the South Africa Institute of Physics (2001), Natal University, Durban
2. A.P. Greeff and H.C. Swart, *A Monte Carlo simulation on the electron trajectories and energy loss in ZnS*, Annual conference of the South African Institute of Physics (2000), Rand Afrikaans University, Johannesburg
3. A.P. Greeff and H.C. Swart, *A Monte Carlo simulation of the effect of a ZnO layer on the Cathodoluminescence of a FED phosphor*, Annual conference of the South African Institute of Physics (2000), Rand Afrikaans University, Johannesburg
4. A.P. Greeff and H.C. Swart, *A Monte Carlo simulation on the electron beam incident angle with spherical particles applied to the energy loss in ZnS phosphor powders*, Annual conference of the South African Institute of Physics (2000), Rand Afrikaans University, Johannesburg

5. H.C. Swart, K.T. Hillie and A.P. Greeff, *The effect of temperature on the degradation of ZnS FED phosphors*, Annual conference of the South African Institute of Physics (2000), Rand Afrikaans University, Johannesburg

6. H.C. Swart, A.P. Greeff, P.H. Holloway and G.L.P. Berning, *The difference in degradation behavior of ZnS:Cu,Al,Au and ZnS:Ag,Cl phosphor powders*, Annual conference of the South African Institute of Physics (1998), University of Cape Town, Cape Town

Publication list

Here follows a complete list of publications to date by the author. Publications originating from this study are indicated by *.

1. * A.P. Greeff and H.C. Swart, *Quantifying the cathodoluminescence generated in ZnS phosphor powders using Monte Carlo energy loss simulations*, Surf. Int. Anal., Submitted July 2001.

2. * A.P. Greeff and H.C. Swart, *Modeling the effect of a thin ZnO layer on the cathodoluminescence generated in ZnS phosphor powders*, Thin Solid Films, Submitted June 2001.

3. * A.P. Greeff and H.C. Swart, *Monte Carlo simulation of low-energy electron trajectories and energy loss in ZnS phosphor powders*, Surf. Int Anal. 31 (2001) 448.

4. H.C. Swart, K.T. Hillie and A.P. Greeff, *Effect of temperature on the degradation of ZnS FED phosphors*, Surf. Int. Anal. 32 (2001) 110.

5. * H.C. Swart and A.P. Greeff, *Degradation effect of a ZnO layer on ZnS: comparison between a Monte Carlo simulation and experimental Auger and CL measurements*, Surf. Int. Anal. 32 (2001) 84.

6. * A.P. Greeff and H.C. Swart, *A Monte Carlo Simulation on the electron beam incident angle with spherical particles applied to the energy loss in ZnS phosphor powders*, Surf. Int. Anal. 29 (2000) 807.

7. * A.P. Greeff and H.C. Swart, *A Monte Carlo simulation of cathodoluminescence generated in ZnS phosphor powders*, Radiation Effects and Defects in Solids, Accepted June 2000

8. A.P. Greeff, C.W. Louw and H.C. Swart, *The high temperature oxidation of industrial FeCrMo steel*, Surf. Int. Anal. 30 (2000) 120.

9. A.P. Greeff, C.W. Louw and H.C. Swart, *The oxidation of industrial FeCrMo steel*, Corr. Sci. 42 (2000) 1725.

10. A.P. Greeff, H.C. Swart, C.W. Louw and J.J. Terblans, *The influence of sulphur segregation on the oxidation of industrial FeCrMo steel*, Corr. Sci. 42 (2000) 991.

11. A.P. Greeff, L.W. Wakaba, S. Cockroft, C.W. Louw and H.C. Swart, *The oxide layer formed on industrial FeCrMo steel during dry and wet high-temperature oxidation*, Proceedings of the 38th Conference of the Microscopy Society of Southern Africa (1999) 32

12. H.C. Swart, A.P. Greeff, P.H. Holloway and G.L.P. Berning, *The difference in degradation behavior of ZnS:Cu,Al,Au and ZnS:Ag,Cl phosphor powders*, Appl. Surf. Sci. 140 (1999) 63.

13. J.D. Saunderson, A.P. Greeff, H.C. Swart, C.M. Demanat, D.F. Langa, K.V. Sankar and R. Swanepoel, *Growth mechanisms of thin film amorphous silicon on metallised flexible substrates*, Proceedings of the 37th Conference of the Microscopy Society of Southern Africa (1998) 28.

U.O.V.S. BIBLIOTEEK